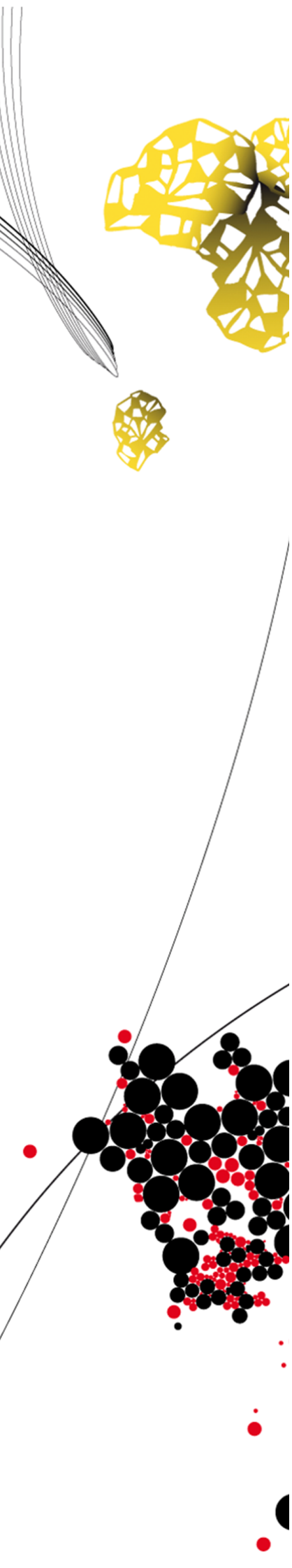

UNIVERSITY OF TWENTE.

Faculty of Engineering Technology

Low frequency calibration of an acoustic vector sensor using immersive wave propagation

P. V. L. Piening

M.Sc. Thesis
October 2022

Supervisors:
dr.ir. A.P. Berkhoff
Committee:
prof.dr.ing. B. Rosic
dr.ir. Y.H. Wijnant

Applied Mechanics and Data Analysis
Faculty of Engineering Technology
University of Twente
P.O. Box 217
7500 AE Enschede
The Netherlands

Abstract

This document investigates immersive boundary conditions used in immersive wave propagation, a method where one creates a virtual representation of a measured acoustic wave to remove, in real-time, undesired interactions with active boundaries. Desired interactions with virtual boundaries can be added, also in real-time. The ability to remove reflections caused by rigid boundaries using analytical physics-based extrapolation equations is investigated. In addition, the applicability of immersive wave propagation to low frequency vector-sensor calibration in enclosed spaces is investigated, where analytical physics-based immersive wave propagation is used for the removal of undesired reflections caused by the boundaries of the limited calibration environment. Derivations are given for one-, two- and three-dimensional problems. A one-dimensional numerical simulation shows that an analytical physics-based implementation exists that significantly reduces reflections during continuous operation. Physical experiments on a one-dimensional system require accurate filters to compensate transducer dynamics. A two-dimensional numerical simulation shows that there are differences between the analytical extrapolated velocity and the actual velocity. However, if velocity extrapolation is successful, relatively few monopole sources are required to significantly reduce the reflected waves at low frequencies. A three-dimensional simulation shows that for immersive boundary conditions in idealized circumstances the analytical physics base extrapolation equations are able to successfully extrapolate the particle velocity during continuous operation.

Contents

List of Symbols

Sign	Description	Unit
c	Sound speed	m/s
c_0	Small signal sound speed	m/s
$G^{p,q}$	Impulse pressure response to an impulse point source of volume injection	
$G^{v,f}_{i,m}$	Impulse velocity response in i direction to an impulse point source of force oriented in m direction	
$G^{v,q}_{i}$	Impulse velocity response in i direction to an impulse point source of volume injection	
$\mathbf{I}$	Time averaged acoustic intensity	W/m^2
$\mathbf{i}$	Instantaneous acoustic intensity	W/m^2
k	Wave number	m^{-1}
κ	Compressability of fluid	Pa^{-1}
P	Total pressure	Pa
p	Acoustic pressure	Pa
p_{rms}	Root mean square pressure	Pa
q	Volume source density of injection rate	s^{-1}
ρ	Mass density	kg/m^3
ρ_0	Ambient mass density	kg/m^3
$\delta\rho$	Excess mass density	kg/m^3
S^{emt}	Emitting surface for the Boundary conditions	
S^{rec}	Recording surface for the Boundary conditions	
t	Time	s
$\mathbf{v}$	Velocity vector	m/s
ϕ	Velocity potential	m^2/s
$V_{external}$	External domain	
V_{local}	Local or bounded domain	
V	Spatial domain	
$V_{virtual}$	Virtual domain	

Sign	Description	Unit
$\mathbf{x}$	Position vector	m

Acronyms

Abbreviation	Definition
FDTD	finite difference time domain
IBC	immersive boundary condition
PABC	perfectly absorbing boundary condition
PML	perfectly matched layers

Chapter 1

Introduction

An acoustic vector sensor is a device capable of measuring vector components of a sound field, such as sound particle velocity or acoustic intensity [1]. Sound intensity measurements allow for the measurement of sound generated by devices outside of carefully controlled test environments, as indicated in ISO 3740 [2] guidelines. Current standards regarding the use of intensity measurements, e.g. ISO 9614-1 [3], stipulate that the standard is only valid for a limited frequency range above 50 Hertz. This leaves frequencies below 50 Hertz out of scope for standardised measurements. The exclusion of frequencies outside this frequency range is attributed to limitations of intensity measurement equipment [3], i.e. acoustic vector sensors and their instrumentation.

For an acoustic vector-sensor to correctly measure aspects of a wave field, such as the acoustic intensity, it is important that such a sensor is properly calibrated. Small discrepancies can lead to significant errors, especially at low frequencies in vector sensors using a microphone array [4]. Calibration at low frequencies in enclosed spaces is challenging due to the presence of undesired sound reflection, or echo, that interferes with the calibration process. A sufficiently large calibration environment where the reflection travel time exceeds the duration of the calibration process may not be available. Alternatively one could perform the calibration inside an anechoic chamber [5]. The lower cutoff frequency of an anechoic chamber, the lower frequency limit above which the anechoic chamber shows anechoic behavior, may not be sufficient. Other passive methods, such as those published in [6], [7], tend to only work in a limited frequency range. A solution to the low frequency broadband reflection problem may be found in the application of active control systems.

Immersive wave propagation is an active control method that removes undesired reflections caused by reflective boundaries in real time using immersive boundary conditions (IBCs) and wavefield extrapolation functions. It also allows for the introduction of reflections caused by virtual objects inside a virtual environment in real time. It is the ability of immersive wave propagation to remove undesired reflections that is of interest in regards to creating an active anechoic environment for vector sensor calibration.

1.1 Literature review

The calibration can be performed using a number of methods. A relatively straightforward method is to perform a series of measurements with the vector sensor and compare the results to those obtained with a separate calibrated vector sensor [1]. Any inaccuracies of the already calibrated sensor will negatively affect the accuracy of the calibration of the other sensor [8].

Calibration can also be performed using free field reciprocity, however this has a lower limit of 800 Hertz [9]. Infrasound calibration can be performed in the $0.1 - 250$ Hertz range using specialised techniques and equipment [9], [10]. Pressure reciprocity calibration is a calibration method that is widely used in commercial devices [9], such as the type 4297 calibrator by B&K and the GRAS 51AC calibration kit, that performs well at low frequencies, however these devices are only compatible with specific types of vector sensors and not compatible with vector sensors with multiple sensing directions.

A alternative approach that is compatible with a wider range of vector sensors is to perform the calibration in an anechoic chamber as demonstrated by Kotus et. al. [5], which is described further in Chapter 2. This does require the anechoic chamber to be anechoic at the frequencies of interest, which is can be problematic when passive methods are used.

The development of active control methods to make a physical chamber anechoic are a relatively recent development in part due to the vast amount of computational power required, as illustrated by Becker et. al. [11]. One such method is immersive wave propagation by means of immersive boundary conditions. Immersive boundary conditions (IBCs) are exact boundary conditions that allow one to immerse a bounded domain, either physical or numerical, into a larger virtual domain. These boundary conditions were first proposed by van Manen et al. [12] and are based on the exact boundary conditions for unbounded scattering problems proposed by Ting and Miksis [13]. A physical implementation of these boundary conditions as a means to extend a physical experimental environment beyond its physical bounds was proposed by Vasmel et al. [14] as well as its name [15].

At the time of writing a number of articles have been published investigating and utilising these boundary conditions in both numerical and physical environments. Topics treated include: active reflection cancellation and immersion in a virtual domain for one-dimensional and two-dimensional physical waveguides [11], [16], broadband acoustic holography and cloaking [17], [18], modelling of sub domains [19] and the effects of boundary transducer directivity [20]. These publications show that the boundary conditions are versatile and can be implemented in real time. One may note that all these papers implement the immersive boundary conditions by using impulse responses obtained from either numerical simulations or experiments for the entire duration of the experiment. There is no research regarding a physics-based analytical implementation of immersive boundary conditions.

1.2 Motivation

This research aims to apply immersive boundary conditions to remove reflections in a confined calibration environment. The goal is to investigate whether the use of immersive wave propagation can be extended to the practical case of vector sensor calibration. To further current understanding of the physics and calculations involved in IBCs, as well as investigate options regarding implementation methods, it is of interest to develop physics based analytical extrapolation equations.

The application to low frequency vector calibration necessitates the evaluation of low frequency performance of the implementation of immersive boundary conditions in the sub kiloHertz frequency range. Currently physical experiments in air have been performed at the one to five kiloHertz range [11].

1.3 Framework

The research is carried out at the University of Twente for the Applied Mechanics and Data Analysis research group at the faculty of Engineering Technology as a Master thesis.

1.4 Research objectives

The objective of this research is to develop an physics-based implementation of immersive boundary conditions and asses whether it can adequately reduce reflections for use in low frequency vector sensor calibration applications. This thesis focuses on the development of a physics-based implementation with the aim to expand the knowledge base at the University of Twente and obtain a less computationally expensive implementation. In order to reduce computational costs further in two-dimensional setups, the performance dependency on transducer amount at low frequencies is investigated.

1.5 Report organization

The remainder of this report is organized as follows. Chapter 2 briefly treats vector sensors and their calibration. In Chapter 3 the assumptions and fundamental wavefield equations are presented, theory of immersive boundary conditions is presented and its general implementation is presented. The implementation and evaluation in one dimensional waveguides, two dimensional waveguides and three dimensional space are explored in Chapters 4 to 6 respectively. Finally Chapter 7 presents the overall conclusion and recommendations.

Chapter 2

Vector sensor calibration

2.1 Vector sensor

Before discussing how an acoustic vector sensor may be calibrated it is important to first establish what is meant by an acoustic vector sensor. An acoustic vector sensor in the most general sense is a passive device that measures a vector component of a sound field such as sound particle displacement, velocity or acceleration [1]. The term is also used to refer to a device that specifically measures the sound intensity $\mathbf{I}$ through the measurement of the acoustic pressure p and acoustic particle velocity $\mathbf{v}$ [1], [5]. Going forward the term acoustic vector-sensor refers to an acoustic intensity measurement device.

The sound intensity is defined as the time average of the instantaneous acoustic intensity, i.e.

$$\mathbf{I}(\mathbf{x},t) = \frac{1}{t_{avg}} \int_0^{t_{avg}} \mathbf{i}(\mathbf{x},t)\, dt, \tag{2.1}$$

where t_{avg} is the averaging time and $\mathbf{i}(\mathbf{x},t)$ is the instantaneous acoustic intensity. The instantaneous acoustic intensity is defined as the acoustic energy flow, or power, through an unit area and can be derived given the mechanical power $P = \mathbf{f} \cdot \mathbf{v}$ [21], [22], i.e.

$$\begin{aligned} \mathbf{i} \cdot \delta\mathbf{S} =& \mathbf{f} \cdot \mathbf{v}, \\ \mathbf{i}(\mathbf{x},t) =& p(\mathbf{x},t)\mathbf{v}(\mathbf{x},t) \end{aligned} \tag{2.2}$$

where $\delta\mathbf{S}$ is the increment of an area, $\mathbf{f}$ is the force exerted on a fluid particle, p is the acoustic pressure and $\mathbf{v}$ is the acoustic particle velocity.

Acoustic vector sensors can be categorized by the method they use to obtain the acoustic pressure $p(\mathbf{x},t)$ and particle velocity $\mathbf{v}(\mathbf{x},t)$ required to evaluate the intensity. The first category of acoustic vector sensor uses a p-$\mathbf{v}$ measurement principle, where two different types of transducers are used to directly measure both $p(\mathbf{x},t)$ and $\mathbf{v}(\mathbf{x},t)$ at the measurement location. The measurement of $p(\mathbf{x},t)$ can be done with a microphone. The measurement of $\mathbf{v}(\mathbf{x},t)$ can be done using a variety of methods. In air a Microflown sensors [4], [23], ribbon microphones or Doppler anemometry [1] can be used. In water one can utilize a neutrally

buoyant sphere containing a velocity sensitive sensor, apply laser interferometry combined with an acoustically compliant reflective membrane or apply the methods used in air [1].

The subject of this report is the more standard and established second category, which utilizes the p-p measurement principle. This measurement principle employs two pressure microphones, located at $\mathbf{x}_1$ and $\mathbf{x}_2$ respectively, to evaluate the intensity in the i direction at location $\mathbf{x}$, as shown in fig. 2.1. The pressure at position $\mathbf{x}$ can be estimated by linear interpolation of the recorded pressures [22], i.e.

$$p(\mathbf{x}, t) \approx \frac{p(\mathbf{x}_1, t) + p(\mathbf{x}_2, t)}{2}, \tag{2.3}$$

or it can be obtained directly by introducing a third microphone at $\mathbf{x}$. In order to obtain the velocity at $\mathbf{x}$, the equation of motion for an acoustic fluid particle is required. The derivation of this equation is presented in Chapter 3 and results in

$$\rho_0(\mathbf{x}) \frac{\partial \mathbf{v}(\mathbf{x}, t)}{\partial t} + \nabla p(\mathbf{x}, t) = 0.$$

By rearranging the equation of motion and applying a finite difference approximation of the spatial derivative in the i-direction one may obtain the velocity at $\mathbf{x}$ in the i-direction [4], [24], [25] using

$$v_i(\mathbf{x}^{rec}, t) \approx -\frac{1}{\rho d} \int_0^t \left[p(\mathbf{x}_2^{rec}, t) - p(\mathbf{x}_1^{rec}, t) \right] dt. \tag{2.4}$$

Here the separation distance d, the distance between $\mathbf{x}_1^{rec}$ and $\mathbf{x}_2^{rec}$ in the i-direction, should be small compared to the signal wavelength for these equations to hold. This places an upper limit on the frequency at which the intensity can be accurately evaluated. The upper frequency limit used by Kotus et al. [5] for their vector sensor can be approximated by

$$f_{max} = \frac{\frac{1}{4}c}{d}, \tag{2.5}$$

Fahy [22] notes that for intensity measurements of plane waves one must ensure that $f\ d < 30$ in order to obtain a relative error of less than 5%.

Using the p-p measurement method does require careful calibration as a phase difference between the two microphones results in a bias error in the intensity $\mathbf{I}$ [4]:

$$I_{estimate} = I_{true}(1 - \frac{\varphi_{error}}{kd} \frac{{p_{rms}}^2}{I_{true}}), \tag{2.6}$$

where $\mathbf{I}_{true}$ is the actual intensity, φ_{error} is the phase error and p_{rms} is the root mean square pressure. Equation (2.6) shows that the error is inversely proportional to the wave number, and therefore inversely proportional to the frequency. This illustrates the importance of low frequency calibration when evaluating the sound intensity $\mathbf{I}$ at low frequencies.

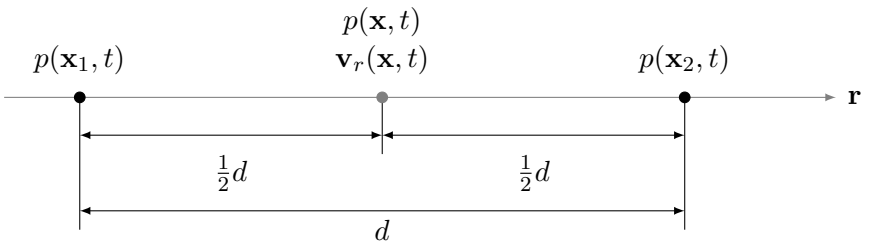

Figure 2.1: Schematic of an acoustic vector sensor using the p-p measurement principle to measure the acoustic intensity $\mathbf{i}(x_1, t)$ in the i direction.

2.2 Calibration

As mentiond in Chapter 1, calibration can be performed using variaty of methods. Here the method used by Kotus et. al. [5], i.e. calibration in an anechoic chamber, is presented as it may benefit from the applition of active reflection removal. The method used by Kotus et. al. is described here for completeness.

First the pressure microphones should be checked for proper operation by means of standard single microphone calibration procedures. Once this has been done, a two step calibration procedure can be performed. The first calibration step of the vector sensor is performed using the configuration shown in fig. 2.2. The microphones are placed perpendicular to the propagation direction of the plane wave generated at the source. The goal of this step is to obtain discrete time calibration filters $q_{x_1}(n)$ and $q_{x_2}(n)$ that ensure the amplitude of both recorded signals is identical, i.e.

$$h_{x_1}(n)q_{x_1}(n) = h_{x_2}(n)q_{x_2}(n), \tag{2.7}$$

where $h(n)$ is the impulse response of a microphone. The impulse responses can be obtained by generating a linear swept sine signal and applying the cross-correlation technique [26]. The impulse responses can be converted to their spectral forms $H_{x_1}(f)$ and $H_{x_2}(f)$ and the difference $E_x(f)$ can be calculated using

$$E_x(f) = \mathsf{log}_{10}|H_{x_2}(f)| - \mathsf{log}_{10}|H_{x_1}(f)| \tag{2.8}$$

In the absence of a reference microphone, the error has to be distributed over both microphones [5]. The correction functions in the frequency domain can then be calculated using

$$Q_{x_1}(f) = 10^{E_x(f)/2} \qquad Q_{x_2}(f) = 10^{E_x(f)/2} \tag{2.9}$$

The final correction functions $q_{x_1}(n)$ and $q_{x_2}(n)$ are obtained by transforming these spectral filters to the time domain.

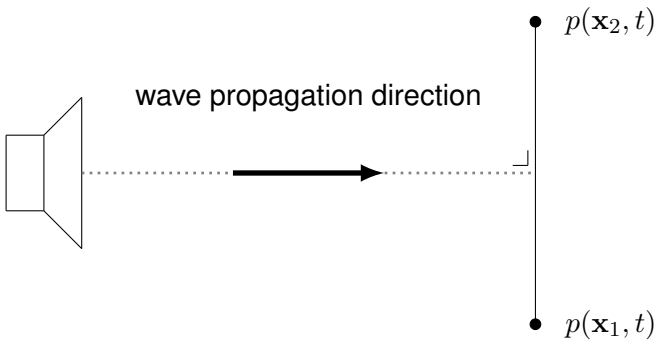

Figure 2.2: Schematic of the first step for calibrating an acoustic vector sensor using the p-p measurement principle.

In the second calibration step calibration filters are obtained that aim to remove any phase difference between the estimated velocity and estimated pressure such that the following condition holds:

$$\frac{p(t)}{v_1(\mathbf{x}, t)} = \frac{\frac{1}{2}\left(p_{x1}(t) + p_{x2}(t)\right)}{p_{x1}(t) - p_{x2}(t)} = C, \tag{2.10}$$

where C is a constant. For calibration purposes C can be set to $C = 0.5$.

In order to perform this calibrations step, the vector sensor must be oriented in the direction in which it would be used to obtain the sound intensity as shown in fig. 2.3. In order to obtain the phase calibration filter Q_{ux}, the impulse responses $h_p(t)$ and $h_{ux}(t)$ are obtained from the earlier obtained amplitude corrected impulse responses

$$h_p(t) = 0.5\left(h_{x2}(t) + h_{x1}(t)\right), \tag{2.11}$$

$$h_{ux}(t) = \left(h_{x2}(t) - h_{x1}(t)\right). \tag{2.12}$$

Signals $h_p(t)$ and $h_{ux}(t)$ are aligned such that for both impulse responses $h(0) = \max(h(n))$. The phase correction is applied to $h_{ux}(t)$ such that

$$\arg\left(H_{ux}(f) Q_{ux}(f)\right) = \arg\left(H_p(f)\right), \tag{2.13}$$

where $|Q_{ux}(f)| = 1$, $\arg\left(Q_{ux}(f)\right) = \arg\left(H_p(f) - H_{ux}(f)\right)$ and $\arg\left(H(f)\right)$ is the unwrapped phase of $H(f)$. The phase correction function $q_{ux}(n)$ is obtained by transforming $Q_{ux}(f)$ to the time domain.

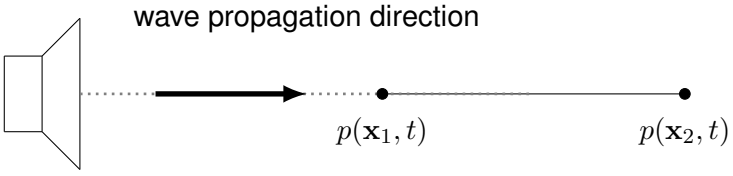

Figure 2.3: Schematic of the second step for calibrating an acoustic vector sensor using the p-p measurement principle.

With the calibration filters applied, the instantaneous intensity can be obtained by implementing the schematic shown in fig. 2.4. The calibration process can be repeated for two additional orthogonal microphone pairs in order to calibrate a three dimensional acoustic vector sensor. When these sensors are placed on the center of the faces of a cube, one may obtain the pressure $p(\mathbf{x}, t)$ at the center of the cube by averaging all six microphones [5], which is equivalent to averaging the pressure at $p(\mathbf{x}, t)$ obtained from each pair of pressure microphones.

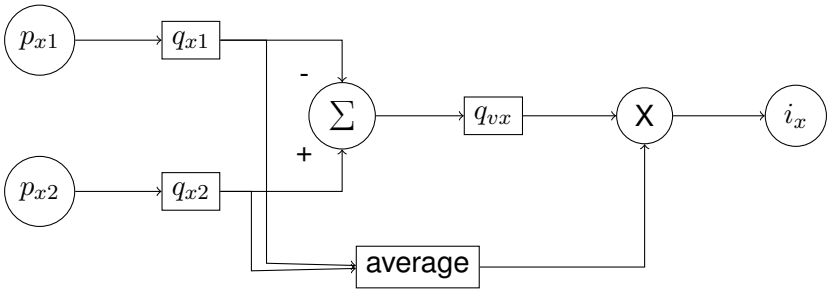

Figure 2.4: Schematic of the acoustic intensity calculation with filters applied.

This calibration procedure assumes the following. Firstly it assumes that the relation $\frac{p(t)}{v_x(t)} = constant$ actually yields a constant. When the sound source generates a spherical wave, such as when an omnidirectionally radiating sound source is used inside an anechoic chamber, the impedance experienced by the generated wave follows the frequency domain relation

$$Z_0(s) = \rho_0 c_0 \frac{rs}{rs + c_0}. \tag{2.14}$$

The derivation of this equation is presented in appendix A.3, and shows that this impedance does not equal a constant value for spherical waves. One may consider performing the calibration in a one dimensional waveguide. This would ensure the presence of plane waves, which do follow the $\frac{p(t)}{v_x(t)} = constant$ relation.

The second assumption is that no reflections are recorded. This is done by performing the measurements inside an anechoic chamber [5], however this assumption may be erroneous for frequencies below the lower cutoff frequency of the anechoic chamber. A one dimensional waveguide of finite length generates reflections due to the termination of the tube, either a rigid boundary in case of a closed waveguide or a pressure release boundary at low frequencies in case of an open tube [21]. In case of a closed tube this may be mitigated by applying passive acoustic dampening similar to an anechoic chamber. Alternatively these reflections may be cancelled by means of active control using immersive boundary conditions.

Chapter 3

Immersive Boundary Conditions

As stated in Chapter 1 the immersive boundary conditions (IBCs) are exact boundary conditions that can be applied to a finite truncated domain in order to immerse said domain into a different virtual domain. In this chapter first the general assumptions are stated and the linearized wavefield equations are derived. Next the immersive boundary conditions are derived in a general sense. Finally the required wavefield extrapolation is treated together with a discretized implementation. Specifics regarding the one dimensional, two dimensional and three dimensional implementation are treated in Chapters 4 to 6 respectively.

3.1 Wavefield equations

Before starting with the derivation of the wavefield equations and boundary conditions the following assumptions are made:

1. The control volume that is used for the equations is fixed in space, i.e. an Eulerian coordinate system is used.

2. The fluid is assumed to be inviscid, or nonviscous.

3. Body forces such as gravity are neglected.

4. The flow of fluid is assumed to be lossless.

With these assumptions in place, the starting point for this derivation are the continuity equation, based on the conservation of mass on a finite volume element, and the momentum equation, based on conservation of momentum on a finite volume element. This derivation follows the approach of [21] and is included for completeness. For an inhomogeneous acoustic medium the continuity equation and momentum equation are respectively [21]:

$$\frac{D\rho(\mathbf{x},t)}{Dt} + \rho(\mathbf{x},t)\nabla\cdot\mathbf{v}(\mathbf{x},t) = 0, \tag{3.1}$$

$$\rho(\mathbf{x},t)\frac{D\mathbf{v}(\mathbf{x},t)}{Dt} + \nabla P(\mathbf{x},t) = 0. \tag{3.2}$$

Here the D/Dt operator is the material derivative, which corresponds to:

$$\frac{Dq}{Dt} = \frac{\partial q}{\partial t} + \mathbf{v} \cdot \nabla q. \tag{3.3}$$

In addition to these equations, an equation of state relating thermodynamic properties is also required. As the losses are assumed to be negligible the isentropic equation of state for an arbitrary fluid can be used [21], which for inhomogenious fluids can be written as

$$p(\mathbf{x}, t) = {c_0}^2(\mathbf{x}) \delta\rho(\mathbf{x}, t) \left[1 + \frac{B}{2!A} \frac{\delta\rho(\mathbf{x}, t)}{\rho_0(\mathbf{x})} + \frac{C}{3!A} \left(\frac{\delta\rho(\mathbf{x}, t)}{\rho_0(\mathbf{x})} \right)^2 + \dots \right]. \tag{3.4}$$

Here A, B and C are coefficients that can be determined from experiments. For most acoustic signals the pressure variations are small compared to the static pressure of the medium. As this is also the case here eqs. (3.1), (3.2) and (3.4), can be simplified using the small signal approximation [21], i.e.:

$$|\delta\rho| \ll |\rho_0| \qquad |p| \ll |\rho_0 {c_0}^2| \qquad |\mathbf{v}| \ll |c_0|. \tag{3.5}$$

Applying the small signal approximation of eq. (3.5) to eqs. (3.1) and (3.2) reduces the material derivative to a partial derivative with respect to time, i.e.:

$$\frac{\partial \delta\rho(\mathbf{x}, t)}{\partial t} + \rho_0(\mathbf{x}) \nabla \cdot \mathbf{v}(\mathbf{x}, t) = 0, \tag{3.6}$$

$$\rho_0(\mathbf{x}) \frac{\partial \mathbf{v}(\mathbf{x}, t)}{\partial t} + \nabla p(\mathbf{x}, t) = 0, \tag{3.7}$$

where eq. (3.7) is the local equation of motion. Applying eq. (3.5) to eq. (3.4) yields

$$p = {c_0}^2 \delta\rho. \tag{3.8}$$

Replacing the excess density $\delta\rho$ in eq. (3.6) using eq. (3.8) and rearranging terms yields the deformation equation

$$\frac{1}{\rho_0(\mathbf{x}) {c_0}^2(\mathbf{x})} \frac{\partial p}{\partial t} + \nabla \cdot \mathbf{v}(\mathbf{x}, t) = 0, \tag{3.9}$$

where $\frac{1}{\rho_0(\mathbf{x}) {c_0}^2(\mathbf{x})}$ can be replaced by the compressibility of the fluid

$$\kappa_0(\mathbf{x}) = \frac{1}{\rho_0(\mathbf{x}) {c_0}^2(\mathbf{x})}. \tag{3.10}$$

The standard second order linearized acoustic equation is obtained by applying the partial derivative with respect to time to eq. (3.9) and substituting in eq. (3.7):

$$\frac{\partial^2 p(\mathbf{x}, t)}{\partial t^2} - {c_0}^2(\mathbf{x}) \nabla^2 p(\mathbf{x}, t) = 0. \tag{3.11}$$

Adding sources to eqs. (3.7) and (3.9) results in the acoustic wave equations that form the starting point in the works of Vasmel [15] and Broggini et al. [19]:

$$\kappa_0(\mathbf{x}) \frac{\partial p(\mathbf{x}, t)}{\partial t} + \nabla \cdot \mathbf{v}(\mathbf{x}, t) = q(\mathbf{x}, t), \tag{3.12}$$

$$\rho_0(\mathbf{x}) \frac{\partial \mathbf{v}(\mathbf{x}, t)}{\partial t} + \nabla p(\mathbf{x}, t) = \mathbf{f}(\mathbf{x}, t). \tag{3.13}$$

Alternatively one can obtain eqs. (3.12) and (3.13) by starting with the equation of motion and the deformation equation, including source terms, and applying the constitutive relations and using a low-velocity approximation of the result, as outlined by Fokkema and van den Berg [27]. The low-velocity approximation used is analogous to the small-signal approximation used here and both methods yield equations that allow for inhomogeneous fluids.

3.2 Boundary conditions

Now that the equations governing the pressure and particle velocity wavefields have been established the actual boundary conditions can be derived. This largely follows the approach of Vasmel [15] and Broggini et al. [19] and is included for completeness and clarity. Suppose there is a configuration as shown in figure 3.1, where V_{local} is the domain enclosed by S^{emt} and $V_{external}$ is the complement of V_{local}.

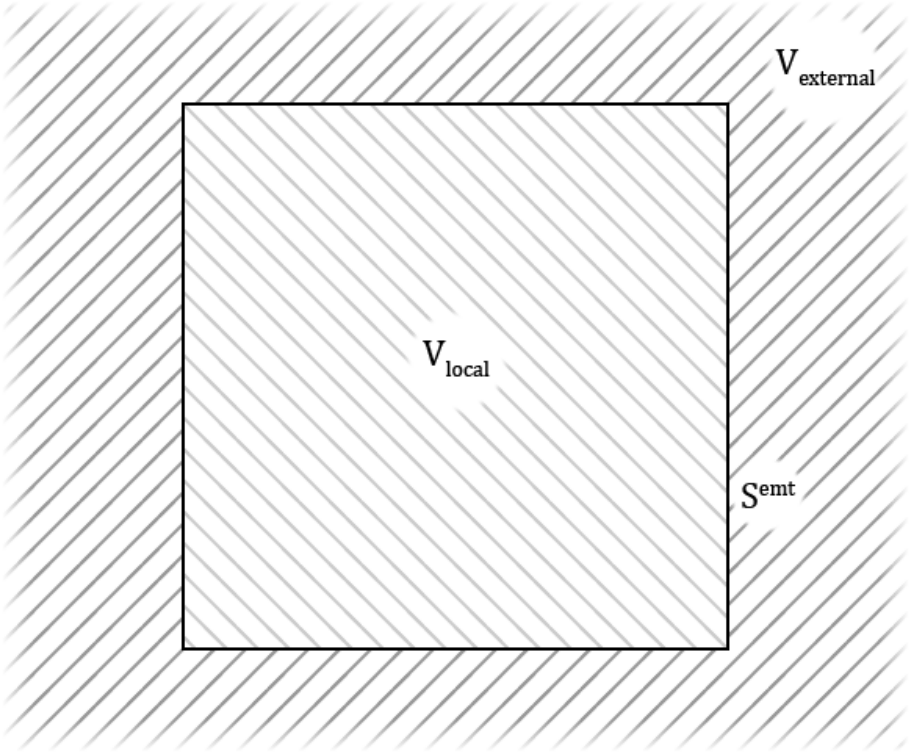

Figure 3.1: Domains for derivation of immersive boundary conditions.

The wavefield inside a domain V can be described using Rayleigh's reciprocity theorem of the convolution type [28]. When this version of Rayleigh's reciprocity theorem is applied to

the domain V_{local} shown in fig. 3.1, it relates two acoustic states as follows [15], [27]:

$$\oint_{S^{emt}} \{p_A(\mathbf{x},t) * v_{i,B}(\mathbf{x},t) - v_{i,A}(\mathbf{x},t) * p_B(\mathbf{x},t)\}\, n_i dS = \\ \frac{\partial}{\partial t}\int_{V_{local}} \{[\kappa_A(\mathbf{x}) - \kappa_B(\mathbf{x})][p_A(\mathbf{x},t) * p_B(\mathbf{x},t)] - [\rho_A(\mathbf{x}) - \rho_B(\mathbf{x})][v_{i,A}(\mathbf{x},t) * v_{i,B}(\mathbf{x},t)]\}\, dV \\ + \int_{V_{local}} \{p_A(\mathbf{x},t) * q_B(\mathbf{x},t) - v_{i,A}(\mathbf{x},t) * f_{i,B}(\mathbf{x},t) - q_A(\mathbf{x},t) * p_B(\mathbf{x},t) + f_{i,A} * v_{i,B}(\mathbf{x},t)\}\, dV. \tag{3.14}$$

Here the $*$ denotes temporal convolution and the subscripts A and B denote which acoustic state the wavefield and medium parameters belong to.

At this point one can define three states: $\overline{A}$, A and B. State $\overline{A}$ is an acoustic state where a source distribution described by $\{q, 0\}(\mathbf{x},t)$ generates a wavefield described by $\{\overline{p}, \overline{v}_i\}(\mathbf{x})$. The medium parameters are described by $\{\rho, \kappa\}(\mathbf{x},t)$. No boundary conditions are applied meaning that the waves freely radiate through the boundary S^{emt} and no reflections occur due to S^{emt}. This would be the desired state.

State A is the same as state $\overline{A}$ however, and without loss of generality, Neumann boundary conditions are assumed on the boundary S^{emt}, i.e. the velocity normal to S^{emt} is zero or $v_i|_{S^{emt}} n_i = 0$. This corresponds to the situation where there is a rigid reflecting boundary at S^{emt} such as a perfectly rigid wall, floor or ceiling.

Finally state B is an auxiliary state. This auxiliary state can be chosen such that when it is applied to eq. (3.14) together with either state $\overline{A}$ or state A, one obtains a relation for the pressure $\overline{p}(\mathbf{x},t)$ or $p(\mathbf{x},t)$ respectively. This is the case if the source distribution is chosen to be a point source of volume injection rate described by $q^B(t)\delta(\mathbf{x} - \mathbf{x}^R)$, where δ is the spatial Dirac distribution. The wavefield is described by the pressure and velocity radiating from that point source, i.e. $\{p^q, \mathbf{v}_i^q\}(\mathbf{x}, \mathbf{x}^R, t)$ and the medium parameters are the same as those of states $\overline{A}$ and A.

When state B is converted to the frequency domain one can apply the following linear relation to relate p^q and $\mathbf{v}_i^q$ to $q^B(s)$:

$$\hat{p}^q(\mathbf{x}, \mathbf{x}^R, s) = \hat{G}^{p,q}(\mathbf{x}, \mathbf{x}^R, s) q^B(s), \tag{3.15}$$

$$\hat{\mathbf{v}}_i^q(\mathbf{x}, \mathbf{x}^R, s) = \hat{G}_i^{v,q}(\mathbf{x}, \mathbf{x}^R, s) q^B(s). \tag{3.16}$$

$\hat{G}^{p,q}$ and $\hat{G}_i^{v,q}$ are the frequency domain pressure and velocity response respectively due to an impulse point source of volume injection rate at the source location $\mathbf{x}^R$. By replacing the wavefield with eqs. (3.15) and (3.16) one can omit $q(s)$ from the source description as this is already included in the Green's states. The wavefield of state B becomes by $\{\hat{G}^{p,q}, \hat{G}_i^{v,q}\}(\mathbf{x}, \mathbf{x}^R, s)$ and the source distribution becomes $\delta(\mathbf{x} - \mathbf{x}^R)$. The boundary condition of state A is also applied, although for state B this would be expressed as $\hat{G}_i^{v,q}|_{S^{emt}} n_i = 0$.

Converting everything back to the time domain yields the state time domain state B shown in table 3.1, shown together with states $\overline{A}$ and A.

State	$\overline{A}$	A	B
Wavefield	$\{\overline{p}, \overline{v_i}\}(\mathbf{x}, t)$	$\{p, v_i\}(\mathbf{x}, t)$	$\{G^{p,q}, G_i^{v,q}\}(\mathbf{x}, \mathbf{x}^R, t)$
Medium parameters	$\{\rho, \kappa\}(\mathbf{x})$	$\{\rho, \kappa\}(\mathbf{x})$	$\{\rho, \kappa\}(\mathbf{x})$
Source functions	$\{q, 0\}(\mathbf{x}, t)$	$\{q, 0\}(\mathbf{x}, t)$	$\{\delta(\mathbf{x} - \mathbf{x}^R), 0\}$
BC's on S^{emt}	none	$v_i\|_{S^{emt}} n_i = 0$	$G_i^{v,q}\|_{S^{emt}} n_i = 0$

Table 3.1: Parameters of states $\overline{A}$, A and B. State $\overline{A}$ corresponds to a wavefield propagating unhindered through S^{emt} and states A and B correspond to states in which the wavefield only propagates in the truncated domain with Neumann boundary conditions on S^{emt}.

Now that the three states have been introduced, eq. (3.14) can be used. Substituting the parameters of states $\overline{A}$ and B into eq. (3.14) yields

$$\begin{aligned}&\oint_{S^{emt}} \left\{\overline{p}(\mathbf{x}, t) * G_i^{v,q}(\mathbf{x}, \mathbf{x}^R, t) - \overline{v}_i(\mathbf{x}, t) * G^{p,q}(\mathbf{x}, \mathbf{x}^R, t)\right\} n_i dS \\ &= \frac{\partial}{\partial t} \int_V \{0\} dV + \int_V \left\{\overline{p}(\mathbf{x}, t) * \delta(\mathbf{x} - \mathbf{x}^R) - 0 + q(\mathbf{x}, t) * G^{p,q}(\mathbf{x}, \mathbf{x}^R, t) - 0\right\} dV. \end{aligned} \tag{3.17}$$

Splitting the integrals and applying the BC's of state B reduces eq. (3.17) to

$$\begin{aligned}&- \oint_{S^{emt}} \left\{\overline{v}_i(\mathbf{x}, t) * G^{p,q}(\mathbf{x}, \mathbf{x}^R, t)\right\} n_i dS \\ &= \int_V \left\{\overline{p}(\mathbf{x}, t) * \delta(\mathbf{x} - \mathbf{x}^R)\right\} dV + \int_V \left\{q(\mathbf{x}, t) * G^{p,q}(\mathbf{x}, \mathbf{x}^R, t)\right\} dV. \end{aligned} \tag{3.18}$$

By rearranging terms, resolving the first volume integral and applying source-receiver reciprocity, i.e.

$$G^{p,q}(\mathbf{x}, \mathbf{x}^R, t) = G^{p,q}(\mathbf{x}^R, \mathbf{x}, t), \tag{3.19}$$

one can rewrite eq. (3.18) to obtain the following equation for the desired pressure field:

$$\overline{p}(\mathbf{x}^R, t) = \int_V G^{p,q}(\mathbf{x}^R, \mathbf{x}, t) * q(\mathbf{x}, t) dV - \oint_{S^{emt}} G^{p,q}(\mathbf{x}^R, \mathbf{x}, t) * \overline{v}_i(\mathbf{x}, t) n_i dS \quad \text{for } \mathbf{x}^R \in V. \tag{3.20}$$

This process can be repeated by substituting state A instead of state $\overline{A}$ into eq. (3.14). Doing so yields the following equation:

$$p(\mathbf{x}^R, t) = \int_V G^{p,q}(\mathbf{x}^R, \mathbf{x}, t) * q(\mathbf{x}, t) dV \quad \text{for } \mathbf{x}^R \in V. \tag{3.21}$$

Substituting eq. (3.21) into eq. (3.20) gives an expression for the desired wavefield pressure in terms of the actual wavefield pressure and an additional term:

$$\overline{p}(\mathbf{x}^R, t) = p(\mathbf{x}^R, t) - \oint_{S^{emt}} G^{p,q}(\mathbf{x}^R, \mathbf{x}, t) * \overline{v}_i(\mathbf{x}, t) n_i dS \quad \text{for } \mathbf{x}^R \in V. \tag{3.22}$$

This additional term would be the pressure field that needs to be introduced to obtain the desired pressure field and should be the pressure field generated by the immersive boundary conditions, i.e.:

$$p^{IBC}(\mathbf{x}^R, t) = -\oint\limits_{S^{emt}} G^{p,q}(\mathbf{x}^R, \mathbf{x}, t) * \overline{v}_i(\mathbf{x}, t) n_i dS \quad \text{for } \mathbf{x}^R \in V. \tag{3.23}$$

Note that this pressure field is the pressure impulse response inside domain V due to impulse points sources of volume injection rate on the boundary S^{emt} that are scaled with the desired velocity $\overline{v}_i(\mathbf{x}, t)$ at S^{emt}.

3.3 Wavefield extrapolation

In order to implement these boundary conditions one must obtain the desired velocity $\overline{v}_i$ on S^{emt}. This can be done by recording the incoming wavefield at the recording surface S^{rec}, shown in fig. 3.2, and extrapolating it to S^{emt}.

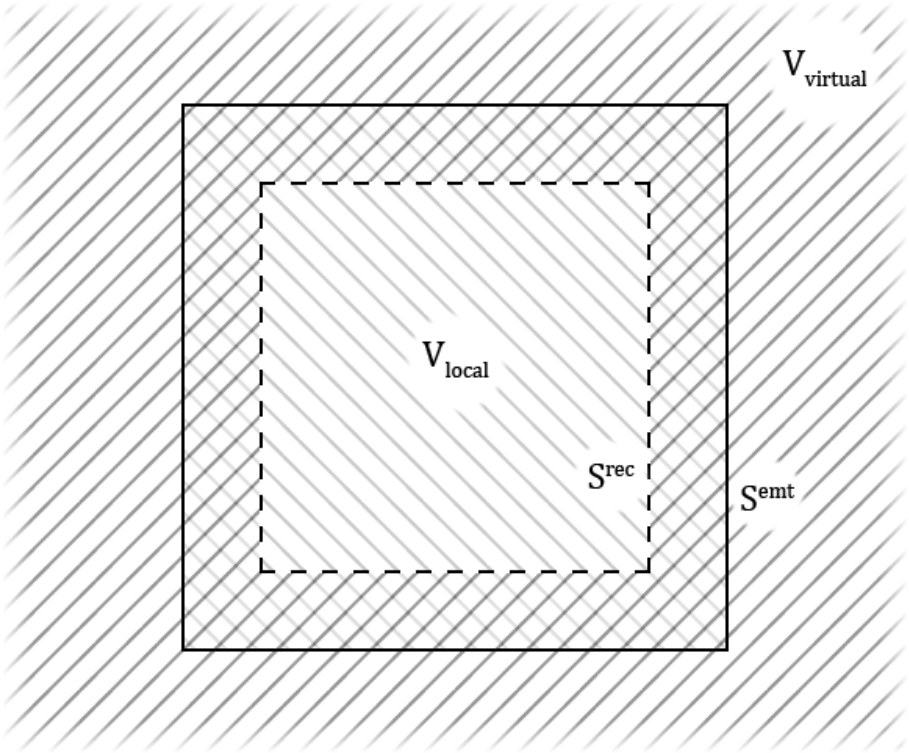

Figure 3.2: Domains for the velocity extrapolation.

This extrapolation can be done using eq. (3.24) [15],

$$\begin{aligned}\overline{v}_i(\mathbf{x}^{emt}, \tau) = \int_0^\tau \oint\limits_{S^{rec}} \Big\{ & G_i^{v,q}(\mathbf{x}^{emt}, \mathbf{x}, \tau - t) \overline{v}_m(\mathbf{x}, t) \\ & + G_{i,m}^{v,f}(\mathbf{x}^{emt}, \mathbf{x}, \tau - t) \overline{p}(\mathbf{x}, t) \Big\} n_m dS dt,\end{aligned} \tag{3.24}$$

where n_m is the outward normal of S^{rec} and $\mathbf{x}^{emt}$ is a point on S^{emt}. The extrapolation Green's functions required here need to be of the virtual domain and can include the effects of scatterers present in $V_{virtual}$ [15] [19]. In other words these Green's functions allow one to immerse domain V_{local} in domain $V_{virtual}$, where domain $V_{virtual}$ can contain any number of scattering objects. This is what makes these boundary conditions immersive.

One may note that $V_{virtual}$ overlaps V_{local} between S^{rec} and S^{emt}. This means that any scatterers inside the physical domain V_{local} in this region must also be included in the extrapolation Green's functions, i.e. in the virtual domain $V_{virtual}$.
For the actual implementation in discrete time simulations and digitally controlled hardware eq. (3.24) can be discretized in time according to [11] as

$$\begin{aligned}\hat{\overline{v}}_i(\mathbf{x}^{emt}, l, k) = \sum_{l=k}^{N_T-1} \oint_{S^{rec}} \Big\{ &\hat{G}^{v,q}(\mathbf{x}^{emt}, \mathbf{x}, l-k)\hat{\overline{v}}_m(\mathbf{x}, k) \\ &+ \hat{G}^{v,f}(\mathbf{x}^{emt}, \mathbf{x}, l-k)\hat{\overline{p}}(\mathbf{x}, k)\Big\} n_m dS. \end{aligned} \tag{3.25}$$

Here the $\hat{}$ denotes discrete parameters and τ and t have been replaced by l and k respectively. The parameter N_T corresponds to the total number of time steps of a simulation or experiment of finite duration. By selecting the upper limit of the sum in this manner one ensures that any wave, reflection and attenuation behavior included in the extrapolation Green's functions that should arrive at S^{emt} during this time period do so. This does limit the use of this implementation to cases where it only needs to operate for a limited duration and requires extrapolation for the entire duration.

Alternatively one can modify eq. (3.25) to reduce the number of computations and allow for continuous operation by adjusting the upper limit of the summation, i.e.

$$\begin{aligned}\hat{\overline{v}}_i(\mathbf{x}^{emt}, l, k) = \sum_{l=k}^{N_t+k} \oint_{S^{rec}} \Big\{ &\hat{G}^{v,q}(\mathbf{x}^{emt}, \mathbf{x}, l-k)\hat{\overline{v}}_m(\mathbf{x}, k) \\ &+ \hat{G}^{v,f}(\mathbf{x}^{emt}, \mathbf{x}, l-k)\hat{\overline{p}}(\mathbf{x}, k)\Big\} n_m dS. \end{aligned} \tag{3.26}$$

Here N_t is a fixed number of discrete time steps that are used for extrapolation. For any finite value of N_t one limits the wave, reflection and attenuation behaviour to that with a travel time less than $N_t \cdot dt$. In order to include the relevant behavior of waves and reflections, one should ensure that the number of time steps exceeds the travel time of the behavior of these waves and reflections. This does mean that in specific cases, such as those described in Chapters 4 and 6, one can significantly limit the number of extrapolation steps required, reducing computation time.

Both eqs. (3.25) and (3.26) can be written recursively [11] using

$$\begin{aligned}\hat{\bar{v}}_i(\mathbf{x}^{emt}, l, k) =& \hat{\bar{v}}_i(\mathbf{x}^{emt}, l, k-1) \\ &+ \oint_{S^{rec}} \Big\{ G_i^{\hat{v},q}(\mathbf{x}^{emt}, \mathbf{x}, l-k) \hat{\bar{v}}_m(\mathbf{x}, k) \\ &\quad + G_{i,m}^{\hat{v},f}(\mathbf{x}^{emt}, \mathbf{x}, l-k) \hat{\bar{p}}(\mathbf{x}, k) \Big\} n_m dS \end{aligned} \tag{3.27}$$

with different value ranges for l for easier implementation. Equation (3.27) extrapolates the values recorded on S^{rec} at time step k to obtain the values for $\hat{\bar{v}}_i(\mathbf{x}^{emt}, l \geqslant k, k)$. When using this scheme one would apply the value of $\hat{\bar{v}}_i(\mathbf{x}^{emt}, l = k, k)$ to the boundary and the values $\hat{\bar{v}}_i(\mathbf{x}^{emt}, l > k, k)$ are stored for subsequent time steps.

The numerical implementation of eq. (3.27) can be schematically represented in the following figures. Figure 3.3 shows the numerical implementation of the surface integral calculation for N_t time steps. These Green's states are scaled with the surface area segment ΔS, which is obtained by dividing the total recording surface area by the number of recording points. While not neccesary for the finite duration implementation, it is advantageous to extrapolate a constant number of time steps, as this will ensure a constant calculation time. Figure 3.4 shows the iterative component of eq. (3.27) when the finite duration implementation is applied. The integral is reshaped such that each output is assigned to a row and any extrapolated time steps that would exceed N_t are discarded. The first column highlighted in green is the value that will be applied to the sources on S^{emt}, although one can also select the values in one of the columns in the blue highlighted area. Doing so advances the output in time, which can be used to compensate various delays that are introduced by calculations, discrete filters and other phenomena.

$$\begin{pmatrix} \overset{\Delta S\, G_i^{\hat{v},q}}{\begin{matrix} 1,1 & \dots & 1,N_{AI} \\ \vdots & \ddots & \vdots \\ N_t,1 & \dots & N_t,N_{AI} \\ N_t+1,1 & \dots & N_t+1,N_{AI} \\ \vdots & \ddots & \vdots \\ \vdots & \ddots & \vdots \\ N_{AO}N_t,1 & \dots & N_{AO}N_t,N_{AI} \end{matrix}} & \Bigg| & \overset{\Delta S\, G_{i,m}^{\hat{v},f}}{\begin{matrix} 1,1 & \dots & 1,2N_{AI} \\ \vdots & \ddots & \vdots \\ N_t,1 & \dots & N_t,2N_{AI} \\ N_t+1,1 & \dots & N_t+1,2N_{AI} \\ \vdots & \ddots & \vdots \\ \vdots & \ddots & \vdots \\ N_{AO}N_t,1 & \dots & N_{AO}N_t,2N_{AI} \end{matrix}} \end{pmatrix} \begin{pmatrix} \overset{\frac{\hat{\bar{v}}_m(\mathbf{x},k)}{\hat{\bar{p}}(\mathbf{x},k)}}{\begin{matrix} 1 \\ \vdots \\ N_{AI} \\ N_{AI}+1 \\ \vdots \\ \vdots \\ 2N_{AI} \end{matrix}} \end{pmatrix} = \begin{pmatrix} \overset{\oint_{S^{rec}}}{\begin{matrix} 1 \\ \vdots \\ N_t \\ N_t+1 \\ \vdots \\ \vdots \\ 2N_{AI} \end{matrix}} \end{pmatrix}$$

Figure 3.3: Schematic of integral calculation of Equation (3.27). Here N_{AI} is the number of points on S^{rec} where the position and velocity are recorded. N_{AO} is the number of IBC sources on S^{emt} and N_t is the number of timesteps used for the extrapolation.

$$\underset{\oint_{Srec}}{\begin{pmatrix} 1,1 & \dots & 1,N_t-k+1 \\ \vdots & \ddots & \vdots \\ N_{AO},1 & \dots & N_{AO},N_t-k+1 \end{pmatrix}} + \underset{\hat{\bar{v}}_m(\mathbf{x},k-1;l)}{\begin{pmatrix} 1,l=k & \dots & 1,l=N_t \\ \vdots & \ddots & \vdots \\ N_{AO},l=k & \dots & N_{AO},l=N_t \end{pmatrix}} = \underset{\hat{\bar{v}}_m(\mathbf{x},k;l)}{\begin{pmatrix} 1,l=k & \dots & 1,l=N_t \\ \vdots & \ddots & \vdots \\ N_{AO},l=k & \dots & N_{AO},l=N_t \end{pmatrix}}$$

Figure 3.4: Schematic of iterative component of Equation (3.27) applying the finite duration implementation. The integral is reshaped such all the timesteps corresponding to a single output are assigned to a row and any time steps that exceed N_T are discarded.

$$\underset{\oint_{Srec}}{\begin{pmatrix} 1,1 & \dots & 1,N_t \\ \vdots & \ddots & \vdots \\ N_{AO},1 & \dots & N_{AO},N_t \end{pmatrix}} + \underset{\hat{\bar{v}}_m(\mathbf{x},k-1;l)}{\left(\begin{array}{ccc|c} 1,l=k & \dots & 1,l=N_t & 0 \\ \vdots & \ddots & \vdots & \vdots \\ N_{AO},l=k & \dots & N_{AO},l=N_t & 0 \end{array}\right)} = \underset{\hat{\bar{v}}_m(\mathbf{x},k;l)}{\begin{pmatrix} 1,l=k & \dots & 1,l=N_t \\ \vdots & \ddots & \vdots \\ N_{AO},l=k & \dots & N_{AO},l=N_t \end{pmatrix}}$$

Figure 3.5: Schematic of iterative component of Equation (3.27) applying the continuous operation implementation.

Finally fig. 3.5 shows the same step as fig. 3.4 for the continuous operation implementation. This implementation for continuous operation is only valid when the matrix of Green's states can be written such that for every receiver-emitter combination the impulse response representation inside the Green's state matrix includes all nonzero terms.

The functioning of and difference between the implementation of eq. (3.25) and eq. (3.26) can best be illustrated with an example. Suppose the extrapolation integral, the surface integral of eq. (3.27), for a number of time steps k is given in table 3.2 where the simulation has a duration of $k = 5$ time steps. The values at $l = k + 1$ correspond to a direct travelling wave and the values at $l = k + 3$ correspond to some reflection of that same wave.

$\oint_{Srec}$	l=k	l=k+1	l=k+2	l=k+3	l=k+4
$k=1$	0	0	0	0	0
$k=2$	0	3	0	1.5	0
$k=3$	0	2	0	1	0
$k=4$	0	1	0	0.5	0
$k=5$	0	0	0	0	0

Table 3.2: Interpolation integral example for an number of time steps.

The extrapolated velocity that would be obtained by applying eq. (3.25) using eq. (3.27) is shown in table 3.3. If however eq. (3.26) is used and $N_t = 2$ is chosen, one would obtain the extrapolated velocity that is shown in table 3.4. In both cases the value $\hat{\bar{v}}_i(\mathbf{x}^{emt}, l = k, k)$ in table 3.3 and table 3.4 respectively is applied to the boundary at each time step and the

values for $\hat{\overline{v}}_i(\mathbf{x}^{emt}, l > k, k)$ are stored for later use. Advancing k shifts the stored values and adds the new values of the integral in table 3.2 for the appropriate values of l.

$\hat{\overline{v}}_i(\mathbf{x}^{emt}, l, k)$	l=k	l=k+1	l=k+2	l=k+3	l=k+4
$k=1$	0	0	0	0	0
$k=2$	0	3	0	1.5	
$k=3$	3	2	1.5		
$k=4$	2	1.5+1			
$k=5$	1.5+1				

Table 3.3: Extrapolated velocity at $\mathbf{x}^{emt}$ in the i direction for a limited number of time steps using eq. (3.25).

$\hat{\overline{v}}_i(\mathbf{x}^{emt}, l, k)$	l=k	l=k+1	l=k+2	l=k+3	l=k+4
$k=1$	0	0	0		
$k=2$	0	3	0		
$k=3$	3	2	0		
$k=4$	2	1	0		
$k=5$	1	0	0		

Table 3.4: Extrapolated velocity at $\mathbf{x}^{emt}$ in the i direction for a number of time steps using eq. (3.26).

Table 3.3 illustrates the finite nature of eq. (3.25) and its implementation as it is not possible to continue extrapolation after $k = N_t - 1$ has been reached. Table 3.4 on the other hand shows how eq. (3.26) can operate for an arbitrary duration, however it also illustrates the importance of choosing a sufficiently large value N_{step} as the reflections that are present in the extrapolation integral are excluded and only the direct traveling wave is extrapolated.

As stated earlier, one can choose to apply $\hat{\overline{v}}_i(\mathbf{x}^{emt}, l, k)$ for any single value of $l \geqslant k$ that is included in the extrapolation integral. This can be used to compensate for delays introduced by hardware sampling, calculation times and discrete filters. This is subject to limitations as choosing too high a value for l can result in omitting nonzero parts of the extrapolation integral. If one were to apply the values at $l = k + 2$ in the example, one would compensate for 2 samples of delay but also omit the direct travelling wave from the extrapolated velocity. This also puts a limit on the minimum distance between S^{rec} and S^{emt}. This distance should be such that any delay compensation as described above does not omit any nonzero values of the extrapolation integral.

Now that the extrapolation scheme is in place, one only needs to obtain the pressure and velocity of the outward going wave at S^{rec}. If the acoustic pressure and velocity are measured directly at the same location one can obtain an estimate of the outward going pressure wave

by using

$$p^{+}(\mathbf{x}^{R},t) \approx 0.5\left[p(\mathbf{x}^{R},t) + \rho c\, v_i(\mathbf{x}^{R},t)\right] \tag{3.28}$$

and an estimate of the inward travelling wave by using

$$p^{-}(\mathbf{x}^{R},t) \approx 0.5\left[p(\mathbf{x}^{R},t) - \rho c\, v_i(\mathbf{x}^{R},t)\right]. \tag{3.29}$$

If two pressure sensors are used one must also apply eq. (2.4), which can be discretized in time to get

$$v_i(\mathbf{x}^{rec},k) \approx -\frac{\Delta t_s}{\rho d}\sum_{j=1}^{k}\left[p(\mathbf{x}_2^{rec},j) - p(\mathbf{x}_1^{rec},j)\right]. \tag{3.30}$$

At this point all the required parameters can be obtained and one can switch to implementation and evaluation evaluation in one dimensional, two dimensional and three dimensional space.

Chapter 4

One-dimensional immersive boundary condition application

4.1 Analytical evaluation

Following the assumptions made in Chapter 3, suppose a pressure signal is generated at the source speaker position $\mathbf{x}^{src}$ described by $input_p(\mathbf{x}^{src}, t)$ which results in a plane wave propagating in the direction $\mathbf{n} = [1 \quad 0 \quad 0]$. It is assumed that the acoustic pressure and velocity of a generated plane wave are perfectly recorded at point $\mathbf{x}^{rec}$ on the recording surface S^{rec} with outward normal $\mathbf{n}$. The boundary source is located at point $\mathbf{x}^{emt}$ on emitting surface S^{emt} with outward normal $\mathbf{n}$. In this case the following assumptions are made regarding the positions of $\mathbf{x}^{src}$, $\mathbf{x}^{rec}$ and $\mathbf{x}^{emt}$:

$$\begin{aligned} x_1^{src} &< x_1^{rec} < x_1^{emt} \\ x_2^{src} &= x_2^{rec} = x_2^{emt} = 0 \\ x_3^{src} &= x_3^{rec} = x_3^{emt} = 0 \end{aligned}$$

Starting with the wavefield extrapolation, one may note that eq. (3.24) can be simplified by omitting the integral over the recording surface in the one dimensional case. Secondly due to the direction of the plane wave propagation and the position of $\mathbf{x}^{src}$, $\mathbf{x}^{rec}$ and $\mathbf{x}^{emt}$, one can set the indices i and m to 1. The outward normal n_m can also be omitted as $n_1 = 1$. Finally one can replace the position vectors $\mathbf{x}^{src}$, $\mathbf{x}^{rec}$ and $\mathbf{x}^{emt}$ by their components in the 1 direction. Applying these simplifications to eq. (3.24) yields:

$$\overline{v}_i(x_1^{emt}, t) = \int_0^t \Big\{ G_1^{v,q}(x_1^{emt}, x_1^{rec}, t-\tau)\overline{v}_1(x_1^{rec}, \tau) + G_{1,1}^{v,f}(x_1^{emt}, x_1^{rec}, t-\tau)\overline{p}(x_1^{rec}, \tau) \Big\} dt. \tag{4.1}$$

The one dimensional Green's states that are used here are the free-field Green's states, as the medium is assumed to be homogeneous and infinite in the virtual domain. These are derived from the one dimensional free-field Green's function [29],

$$\hat{G}(x, s) = \frac{c_0}{2s} exp(-s\frac{|x|}{c_0}), \tag{4.2}$$

by substituting eq. (4.2) into the following equations [27],

$$\hat{G}_k^{v,q}(\mathbf{x}^R, \mathbf{x}, s) = -\partial_k^R \hat{G}(\mathbf{x}^R - \mathbf{x}, s), \tag{4.3}$$

$$\hat{G}_{l,k}^{v,f}(\mathbf{x}^R, \mathbf{x}, s) = \frac{1}{s\rho_0}\left[\partial_l^R \partial_k^R \hat{G}(\mathbf{x}^R - \mathbf{x}, s) + \delta(\mathbf{x}^R - \mathbf{x})\delta_{l,k}\right], \tag{4.4}$$

while applying the same simplifications. The full derivation is presented in Appendix B.1 and the resulting equations are

$$\hat{G}_1^{v,q}(x_1^R, x_1, t) = \frac{1}{2}\frac{x_1^R - x_1}{|x_1^R - x_1|}\delta\left(t - \frac{|x_1^R - x_1|}{c_0}\right), \tag{4.5}$$

$$G_{1,1}^{v,f}(x_1^R, x_1, s) = \frac{1}{2}\frac{1}{\rho_0 c_0}\delta\left(t - \frac{|x_1^R - x_1|}{c_0}\right). \tag{4.6}$$

Applying eqs. (4.5) and (4.6) to eq. (4.1) yields

$$\begin{aligned}\overline{v}_1(x_1^{emt}, t) = \int_0^t \Big\{ &\frac{1}{2}\frac{x_1^{emt} - x_1^{rec}}{|x_1^{emt} - x_1^{rec}|}\delta\left((t-\tau) - \frac{|x_1^{emt} - x_1^{rec}|}{c_0}\right)\overline{v}_1(x_1^{rec}, \tau) \\ &+ \frac{1}{2}\frac{1}{\rho_0 c_0}\delta\left((t-\tau) - \frac{|x_1^{emt} - x_1^{rec}|}{c_0}\right)\overline{p}(\mathbf{x}, \tau)\Big\} d\tau.\end{aligned} \tag{4.7}$$

By noting that $x_1^{emt} > x_1^{rec}$ and resolving the convolution integral one obtains

$$\overline{v}_1(x_1^{emt}, t) = \frac{1}{2}\overline{v}_1\left(x_1^{rec}, t - \frac{|x_1^{emt} - x_1^{rec}|}{c_0}\right) + \frac{1}{2}\frac{1}{\rho_0 c_0}\overline{p}\left(x_1^{rec}, t - \frac{|x_1^{emt} - x_1^{rec}|}{c_0}\right), \tag{4.8}$$

which is analogous to eq. (3.28) shifted in time. Conversely $x_1^{emt} < x_1^{rec}$ yields

$$\overline{v}_1(x_1^{emt}, t) = -\frac{1}{2}\overline{v}_1\left(x_1^{rec}, t - \frac{|x_1^{emt} - x_1^{rec}|}{c_0}\right) + \frac{1}{2}\frac{1}{\rho_0 c_0}\overline{p}\left(x_1^{rec}, t - \frac{|x_1^{emt} - x_1^{rec}|}{c_0}\right), \tag{4.9}$$

which is analogous to eq. (3.29) shifted in time.

Moving on to pressure field, i.e. eq. (3.22), the ideal desired pressure and velocity field of an outward propagating wave caused by an arbitrary pressure source can be obtained from the linearized wave equation in velocity potential. The full derivation is presented in Appendix A.1 and the resulting one dimensional equations with x_1^{src} and x_1 substituted in are respectively

$$\overline{p}(x_1, t) = input_p(t - \frac{x_1 - x_1^{src}}{c_0}) \qquad x_1 > x_1^{src}, \tag{4.10}$$

$$\overline{v}(x_1, t) = \frac{1}{\rho_0 c_0} input_p(t - \frac{x_1 - x_1^{src}}{c_0}) \qquad x_1 > x_1^{src}. \tag{4.11}$$

The analytical wavefield with rigid boundary reflection at x_1^{emt} can be calculated by mirroring the source across the rigid boundary, i.e.

$$p(x_1, t) = input_p\left(t - \frac{x_1 - x_1^{src}}{c_0}\right) + input_p\left(t + \frac{x_1 - x_1^{src}}{c_0} - 2\frac{x_1^{emt} - x_1^{src}}{c_0}\right) \qquad x_1^{emt} > x_1 > x_1^{src} \tag{4.12}$$

The pressure field resulting from the point source at x_1^{emt} on S^{emt} is obtained from eq. (3.23). Again the same simplifications that were applied to eq. (3.24) can be applied here. Doing so yields

$$p^{IBC}(x_1,t) = -\int_0^t G^{p,q}(x_1, x_1^{emt}, t-\tau)\overline{v}(x_1^{emt},\tau)d\tau \quad \text{for } x_1^{emt} > x_1 > x_1^{src}. \tag{4.13}$$

It is important to note that here $G^{p,q}$ is not the free-field Green's function

$$G^{p,q}_{free-field}(\mathbf{x}^R, \mathbf{x}, t) = \frac{1}{2}\rho c\, \delta\left(t - \frac{|x^R - x|}{c_0}\right). \tag{4.14}$$

as the reflection caused by the rigid surface must be included as well. This can be done as follows. Suppose the emitting source is spaced a distance dx from the rigid boundary at x_1^{emt}. Doing so allows one to write $G^{p,q}$ as the combination of the free-field impulse responses of the emitting source and an additional source mirrored about x_1^{emt} equal to the emitting source, i.e.

$$\begin{aligned} G^{p,q}(x_1, x_1^{emt}, t) =& \frac{1}{2}\rho c_0\, \delta\left(t - \frac{|x_1 - (x_1^{emt} - dx)|}{c_0}\right) \\ &+ \frac{1}{2}\rho c_0\, \delta\left(t - \frac{|x_1 - (x_1^{emt} + dx)|}{c_0}\right). \end{aligned} \tag{4.15}$$

As dx approaches zero, this simplifies to

$$G^{p,q}(x_1, x_1^{emt}, t) = \rho c_0\, \delta\left(t - \frac{|x_1 - x_1^{emt}|}{c_0}\right). \tag{4.16}$$

Applying eq. (4.16) to eq. (4.13) and resolving the time convolution yields

$$p^{IBC}(x_1,t) = -\rho c_0\, \overline{v}\left(x_1^{emt}, t - \frac{|x_1 - x_1^{emt}|}{c_0}\right) \quad \text{for } x_1^{emt} > x_1 > x_1^{src}. \tag{4.17}$$

Substituting eq. (4.8) into eq. (4.17) and rearranging terms yields

$$p^{IBC}(x_1,t) = -input_p\left(t + \frac{x_1 - x_1^{src}}{c_0} - 2\frac{x_1^{emt} - x_1^{src}}{c_0}\right) \quad \text{for } x_1^{emt} > x_1 > x_1^{src}. \tag{4.18}$$

which perfectly cancels out the reflection caused by the rigid boundary in eq. (4.12). This also means that the pressure signal recorded at x_1^{rec} only contains the forward propagating pressure wave.

When implementing this algorithm, errors may be introduced at various points depending on the specific hardware implementation. The physical one dimensional waveguide is discussed in the next section.

4.2 Physical one-dimensional waveguide setup

A schematic of the physical waveguide setup is shown in fig. 4.1. The physical setup consists of a cylindrical waveguide constructed out of Spirobuis air duct sections connected with couplers and closed with end caps. Both end caps have a plastic speaker enclosure attached to it in which a TB-Speaker W2-2040S 2" subwoofer is mounted, shown in fig. 4.3. Metal plates of 1 mm thickness are attached to the speakers in order ensure that the speaker cone is flush with a rigid reflective boundary, as shown in fig. 4.4. Any gaps between the metal plate and the inside wall of the duct are filled using hot glue.

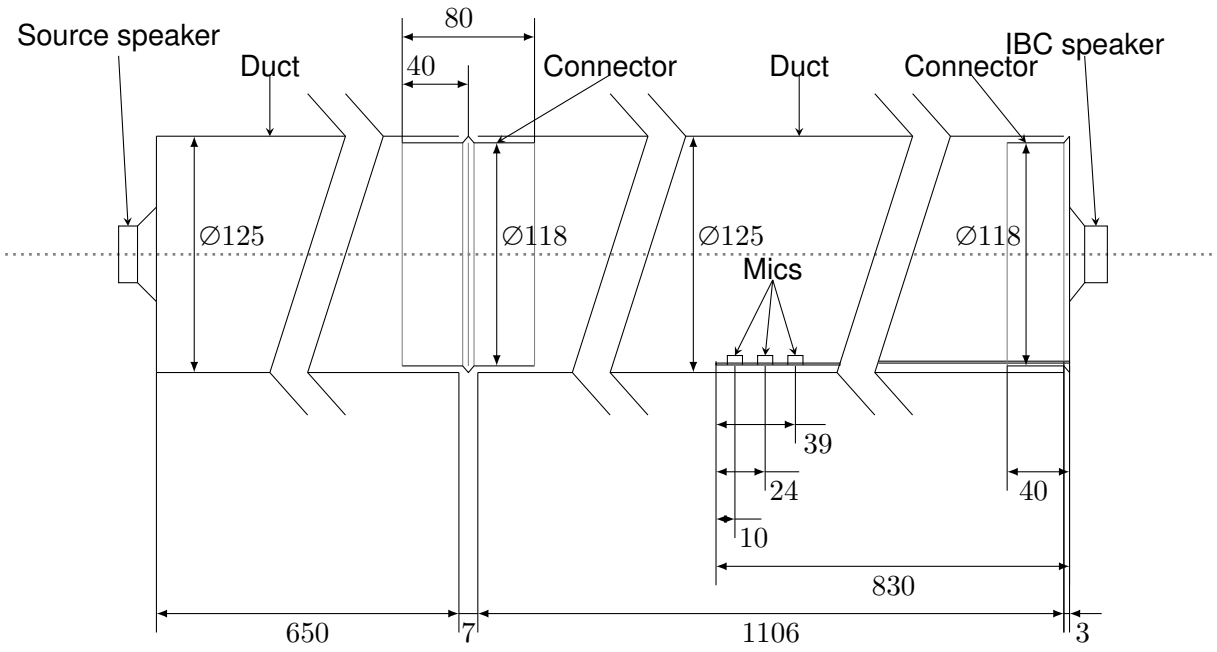

Figure 4.1: Schematic of the waveguide setup.

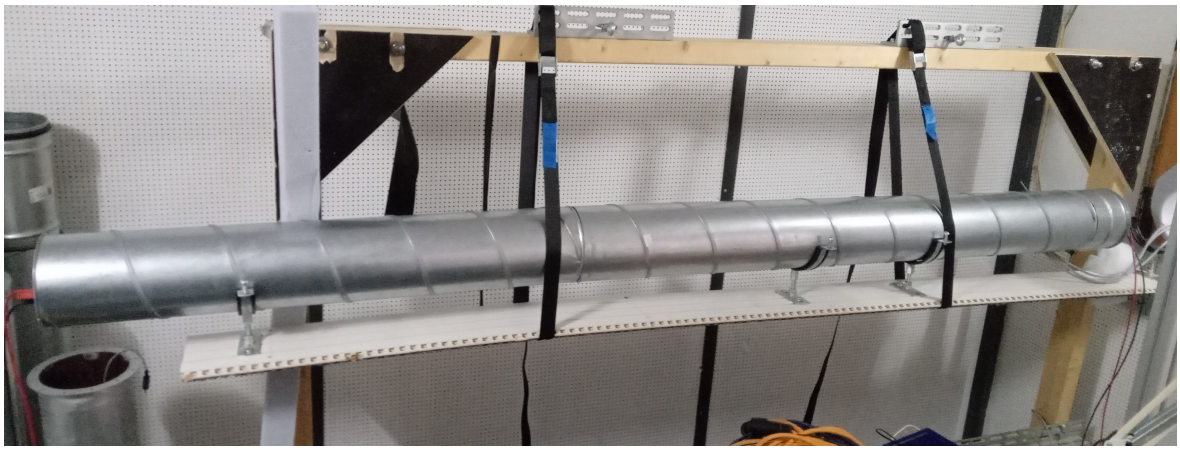

Figure 4.2: Cylindrical waveguide hardware setup used for experimental evaluation. The setup is inside the anechoic chamber in room NH127 in the Horst building of the University of Twente.

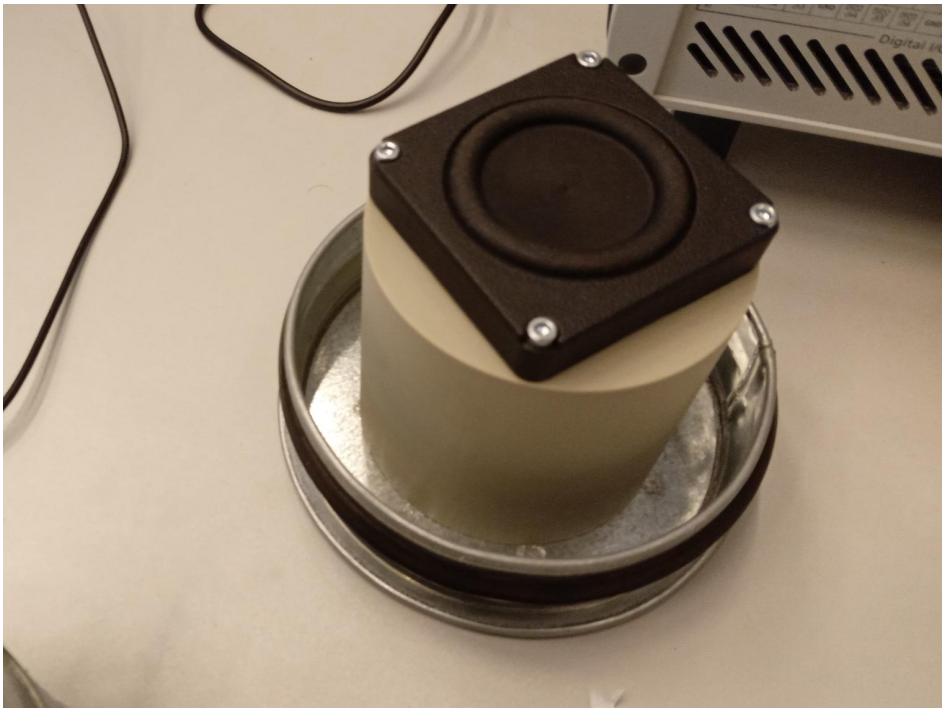

Figure 4.3: End cap with the source speaker mounted in a plastic speaker enclosure. The speaker is a TB-Speaker W2-2040S 2” sub-woofer.

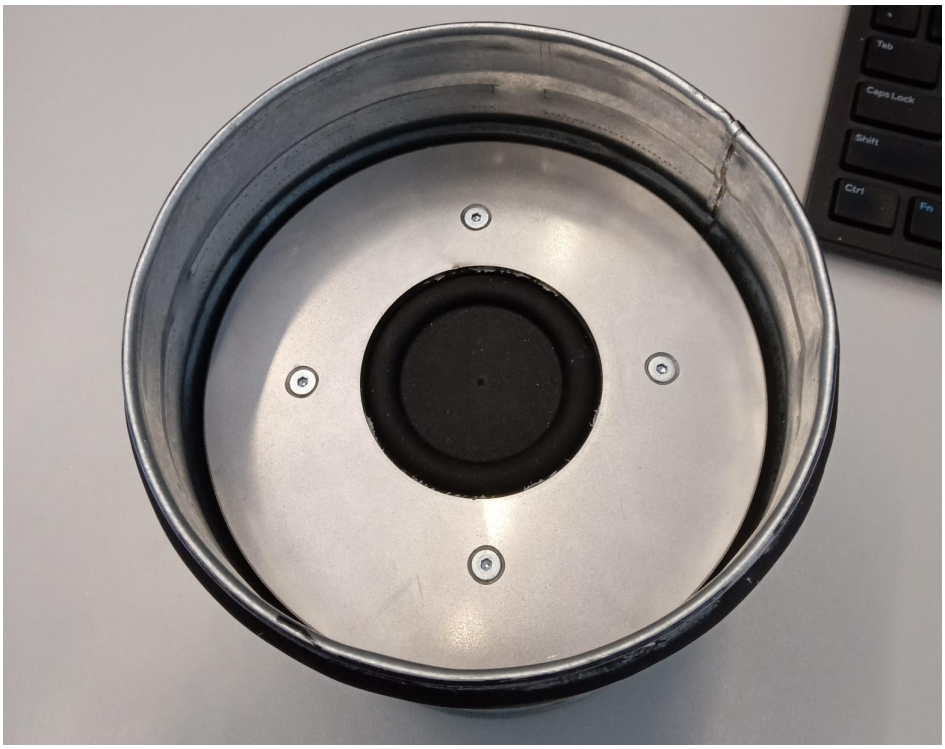

Figure 4.4: End cap containing the IBC source shown in fig. 4.3 with the metal plate and connector piece attached.

The microphones are powered by two 1.5 Volt batteries and are connected to a microphone amplifier. The speakers are powered by XA 12.2 amplifier with an amplification factor of 100 powered by a solid state regulated DC power supply. Both the speaker amplifier and the microphone amplifier are connected to a DSpace MicroLabBox which is connected to a Dell PC. The DSpace MicroLabBox is controlled using dSPACE Controldesk 6.0, the implementation of the control scheme is done in Simulink and further processing is done in Matlab.

4.3 Numerical implementation

In order to evaluate the performance of the immersive boundary conditions a simplified numerical model of the setup shown in fig. 4.1 is created using a finite difference time domain (FDTD) model.

Here the FDTD method is used to discretize eqs. (3.7) and (3.9) using two separate grids staggered in space and time. This is an adaptation of the numerical Yee grid used for electrodynamics [30]–[32]. The two grids are shown in fig. 4.5, where k is the spatial index and n is the temporal index. The velocity nodes are defined at integer spatial grid points and the pressure nodes are offset by $-\frac{1}{2}\Delta x$, where Δx is the spatial grid spacing. The pressure nodes are defined at integer time steps and the velocity nodes are offset by $+\frac{1}{2}\Delta t$, where Δt is the temporal grid spacing, making the grids staggered in both space and time.

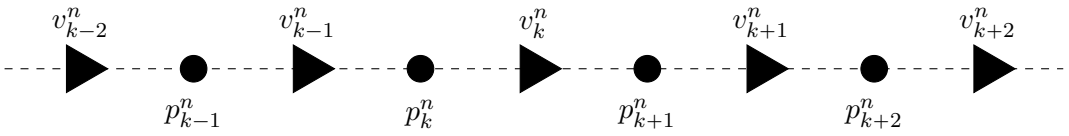

Figure 4.5: Schematic of the staggered grid used in the FDTD simulation.

By staggering the grids in this way one can define boundary conditions in the velocity grid at the exact integer spatial nodes while obtaining the pressure values at integer time steps. Using these grids to discretize eqs. (3.7) and (3.9) results in the following update equations:

$$\begin{aligned} v_k^{n+1} =& v_k^n - \frac{\Delta t}{\rho_0 \Delta x}\left(p_{k+1}^n - p_k^n\right), \\ p_k^{n+1} =& p_k^n - \frac{\Delta t}{\kappa_0 \Delta x}\left(v_k^n - v_{k-1}^n\right). \end{aligned}$$

The difference in magnitude between the pressure and velocity may lead to numerical inaccuracies. In order to mitigate this the velocity is regularized by multiplying with the characteristic impedance Z_0. Doing so results in the regularized update equations:

$$\begin{aligned} \tilde{v}_k^{n+1} =& \tilde{v}_k^n - \frac{c_0 \Delta t}{\Delta x}\left(p_{k+1}^n - p_k^n\right), \\ p_k^{n+1} =& p_k^n - \frac{c_0 \Delta t}{\Delta x}\left(\tilde{v}_k^n - \tilde{v}_{k-1}^n\right), \end{aligned}$$

where $\tilde{v}_k^n = Z_0 v_k^n$. The actual velocity at integer time steps can be obtained by linear interpolation of the regularized velocity divided by Z_0. A simplified numerical model of the hardware setup is created for the evaluation of the performance of the IBCs. The spatial grid spacing of the FDTD grid is set to be 1 [mm]. For stability reasons the temporal grid spacing must be chosen such that the Courant stability factor $C = c_0 \frac{\Delta t}{\Delta x} \leqslant 1$. Here $C = \frac{1}{2}$ is chosen which means that any pulses propagate to the next spatial node in two time steps. The speakers are modeled as soft pressure sources in the FDTD pressure grid, adding their pressure output to the already existing pressure at that node. The microphones are assumed to perfectly record the pressure at their locations. The reflections caused by the coupler joining the two long tube sections is omitted as the IBC system will only record and extrapolate the wavefield after the coupler. The change in crossection at the IBC speaker results in a reflection coefficient that can be calculated using

$$R = \frac{S_1 - S_2}{S_1 + S_2}, \tag{4.19}$$

where S_1 is the crossectional area inside of the tube and S_2 is the crossectional area inside of the coupler [21]. Calculating the crossectional areas and filling in eq. (4.19) yields a reflection coefficient of $R = 0.0576$. This would result in an reflected wave with an amplitude of six percent of that of the incident wave that would not be removed when the boundary conditions function perfectly. One may be able to remove this reflection using the immersive boundary conditions as the extrapolation integral can have additional extrapolation terms included to generate a sound field that could remove that reflection. In this numerical model the reflection is omitted entirely in order to better observe the cancellation of the reflection at the emitting boundary.

In order to evaluate the performance of the immersive boundary conditions, first a numerical simulation is performed with perfectly absorbing boundary conditions (PABCs) applied to the IBC boundary. The PABCs are implemented by setting the pressure value at the boundary to the pressure value recorded at its neighbouring node two time steps ago, using the fact that an impulse takes two time steps to travel to the next node due to the chosen temporal grid spacing. This simulation is compared to the analytical evaluation of eq. (4.10). The source pressure signal used is a Ricker wavelet defined by

$$Ricker(t) = \left(1 - 2\pi^2 f^2 t^2\right) e^{-\pi^2 f^2 t^2}, \tag{4.20}$$

where f is the center frequency of the wavelet [33]. Here the center frequency is chosen to be $f = 500$ Hertz and a delay of 0.005 seconds is applied.

Subsequently a simulation is performed using the IBCs and the results are compared to the numerical simulation with PABCs. The IBC is implemented using the scheme shown in figs. 3.3 and 3.5, which reduces to the schematics shown in figs. 4.6 and 4.7 when there is only one recording and one emitting point respectively. The schematic for the continuous implementation is used in order to reduce computational costs as one needs to extrapolate for fewer time steps.

$$\left(\begin{array}{c|c} \hat{G}^{vq}_{1,1} \\ \vdots \\ N_t,1 \end{array} \quad \begin{array}{c} \hat{G}^{vf}_{1,1} \\ \vdots \\ N_t,1 \end{array}\right) \left(\begin{array}{c} \hat{\bar{v}}_m(\mathbf{x},k) \\ \\ \hat{\bar{p}}(\mathbf{x},k) \end{array}\right) = \begin{array}{c} \S_{Srec} \\ \left(\begin{array}{c} 1 \\ \vdots \\ N_t \end{array}\right) \end{array}$$

Figure 4.6: One dimensional simplified version of fig. 3.3.

$$\begin{array}{c} \S_{Srec} \\ \left(\begin{array}{ccc} 1 & \dots & N_t \end{array}\right) \end{array} + \left(\begin{array}{ccc|c} l=k & \dots & l=N_t & 0 \end{array}\right) = \begin{array}{c} \hat{\bar{v}}_m(\mathbf{x},k-1;l) \\ \\ \hat{\bar{v}}_m(\mathbf{x},k;l) \end{array} \left(\begin{array}{ccc} l=k & \dots & l=N_t \end{array}\right)$$

Figure 4.7: One dimensional simplified version of fig. 3.5.

The one dimensional free-field Green's states in fig. 4.6 are evaluated for 3500 time steps using eqs. (4.5) and (4.6). The effect of the Dirac delta function is approximated numerically by $\delta(t) \approx \{1,0\}$ for $\{|t| \leqslant \frac{1}{2}\Delta t, |t| > \frac{1}{2}\Delta t\}$. The velocity is obtained using eq. (3.30), the desired pressure is obtained using eq. (3.28) and the desired velocity is obtained by dividing the desired pressure by the characteristic impedance Z_0. The extrapolated velocity is multiplied by the characteristic impedance and applied as a soft pressure source at the IBC speaker location.

The IBC simulation is repeated with Gaussian white noise added to the pressure values recorded by the simulated microphones. The amplitude of the noise signal is three percent that of the wavelet amplitude. In order to mitigate the buildup of low frequency errors in the extrapolation due to the noise, the numerical integration used in eq. (3.30) is replaced with a first order low pass Butterworth filter with a cutoff frequency of 20 Hertz and a gain such that the high frequency response equals that of an integrator.

Finally a simulation is performed where the sample frequency of the hardware and the speaker dynamics are included. The sample frequency of the hardware is $20,000$ Hertz and this is implemented by applying zero order hold to the values obtained from and introduced into the finite difference grid. It is not possible to simply reduce the temporal grid size as this will lead to numerical instability. The speaker dynamics are modeled using a lumped parameter model of the W2-2040S 2" subwoofer using the parameters provided by the manufacturer [34]. The frequency response of this continuous lumped parameter model is shown in fig. 4.8 and is discretized using the temporal grid spacing of the FDTD simulation. The velocity output of this speaker is multiplied by the impedance and applied as a soft pressure source to the pressure grid. This is only done for the IBC speaker. The gain is corrected by multiplication with a constant factor of 14 of the IBC speaker input signal and the delay is compensated by selecting the ninth element in the vector obtained from the step shown in fig. 4.7, rather than the first element highlighted in green. This compensates eight samples worth of delay. These samples are linked to the hardware sampling frequency, not

the FDTD temporal grid spacing.

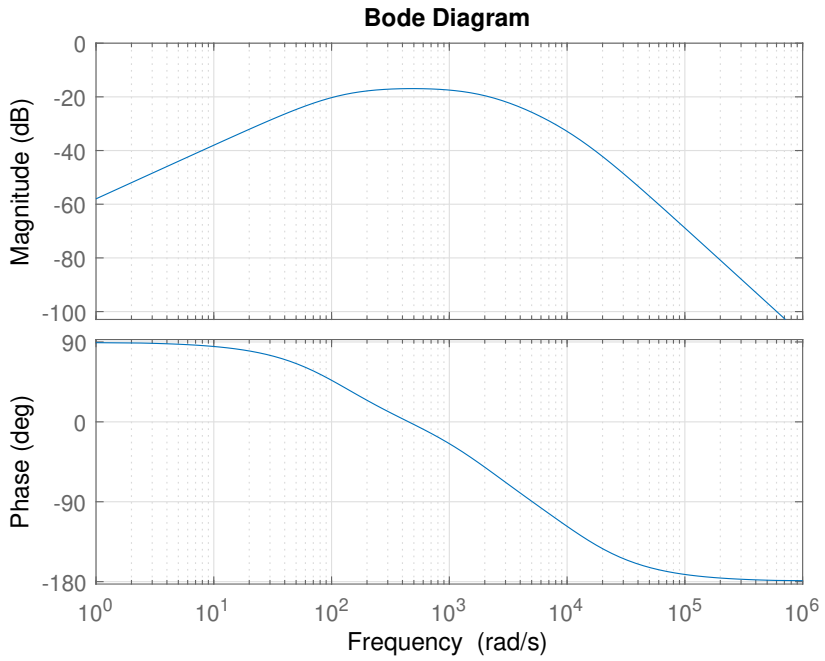

Figure 4.8: Frequency response of the continuous lumped parameter model of a W2-2040S 2" subwoofer. The input is the driving voltage and the output is the cone velocity.

4.3.1 Results

The results of the FDTD simulation with PABCs are shown in fig. 4.9. The pressure field inside the FDTD grid is shown in fig. 4.10 for the specific time instances highlighted in fig. 4.9. Figure 4.11 shows the difference between the FDTD simulation and the analytical evaluation of eq. (4.10) and fig. 4.12 shows fig. 4.11 with adjusted limits to highlight any reflections.

Figure 4.11 shows the error in the pressure distribution found in the FDTD model when compared to the analytical model. Two areas of inaccuracy can be observed. The first is the error in the forward propagating wavelet generated at $x = 0$. This error may be a result of the soft pressure source implementation. The pressure pressure introduced at the source location spreads both forward and backwards, however the rigid barrier at $x = 0$ reflects the backward travelling wave, redirecting it forward. For a nonzero distance between the source and reflector this results in a combination of two time staggered wavelets rather than a single wavelet with increased amplitude. The second area of inaccuracy can be observed in figure fig. 4.12, which shows that the perfect absorbing boundary condition does not fully eliminate the reflection. The reflection is reduced in amplitude by 128 decibels, i.e. $20 \log_{10}(5 \cdot 10^{-7})$.

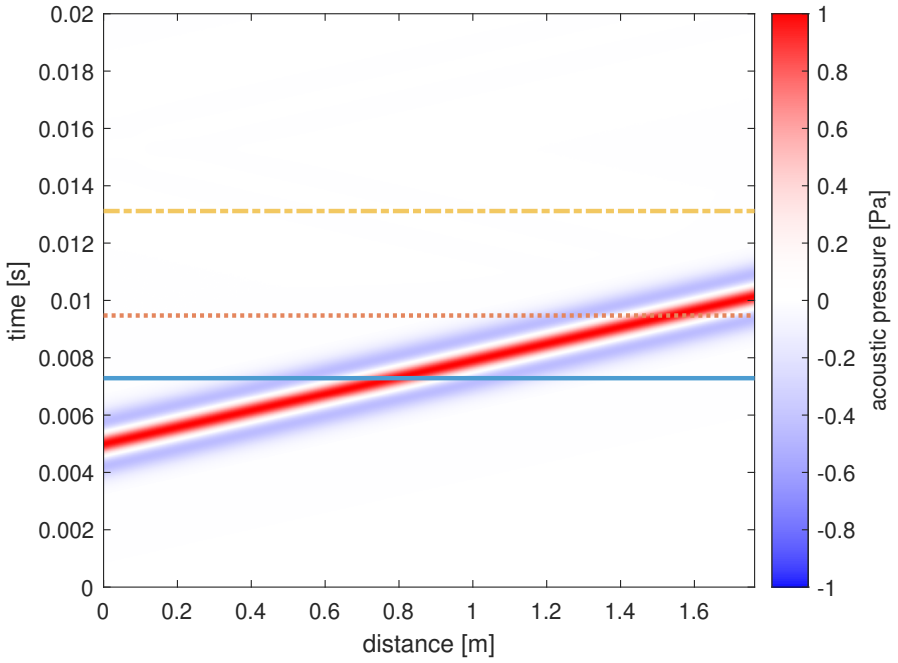

Figure 4.9: FDTD simulation of a Ricker wavelet with center frequency of 500 [Hz] propagating through the simplified waveguide with PABCs applied at the location of the IBC speaker.

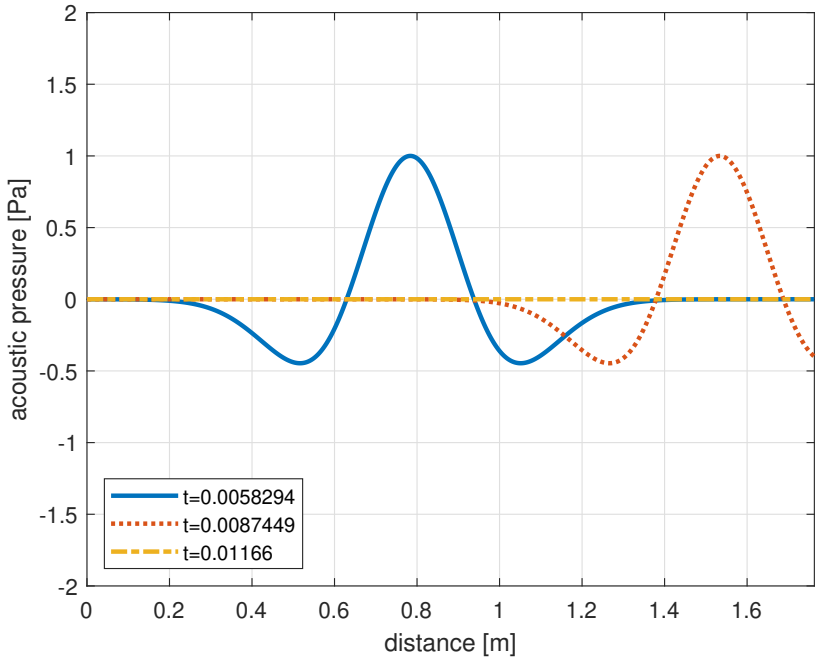

Figure 4.10: FDTD time domain pressure field inside the one-dimensional grid at the time steps highlighted in fig. 4.9.

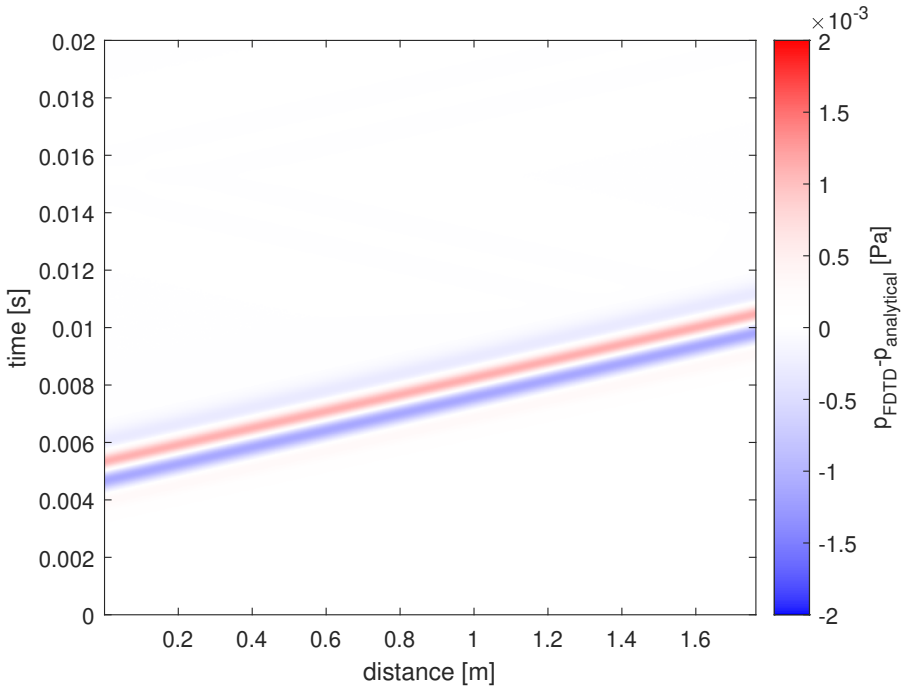

Figure 4.11: Difference between the FDTD simulation with PABCs and the analytical evaluation of eq. (4.10).

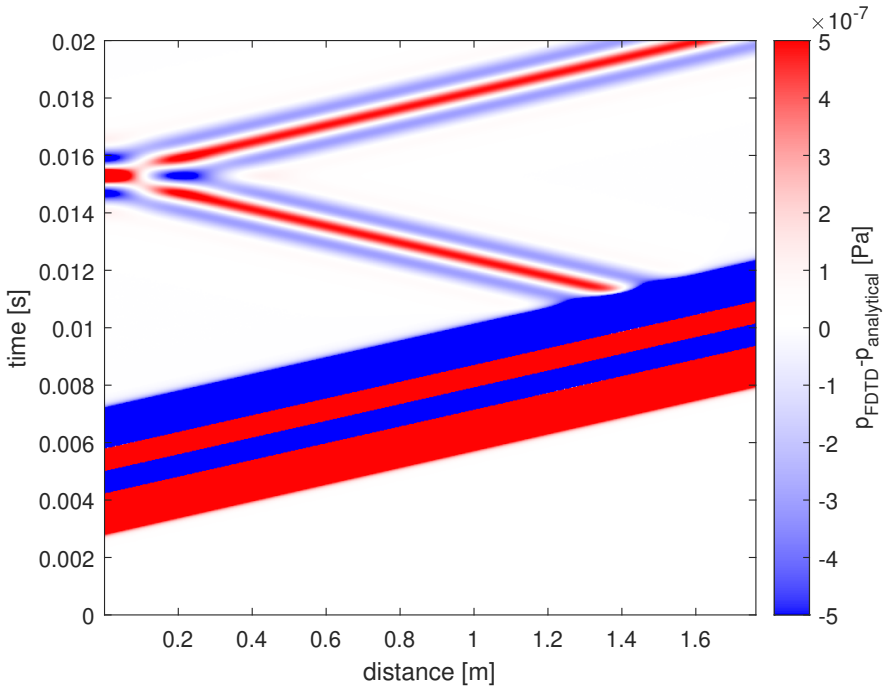

Figure 4.12: Figure 4.11 with adjusted limits to highlight any reflections.

For the purpose of evaluating the effectiveness of the immersive boundary conditions, the result obtained with the perfectly absorbing boundary conditions is used as the desired result in subsequent tests. Moving on to the first immersive boundary condition simulation, fig. 4.13 shows the result of the time domain simulation and fig. 4.14 shows the error compared to the perfectly absorbing boundary condition results. One may note that the amplitude of the reflection has only decreased by 50 decibel.

The error of the IBC simulation with noise is shown in fig. 4.15. This indicates that the presence of noise severely influences the performance of the IBCs as this results in the identification of nonexistent forward propagating waves and the subsequent generation of cancelling waves at the IBC source.

The error for the simulation with noise, hardware sampling frequency and speaker dynamics is shown in fig. 4.16. Although the operating frequency of the speaker should cover the frequencies present in the wavelet, the amplitude and phase variations in the lumped parameter model appear to severely reduce the performance of the IBCs. This may be corrected for by applying a filter that combined with the speaker dynamics yields a level amplitude and phase response in an appropriate frequency range.

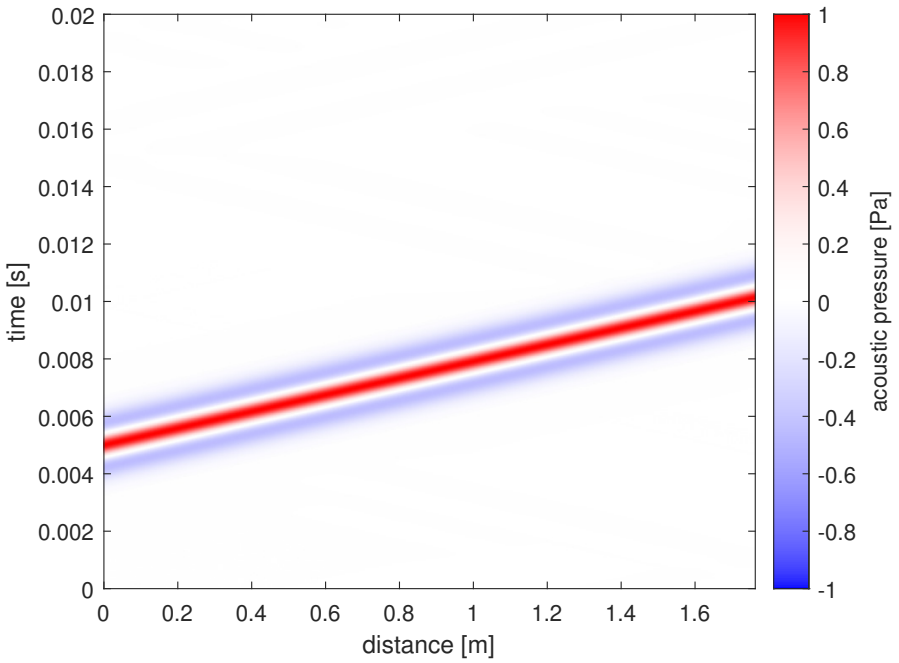

Figure 4.13: FDTD simulation of a Ricker wavelet with center frequency of 500 [Hz] propagating through the simplified waveguide with immersive boundary conditions applied.

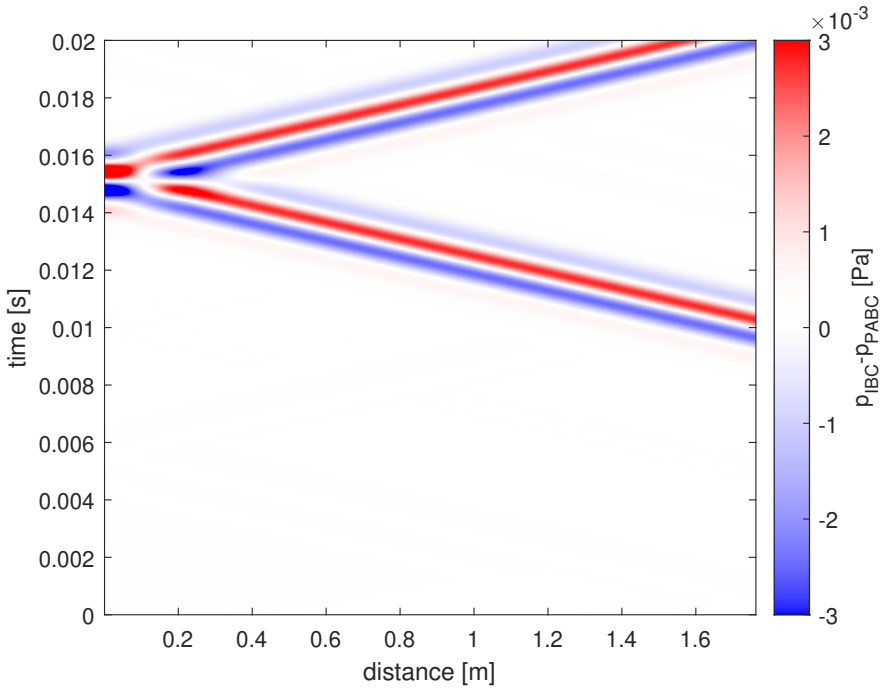

Figure 4.14: Difference between the FDTD IBC simulation and the FDTD simulation with PABCs applied.

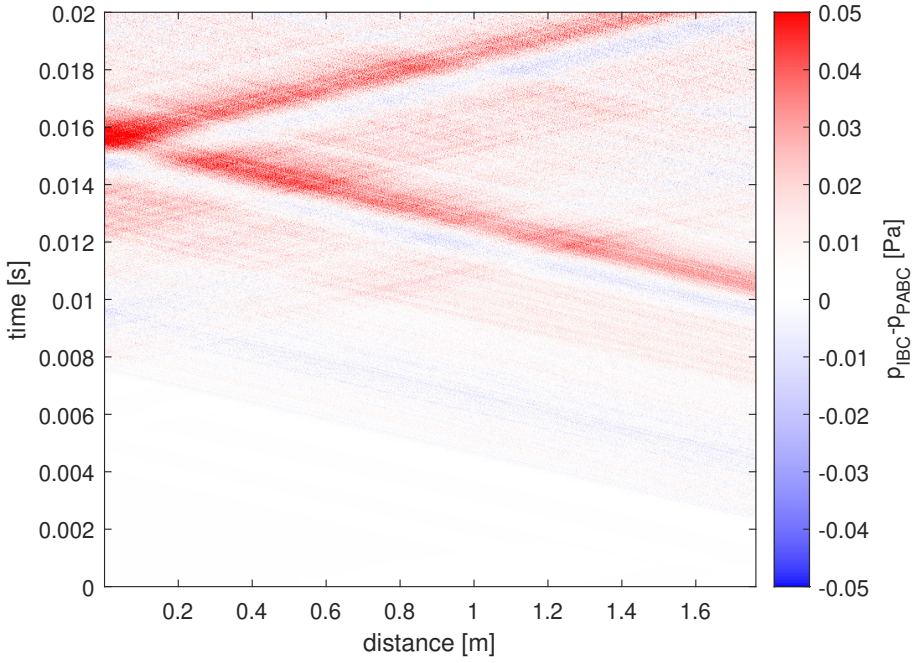

Figure 4.15: Difference between the FDTD IBC simulation with 3% white noise applied to the recorded speaker pressure signals and the FDTD simulation with PABCs applied.

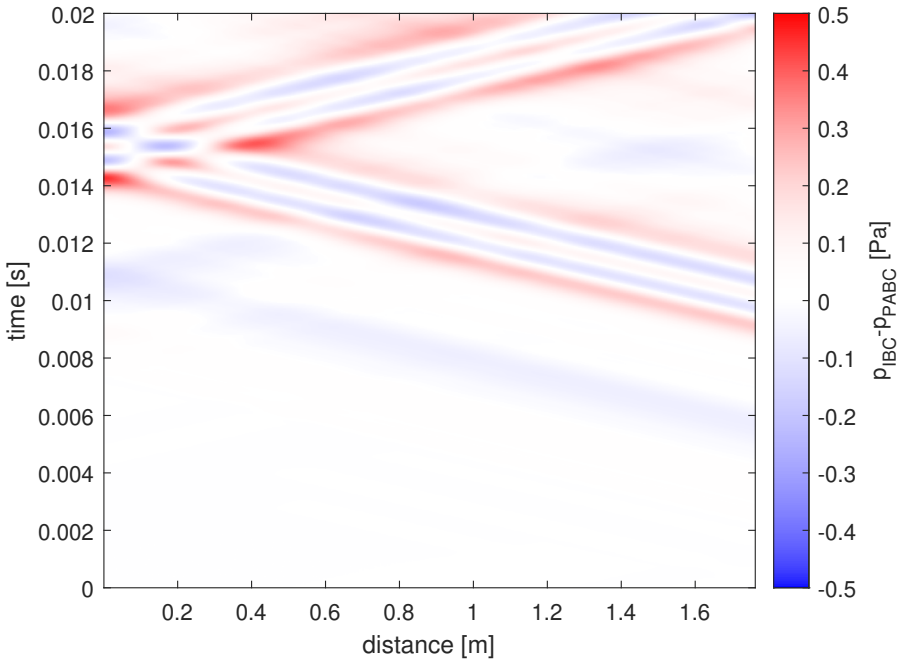

Figure 4.16: Difference between the FDTD IBC simulation, with noise and speaker dynamics and hardware sampling rate applied, and the FDTD simulation with PABCs applied.

4.4 Experimental test

In order to evaluate the performance of immersive boundary conditions using the hardware setup a continuous sine wave signal is applied to the source speaker. Both the forward and backward travelling wave are estimated at the center microphone location from the recorded signals of the three microphones using eqs. (3.28) and (3.29). The integration of eq. (3.30) is replaced with the same low pass filters used in the simulation. In order to account for gains introduced by various stages as well as delays two sliders are added in the ControlDesk environment. The first slider controls the amplitude of the signal going to the IBC speaker, the other slider control the number of time steps of delay compensation that is applied. This should account for any constant gains and delays present in the system. These sliders are adjusted until a combination is found where the estimated backward propagating wave is minimized.

4.4.1 Results

No combination of gain and delay compensation was found that resulted in a reduction of the estimated backward travelling wave without an equal reduction of the forward travelling wave. This may be the result of nonlinear dynamics of the speaker, insufficiently rigid walls of the waveguide or the wave not propagating as a plane wave due to limited distance between the speaker and the microphone array. This may be due to the speaker not covering the entire crossection of the waveguide. It was also assumed that the microphone array was sufficiently calibrated for pressure and velocity estimation, which may not be the case. These issues may be resolve by implementing filters to calibrate the speaker response, calibrating the microphone array and performing the measurement in an impedance tube.

Chapter 5

Two-dimensional immersive boundary condition application

5.1 Setup

The two dimensional numerical setup is a rectangular enclosure with rigid reflecting boundaries at its walls. The enclosure is 0.82x0.82 meter in dimension. The spatial grid spacing is set to 5 millimeter in both x and y direction in order to reduce computation time and the temporal grid spacing is calculated using

$$\Delta t = \frac{\sqrt{0.5}}{c_0\sqrt{\frac{1}{\Delta x^2} + \frac{1}{\Delta y^2}}}. \tag{5.1}$$

The sound source is placed in the center of the enclosure and has a radius of 2.5 centimeter. The source is surrounded by a circular recording surface. On the recording surface is a series points, recording the pressure and velocity using the p-p principle, with their recording direction aligned with the outward normal of the recording surface. There are 48 recording points equally spaced in the radial sense and each point consists of three microphones of which the outer two have a separation distance in the outward normal direction of 2.5 centimeter. The configuration is shown in fig. 5.1.

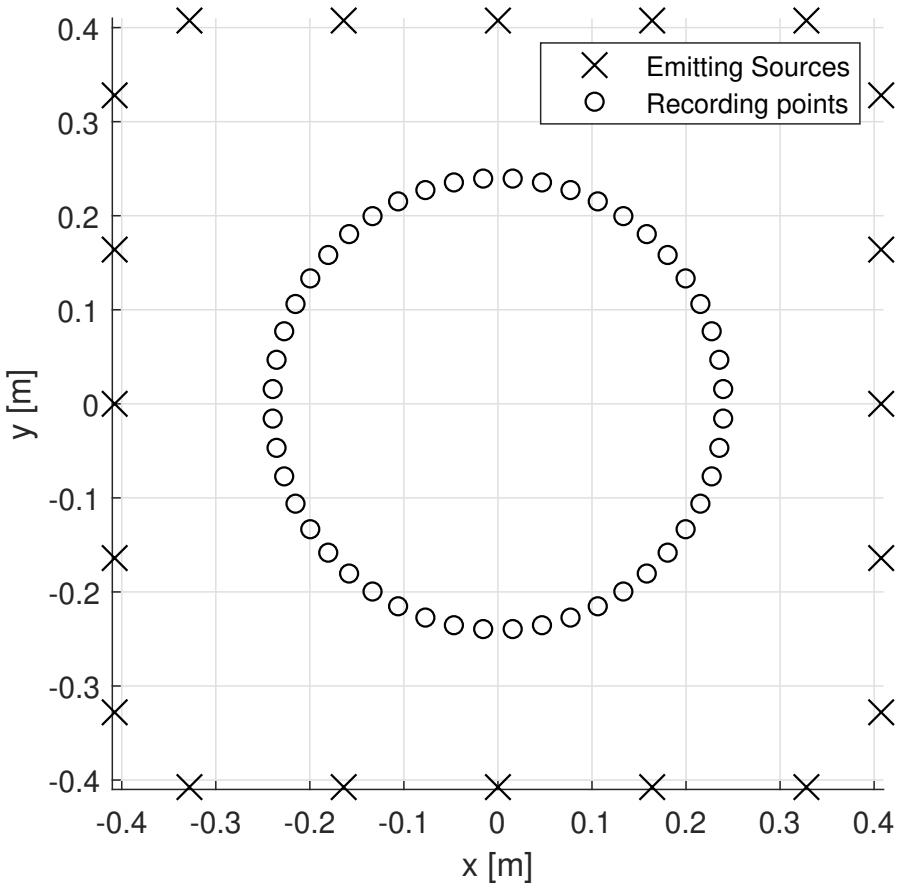

Figure 5.1: Positioning of emitting sources and recording points.

5.2 Numerical evaluation

For the two dimensional simulation one can expand the FDTD scheme used for one dimension to 2 dimensions. The derivation of the extrapolation Green's functions is presented in appendix B.2 and the resulting relevant time domain Green's state equations are

$$G_k^{v,q}(\mathbf{x}^R,\mathbf{x},t) = \frac{1}{2\pi}\frac{x_k^R - x_k}{|\mathbf{x}^R-\mathbf{x}|^2}\left(\frac{\delta\left(t-\frac{|\mathbf{x}^R-\mathbf{x}|}{c}\right)t}{\sqrt{t^2-\left(\frac{|\mathbf{x}^R-\mathbf{x}|}{c}\right)^2}} + \frac{H\left(t-\frac{|\mathbf{x}^R-\mathbf{x}|}{c}\right)}{\sqrt{t^2-\left(\frac{|\mathbf{x}^R-\mathbf{x}|}{c}\right)^2}} - \frac{H\left(t-\frac{|\mathbf{x}^R-\mathbf{x}|}{c}\right)t^2}{\sqrt{t^2-\left(\frac{|\mathbf{x}^R-\mathbf{x}|}{c}\right)^2}^3}\right), \tag{5.2}$$

$$
\begin{aligned}
G_{l,k}^{v,f} =& \frac{-1}{2\pi\rho c}\frac{1}{|\mathbf{x}^R-\mathbf{x}|}\left\{\frac{H\left(t-\frac{|\mathbf{x}^R-\mathbf{x}|}{c}\right)}{\sqrt{t^2-\left(\frac{|\mathbf{x}^R-\mathbf{x}|}{c}\right)^2}}\frac{t}{\frac{|\mathbf{x}^R-\mathbf{x}|}{c}}\right\} \\
&+\frac{1}{2\pi\rho c}\frac{(x_k^R-x_k)(x_l^R-x_l)}{|\mathbf{x}^R-\mathbf{x}|^3}\left\{\frac{H\left(t-\frac{|\mathbf{x}^R-\mathbf{x}|}{c}\right)}{\sqrt{t^2-\left(\frac{|\mathbf{x}^R-\mathbf{x}|}{c}\right)^2}}\frac{t}{\frac{|\mathbf{x}^R-\mathbf{x}|}{c}}\right\} \\
&+\frac{1}{4\pi\rho c^2}\frac{(x_k^R-x_k)(x_l^R-x_l)}{|\mathbf{x}^R-\mathbf{x}|^2}\left\{\frac{\delta\left(t-\frac{|\mathbf{x}^R-\mathbf{x}|}{c}\right)}{\sqrt{t^2-\left(\frac{|\mathbf{x}^R-\mathbf{x}|}{c}\right)^2}}-\frac{H\left(t-\frac{|\mathbf{x}^R-\mathbf{x}|}{c}\right)t}{\sqrt{t^2-\left(\frac{|\mathbf{x}^R-\mathbf{x}|}{c}\right)^2}^3}\right\} \\
&+\frac{1}{4\pi\rho c^2}\frac{(x_k^R-x_k)(x_l^R-x_l)}{|\mathbf{x}^R-\mathbf{x}|^2}\Bigg\{ \\
&\frac{\sigma_1}{\sigma_2}\delta\left(t-T_0\right)-\frac{\sigma_1 t}{\sigma_2^3}H\left(t-T_0\right)+\frac{2\sinh\left(2\cosh^{-1}\left(\frac{t}{T_0}\right)\right)H\left(t-T_0\right)}{T_0\sigma_2\sqrt{\frac{t}{T_0}-1}\sqrt{\frac{t}{T_0}+1}}\Bigg\}, \qquad (5.3) \\
\sigma_1 =& \cosh\left(2\cosh^{-1}\left(\frac{t}{T_0}\right)\right), \qquad \sigma_2=\sqrt{t^2-T_0^2} \qquad ,T_0=\frac{|\mathbf{x}^R-\mathbf{x}|}{c}.
\end{aligned}
$$

In order to verify the accuracy of these extrapolation functions a free-space simulation is performed using perfectly matched layers (PML). These PMLs are additional layers outside the original grid where a loss term is introduced whilst maintaining the same impedance, hence perfectly matched. These can be introduced in the 2D acoustic simulation by adapting the approach described by Turkel and Yefet [35]. The essence of this approach, when translated to acoustics, is that by splitting the acoustic pressure according to

$$
p = p_x + p_y, \qquad (5.4)
$$

one can arrive at the following regularized differential equations

$$
\frac{\partial \tilde{v}_x}{\partial t}+\sigma_x\tilde{v}_x = -\frac{c_0}{\rho_r}\frac{\partial p_x}{\partial x}, \qquad (5.5)
$$

$$
\frac{\partial \tilde{v}_y}{\partial t}+\sigma_y\tilde{v}_y = -\frac{c_0}{\rho_r}\frac{\partial p_y}{\partial y}, \qquad (5.6)
$$

$$
\frac{\partial p_x}{\partial t}+\sigma_x p_x = -\frac{c_0}{\kappa_r}\frac{\partial \tilde{v}_x}{\partial x}, \qquad (5.7)
$$

$$
\frac{\partial p_y}{\partial t}+\sigma_y p_y = -\frac{c_0}{\kappa_r}\frac{\partial \tilde{v}_y}{\partial y}, \qquad (5.8)
$$

where κ_r and ρ_r are the relative compressability and density defined as κ_r=κ/κ_0 and $\rho_r = \rho/\rho_0$ respectively. In this model it is assumed that the $\kappa_r = 1$ and $\rho_r = 1$. Rearranging terms

and converting to the frequency domain yields the following set of equations:

$$\tilde{v}_x = -\frac{c_0}{j\omega + \sigma_x}\frac{\partial p_x}{\partial x}, \tag{5.9}$$

$$\tilde{v}_y = -\frac{c_0}{j\omega + \sigma_y}\frac{\partial p_y}{\partial y}, \tag{5.10}$$

$$p_x = -\frac{c_0}{j\omega + \sigma_x}\frac{\partial \tilde{v}_x}{\partial x}, \tag{5.11}$$

$$p_y = -\frac{c_0}{j\omega + \sigma_y}\frac{\partial \tilde{v}_y}{\partial y}, \tag{5.12}$$

The following expressions are used for σ_x and σ_y:

$$\sigma_x(x) = \frac{1}{2\Delta t}\left(\frac{x}{L_x}\right)^3, \qquad \sigma_y(y) = \frac{1}{2\Delta t}\left(\frac{y}{L_y}\right)^3, \tag{5.13}$$

where L_x and L_y are the thickness of the perfectly matched layers and x and y are the position inside these layers. These are used to construct the following set of equations, which can be used to create update equations similar to the one dimensional case:

$$\frac{\partial}{\partial x}v_x = \frac{-j\omega}{c_0}S_x^{-1}S_y p_x, \tag{5.14}$$

$$\frac{\partial}{\partial y}v_y = \frac{-j\omega}{c_0}S_x S_y^{-1} p_y, \tag{5.15}$$

$$\frac{\partial}{\partial x}p_x = \frac{-j\omega}{c_0}S_x^{-1}S_y v_x, \tag{5.16}$$

$$\frac{\partial}{\partial y}p_y = \frac{-j\omega}{c_0}S_x S_y^{-1} v_y, \tag{5.17}$$

$$S_x(x) = 1 + \frac{\sigma(x)}{j\omega}, \tag{5.18}$$

$$S_y(y) = 1 + \frac{\sigma(y)}{j\omega} \tag{5.19}$$

The verification is of the Green's functions is performed by injecting a Ricker wavelet with a center frequency of 500 Hertz into the source region using soft pressure source nodes inside the area of the source. The estimation of the outward is performed using the same method as used in the one dimensional case, however the constant impedance is replaced with

$$Z_0 = \rho_0 c_0 \left[\frac{2rs}{2rs + c_0}\right], \tag{5.20}$$

where r is the radial distance from the origin of the cylindrical wave. This is implemented numerically by treating this impedance term as a transfer function. It and its inverse are discretized using Matlab's "c2d" function and the relevant parameters are filtered using these discretized filters. The multiplication of the Green's extrapolation functions and velocities with the outward normal vectors indicated in fig. 3.3 and fig. 3.5 are applied to the extrapolation integral in advance. The Dirac delta function implementation is modified to eliminate the presence of imaginary numbers in the signal due to the denominators in the extrapolation Green's functions. This is done by implementing the Dirac delta function as

$\delta(t) \approx \{1, 0, 0\}$ for $\{0 \leqslant t \leqslant \frac{1}{2}\Delta t \ , t > \frac{1}{2}\Delta t \ , t < 0\}$. To account for the integration over the recording surface, the Green's extrapolation functions are multiplied by the circumference of the recording surface divided by the number of recording points.

The results of the extrapolation simulation are shown in figs. 5.2 to 5.4 for the left three emitting points on the bottom edge. The other emitting points exhibit similar behaviour due to symmetry. In these figures the extrapolated velocity is divided by 10.

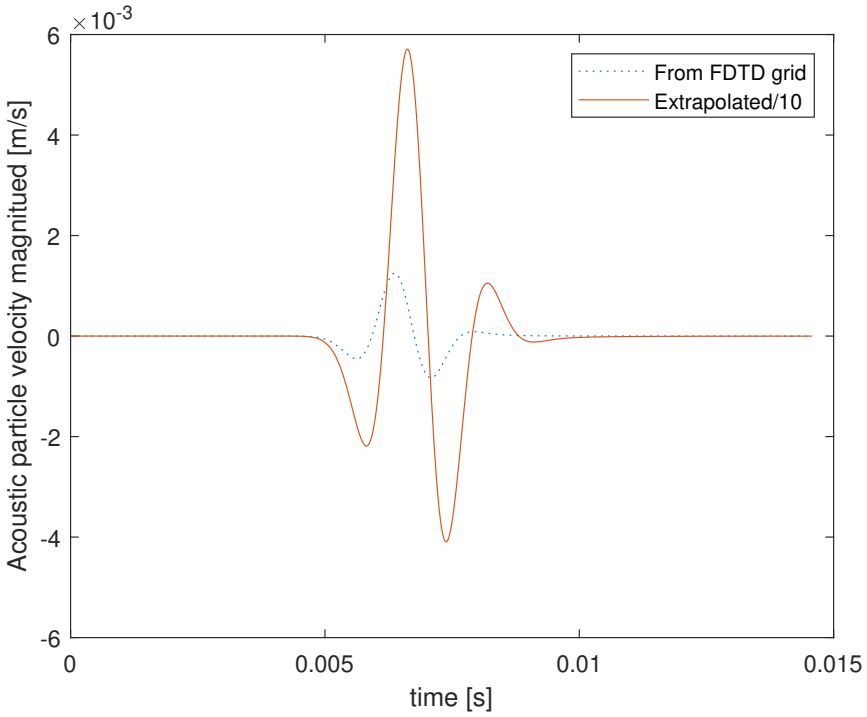

Figure 5.2: Velocity extrapolation simulation where the velocity is extrapolated to the emitting node closed to the corner on the bottom edge.

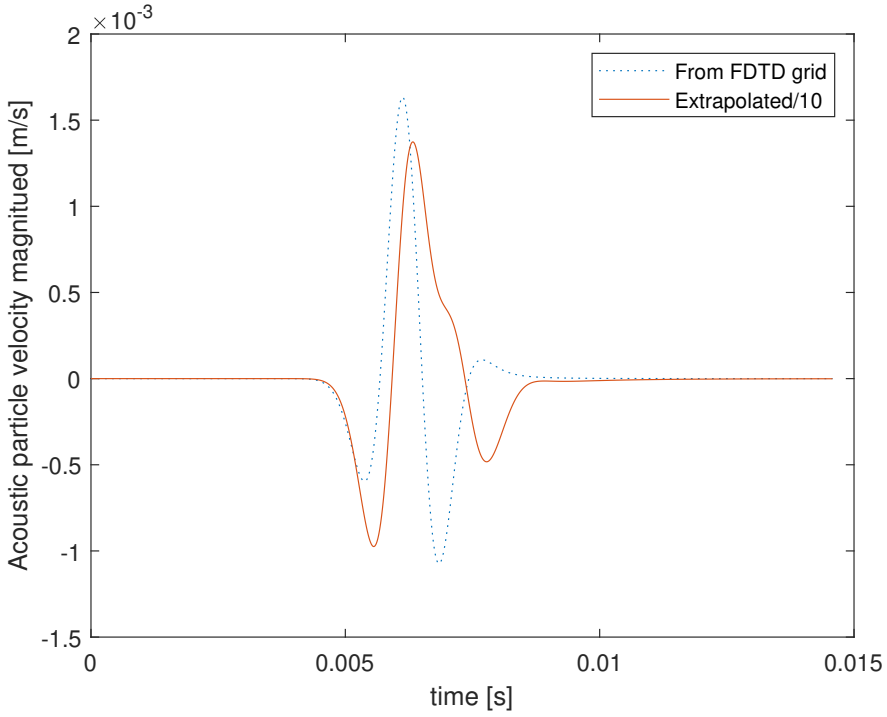

Figure 5.3: Velocity extrapolation simulation to the node between the outer and central node on the bottom edge.

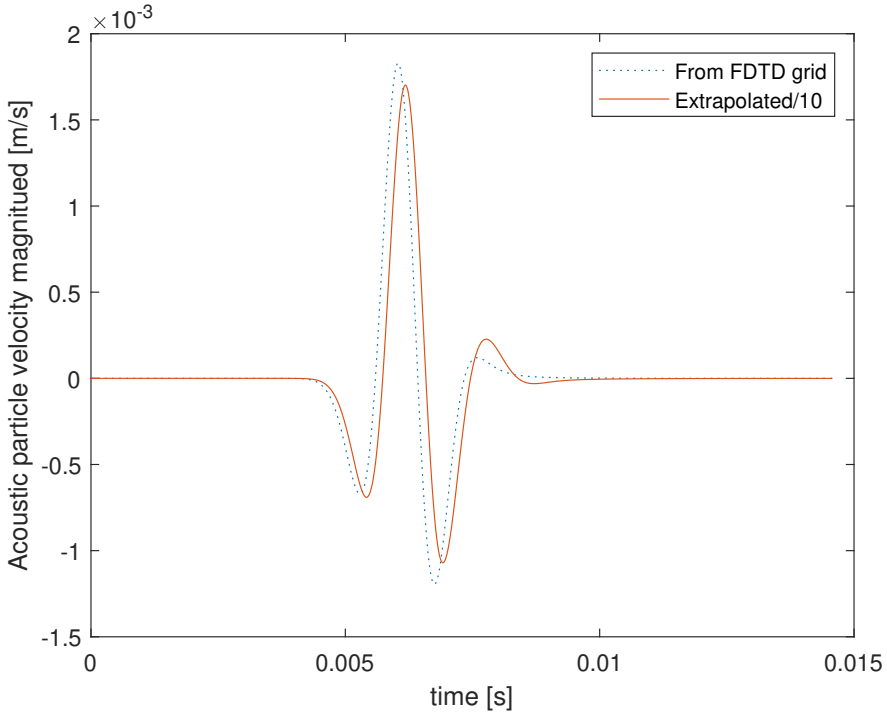

Figure 5.4: Velocity extrapolation to the central emitting node on the bottom edge.

There are significant errors in both the shape and magnitude of the extrapolated waves. The difference in magnitude and shape may be a result of the implementation of the Dirac delta function and its interaction with the temporal terms in the denominator of elements of the extrapolation Green's functions.

In order to be able to investigate the effect of limiting the number of soft sources used on the emitting boundary, the magnitude of the velocity is recorded in a separate simulation using perfectly matched layers to cancel the reflection. Then the recorded velocity signals are multiplied by the impedance and applied to the appropriate pressure nodes as soft pressure sources. The amplitudes of the soft pressure sources are scaled with the ratio of edge nodes covered.

When all 656 nodes at the boundary are populated by emitting nodes, the resulting simulation is shown in figs. 5.5 to 5.7. When only one 20 nodes have IBC pressure sources applied, the results are shown in figs. 5.8 to 5.10.

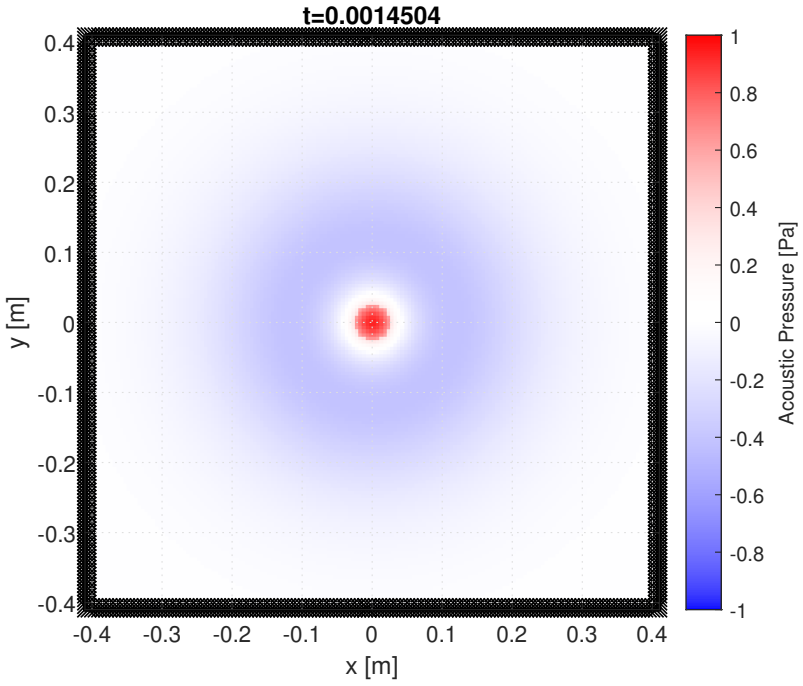

Figure 5.5: Single frame of the simulation of immersive boundary conditions with pressure sources at all nodes on the edge of the grid.

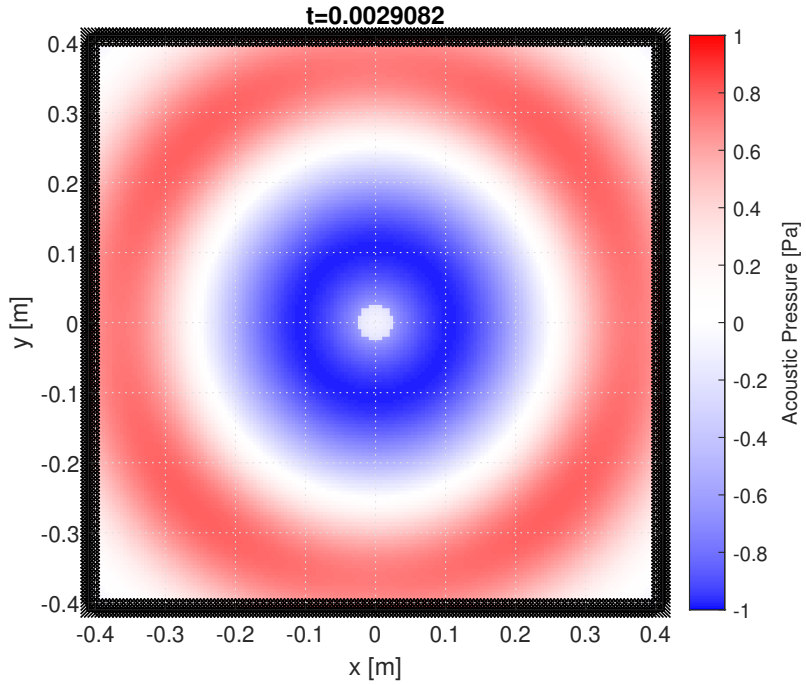

Figure 5.6: Single frame of the simulation of immersive boundary conditions with pressure sources at all nodes on the edge of the grid.

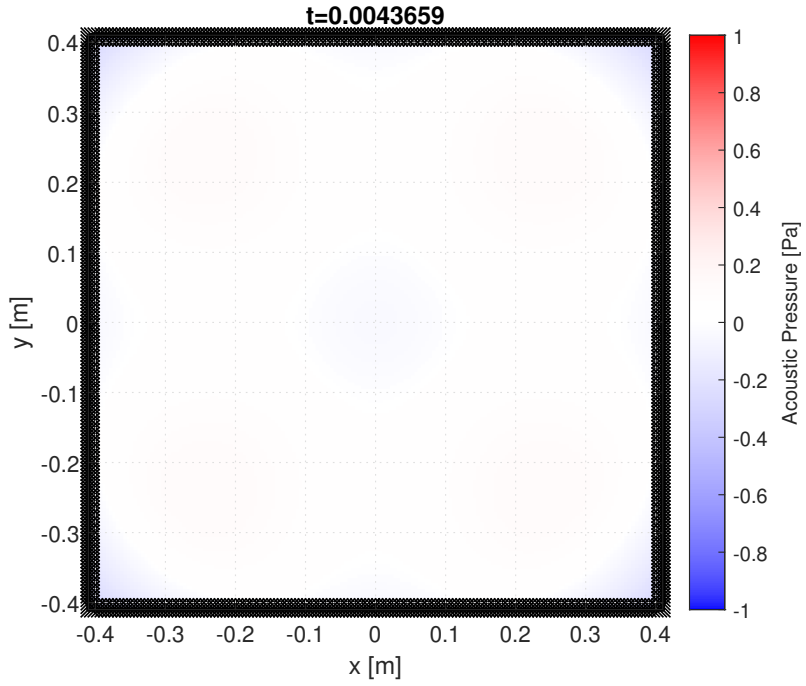

Figure 5.7: Single frame of the simulation of immersive boundary conditions with pressure sources at all nodes on the edge of the grid.

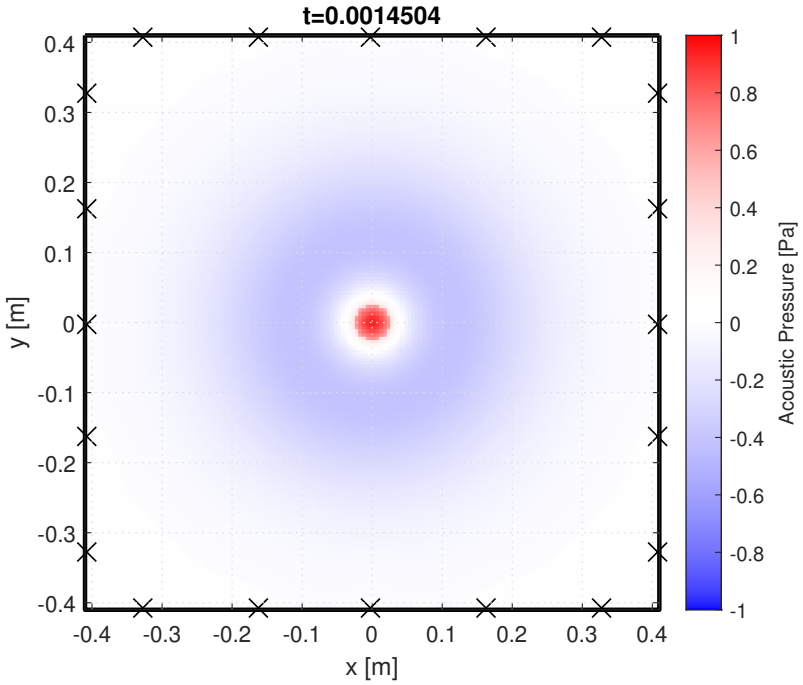

Figure 5.8: Single frame of the simulation of immersive boundary conditions with 5 emitting pressure sources per edge.

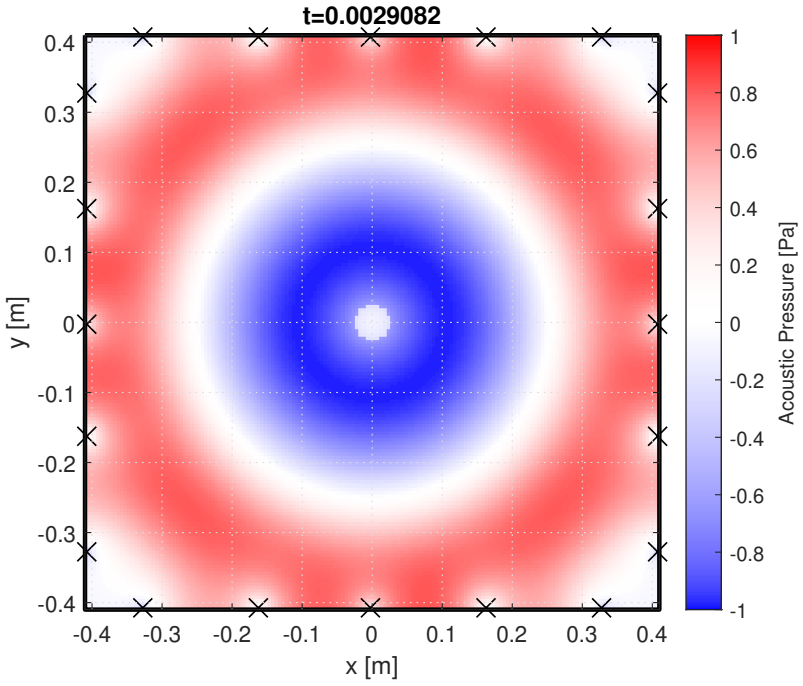

Figure 5.9: Single frame of the simulation of immersive boundary conditions with 5 emitting pressure sources per edge.

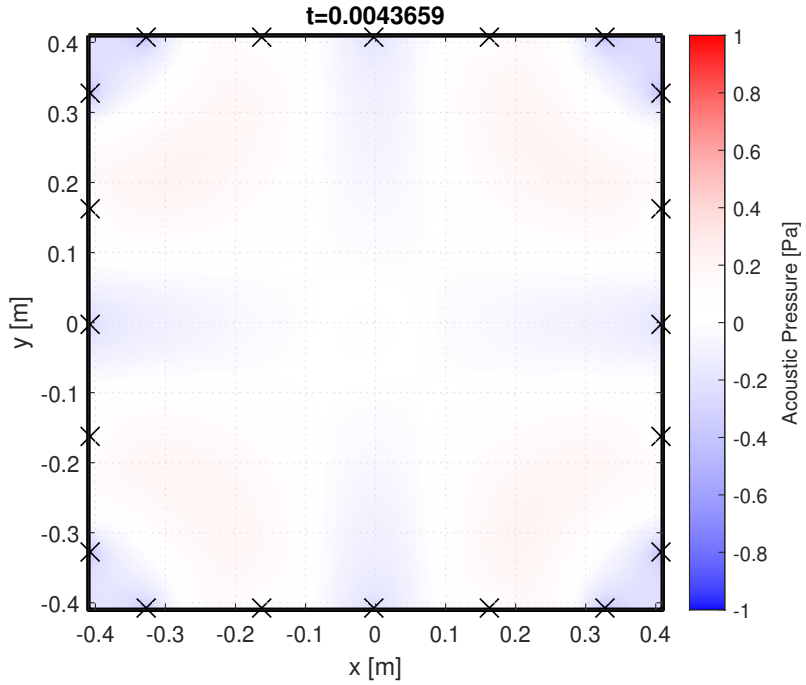

Figure 5.10: Single frame of the simulation of immersive boundary conditions with 5 emitting pressure sources per edge.

This suggests that a significant reduction in reflected wave may be achieved with a significantly reduced number of IBC sources, provided one can accurately extrapolate the wavefield velocity. This does not account for source directivity or near field radiation patterns of acoustic transducers that would be used in a hardware setup. In addition the issues identified in the one dimensional setup need to be addressed as well as the possibility that the assumed rigid boundary where no speakers are present may exhibit frequency dependent reflective behaviour in the frequency range of interest.

Chapter 6

Three-dimensional immersive boundary condition application

6.1 Setup

In order to evaluate the three dimensional implementation a Ricker wavelet with a center frequency of 500 Hertz is generated at a spherical pressure source with a radius of 5 centimeter. The recording surface has a radius of 24 centimeter and is populated by 200 points where the pressure and velocity are obtained. The distribution of nodes is generated using the algorithm developed by Deserno [36] and is shown in fig. 6.1. The pressure and velocity are obtained analytically from velocity potential relations, which results in the following equations for pressure and velocity:

$$p(r,t) = \frac{r_0}{r} input_p\left(t - \frac{r - r_0}{c_0}\right)., \tag{6.1}$$

$$v_r(r,t) = \frac{1}{\rho_0 c_0}\frac{r_0}{r}\left[input_p\left(t - \frac{r - r_0}{c_0}\right) + \frac{c_0}{r} Input_p\left(t - \frac{r - r_0}{c_0}\right)\right].. \tag{6.2}$$

The full derivation of eqs. (6.1) and (6.2) is presented in appendix A.3. The emitting surface is constructed from a similar sphere with a radius of 1 meter with 800 points populating the surface. The wavefield velocity amplitude will be extrapolated to the nodes on the emitting sphere for one quadrant. This is done using the extrapolation scheme of figs. 3.3 to 3.5 with the following Green's states:

$$G_k^{v,q}(\mathbf{x}^R, \mathbf{x}, t) = \frac{1}{4\pi c}\frac{x_k^R - x_k}{|\mathbf{x}^R - \mathbf{x}|^2}\frac{\partial}{\partial t}\delta(t - \frac{|\mathbf{x}^R - \mathbf{x}|}{c}) + \frac{1}{4\pi}\frac{x_k^R - x_k}{|\mathbf{x}^R - \mathbf{x}|^3}\delta(t - \frac{|\mathbf{x}^R - \mathbf{x}|}{c}), \tag{6.3}$$

$$\begin{aligned} G_{l,k}^{v,f}(\mathbf{x}^R, \mathbf{x}, t) = &\left(\frac{1}{4\pi\rho c^2}\frac{(x_k^R - x_k)(x_l^R - x_l)}{|\mathbf{x}^R - \mathbf{x}|^3}\right)\frac{\partial}{\partial t}\delta(t - \frac{|\mathbf{x}^R - \mathbf{x}|}{c}) \\ &+ \left(-\frac{1}{4\pi\rho c|\mathbf{x}^R - \mathbf{x}|^2} + 3\frac{(x_k^R - x_k)(x_l^R - x_l)}{4\pi\rho c|\mathbf{x}^R - \mathbf{x}|^4}\right)\delta(t - \frac{|\mathbf{x}^R - \mathbf{x}|}{c}) \\ &+ \left(-\frac{1}{4\pi\rho|\mathbf{x}^R - \mathbf{x}|^3} + 3\frac{(x_k^R - x_k)(x_l^R - x_l)}{4\pi\rho|\mathbf{x}^R - \mathbf{x}|^5}\right)\int\delta(t - \frac{|\mathbf{x}^R - \mathbf{x}|}{c})dt. \end{aligned} \tag{6.4}$$

The full derivation of these Green's states is presented in appendix B.3. In order to account for the surface integral over the surface of a sphere, the Green's functions are scaled by the surface area of the sphere divided by the number of recording points.

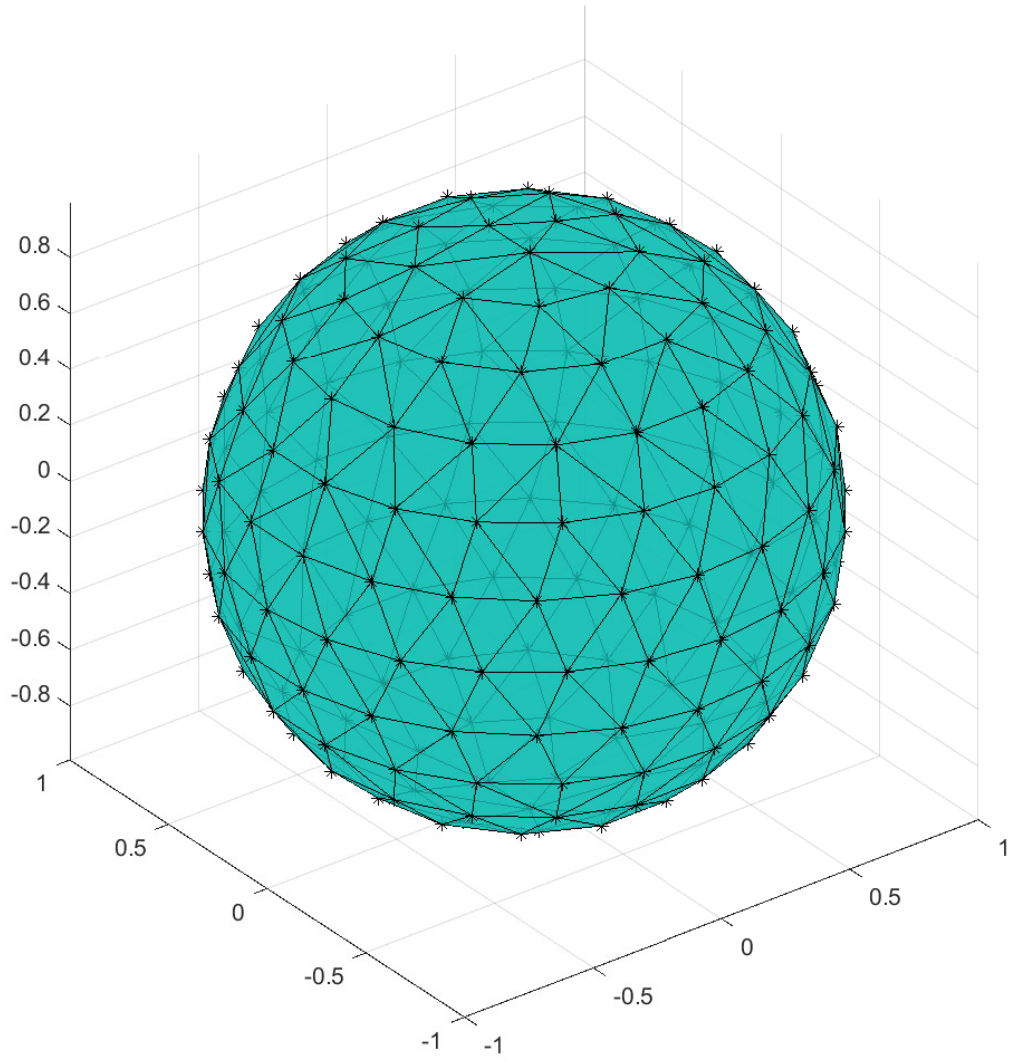

Figure 6.1: Node distribution of the recording sphere with normalized coordinates.

6.2 Numerical extrapolation implementation

The derivative and integral terms of the Dirac delta functions in the convolution context complicate the implementation of the iterative scheme, however this can be mitigated by applying the following property of the Dirac delta distribution:

$$\dot{\delta} * f = \delta * \dot{f}, \tag{6.5}$$

where $*$ corresponds to the convolution and $\dot{a}$ corresponds to the time derivative of a. This same operation is extended to the time integral of the Dirac delta function. This means that the Green's state matrix in fig. 3.3 can be split into components that interact with the desired velocity and its derivative and the desired pressure, its derivative and its integral. The Green's state matrix is split up into five sections instead of the two it had previously and is multiplied by all the relevant signals and their integrals and derivatives. This results in the Greens state matrix only containing Dirac delta functions for the direct travelling wave, which means that it can be implemented using the continuous implementation of the extrapolation scheme, i.e. fig. 3.5. The derivative is obtained by central difference of the current time step and the value two time steps earlier. The integral and the unmodified values of the previous time step are used. This introduces a sample of delay that is compensated by selecting the values from the first column of the blue highlighted section of fig. 3.5 instead of the green highlighted column.
The Green's states are pre-multiplied with the appropriate outward normal vectors in order to extrapolate the magnitude of the velocity instead of the velocity components, in order to further reduce computation time as the magnitude of the velocity in the outward normal direction is the input signal for the IBC speaker.

6.3 Results

The root mean square error of the extrapolated velocities for points on the emitting surface are shown in figure fig. 6.2. The extrapolated velocity of the point with the greatest error is shown in fig. 6.3, together with the expected velocity.

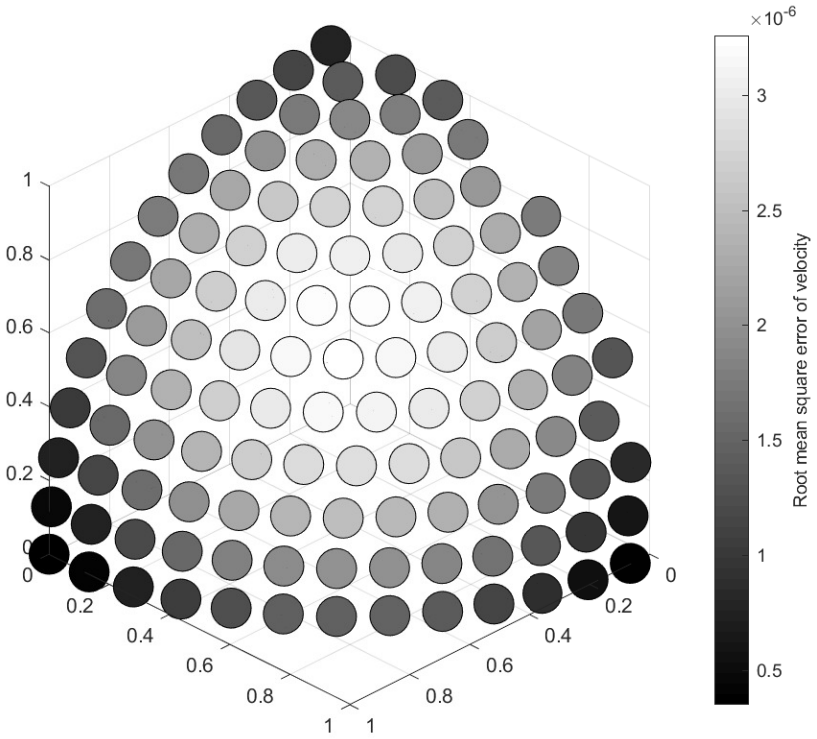

Figure 6.2: Root mean square error of the extrapolated velocity relative to the analytical velocity obtained from eq. (6.2) with additional correction applied.

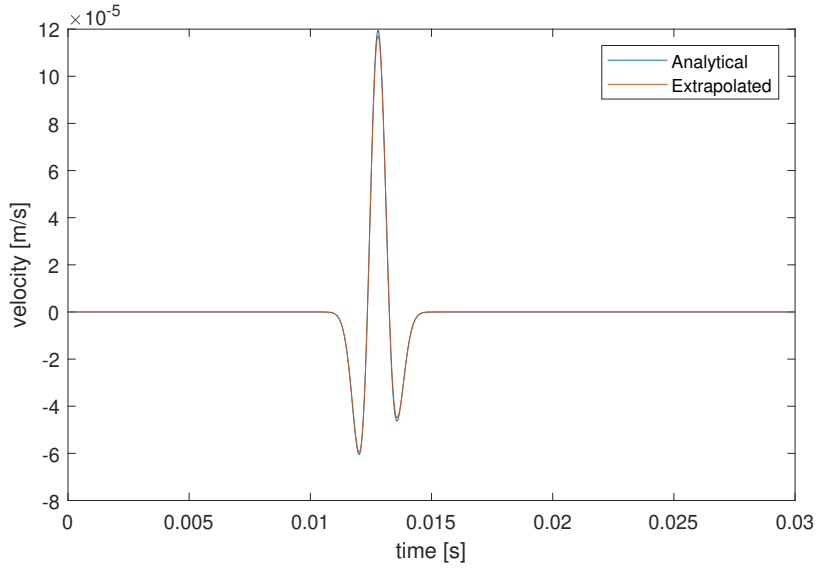

Figure 6.3: Extrapolated velocity of the node with the greatest root mean square error plotted with the expected velocity obtained from eq. (6.2).

The results indicate that the continuous implementation of the extrapolation algorithm with analytical physics-based functions can be used to obtain the desired velocity at the source locations on the emitting boundary in idealized circumstances. This assumes that the desired velocity and pressure on the recording surface do not contain any errors. The effect of the measurement method of the velocity and pressure, specifically eq. (3.28) for obtaining the outward propagating wave will introduce errors due to the impedance being frequency and position dependent, as previously mentioned in chapter 2. Additional tests can be performed to investigate the performance of the extrapolation integral for arbitrary source distributions enclosed by the recording surface.

Chapter 7

Conclusions and recommendations

7.1 Conclusions

Regarding it's suitability for low frequency vector sensor calibration, while the idea of calibrating an acoustic vector sensor inside a one dimensional waveguide may yield benefits regarding its calibration, the implementation of immersive boundary conditions to remove reflections presented in this document requires significant improvements before it can be deemed suitable for this use case. A major issue being the implementation in physical hardware. It may require significant tailoring of the hardware setup and the application of calibration filters for both the microphones and the sound sources before immersive boundary conditions can be feasibly used to actively remove reflections in real life hardware setups aimed at low frequency vector calibration.

With respect to the more general implementation of immersive boundary conditions, in heavily simplified one dimensional and three dimensional simulations it is possible to use analytical physics based extrapolation Green's functions to extrapolate the wavefield parameters required for the implementation of immersive boundary conditions to remove reflections. In these specific cases it is possible to modify the implementation such that continuous operation is possible. The two dimensional extrapolation there appear to exist large discrepancies between the extrapolated acoustic velocities and simulated free-field acoustic velocities. It is shown in a heavily simplified simulation that if the extrapolation is accurately performed, one may significantly reduce reflections with as few as twenty sound sources in a rectangular two dimensional enclosure at low frequencies.

7.2 Recommendations

Regarding future research in hardware implementation of immersive boundary conditions it will be critical to minimize undesirable behaviour of the hardware and its components, either through careful selection of hardware or the application of calibration filters or a combination thereof. This is especially true for use in calibration environment, as any errors introduced by the immersive boundary conditions implementation will hinder the calibration process.

Concerning further research of analytical immersive boundary conditions, simulations better matching real world hardware configurations can be investigated. Additional simulations can be performed to incorporate frequency dependent reflective behaviour at the boundary of the enclosure. Alternatively the continuous implementation of immersive boundary conditions can be investigated in holography and cloaking applications as well as its application in moving media.

Bibliography

[1] P. Theobald and T. Pangerc, “Review of methods for the calibration of vector sensors for the measurement of underwater acoustic fields.” NPL Report, April 2016. [Online]. Available: http://eprintspublications.npl.co.uk/7088/

[2] ISO, “Acoustics - determination of sound power levels of noise sources - guidelines for the use of basic standards,” International Organization for Standardization, Geneva, Switzerland, ISO 3740:2019, 2019.

[3] ——, “Acoustics - determination of sound power levels of noise sources using sound intensity,” International Organization for Standardization, Geneva, Switzerland, ISO 9614:2009, 2009.

[4] F. Jacobsen and H.-E. de Bree, “A comparison of two different sound intensity measurement principles,” *The Journal of the Acoustical Society of America*, vol. 118, no. 3, pp. 1510–1517, 2005. [Online]. Available: https://doi.org/10.1121/1.1984860

[5] J. Kotus and G. Szwoch, “Calibration of acoustic vector sensor based on mems microphones for doa estimation,” *Applied Acoustics*, vol. 141, pp. 307–321, 2018. [Online]. Available: https://www.sciencedirect.com/science/article/pii/S0003682X18300434

[6] A. Bokhari, A. Mousavi, B. Niu, and E. Wadbro, “Topology optimization of an acoustic diode?” *Structural and Multidisciplinary Optimization*, vol. 63, pp. 1–11, 06 2021.

[7] C. Shen, Y. Liu, and L. Huang, “On acoustic absorption mechanisms of multiple coupled quarter-wavelength resonators: Mutual impedance effects,” *Journal of Sound and Vibration*, vol. 508, p. 116202, 2021. [Online]. Available: https://www.sciencedirect.com/science/article/pii/S0022460X21002741

[8] C. Mydlarz, C. Shamoon, M. Baglione, and M. Pimpinella, “The design and calibration of low cost urban acoustic sensing devices,” 06 2015.

[9] Frederiksen, E., “Acoustic metrology - an overview of calibration methods and their uncertainties,” *Int. J. Metrol. Qual. Eng.*, vol. 4, no. 2, pp. 97–107, 2013. [Online]. Available: https://doi.org/10.1051/ijmqe/2013045

[10] E. Frederiksen, “Infrasound calibration of measurement microphones,” *The Journal of the Acoustical Society of America*, vol. 120, no. 5, pp. 3234–3234, 2006. [Online]. Available: https://doi.org/10.1121/1.4788238

[11] T. S. Becker, D.-J. van Manen, C. M. Donahue, C. Bärlocher, N. Börsing, F. Broggini, T. Haag, J. O. A. Robertsson, D. R. Schmidt, S. A. Greenhalgh, and T. E. Blum, “Immersive wave propagation experimentation: Physical implementation and one-dimensional acoustic results,” *Phys. Rev. X*, vol. 8, p. 031011, Jul 2018. [Online]. Available: https://link.aps.org/doi/10.1103/PhysRevX.8.031011

[12] D.-J. van Manen, J. O. A. Robertsson, and A. Curtis, “Exact wave field simulation for finite-volume scattering problems,” *The Journal of the Acoustical Society of America*, vol. 122, no. 4, pp. EL115–EL121, 2007. [Online]. Available: https://doi.org/10.1121/1.2771371

[13] L. Ting and M. J. Miksis, “Exact boundary conditions for scattering problems,” *The Journal of the Acoustical Society of America*, vol. 80, no. 6, pp. 1825–1827, 1986. [Online]. Available: https://doi.org/10.1121/1.394297

[14] M. Vasmel, J. O. A. Robertsson, D.-J. van Manen, and A. Curtis, “Immersive experimentation in a wave propagation laboratory,” *The Journal of the Acoustical Society of America*, vol. 134, no. 6, pp. EL492–EL498, 2013. [Online]. Available: https://doi.org/10.1121/1.4826912

[15] M. L. Vasmel, “Immersive boundary conditions for seismic wave propagation,” Ph.D. dissertation, ETH Zürich, 2016.

[16] T. S. Becker, N. Börsing, T. Haag, C. Bärlocher, C. M. Donahue, A. Curtis, J. O. A. Robertsson, and D.-J. van Manen, “Real-time immersion of physical experiments in virtual wave-physics domains,” *Phys. Rev. Applied*, vol. 13, p. 064061, Jun 2020. [Online]. Available: https://link.aps.org/doi/10.1103/PhysRevApplied.13.064061

[17] D.-J. van Manen, M. Vasmel, S. Greenhalgh, and J. O. A. Robertsson, “Broadband cloaking and holography with exact boundary conditions,” *The Journal of the Acoustical Society of America*, vol. 137, no. 6, pp. EL415–EL421, 2015. [Online]. Available: https://doi.org/10.1121/1.4921340

[18] N. Börsing, T. S. Becker, A. Curtis, D.-J. van Manen, T. Haag, and J. O. Robertsson, “Cloaking and holography experiments using immersive boundary conditions,” *Phys. Rev. Applied*, vol. 12, p. 024011, Aug 2019. [Online]. Available: https://link.aps.org/doi/10.1103/PhysRevApplied.12.024011

[19] F. Broggini, M. Vasmel, J. O. A. Robertsson, and D.-J. van Manen, “Immersive boundary conditions: Theory, implementation, and examples,” *GEOPHYSICS*, vol. 82, no. 3, pp. T97–T110, 2017. [Online]. Available: https://doi.org/10.1190/geo2016-0458.1

[20] X. Li, J. Robertsson, A. Curtis, and D.-J. van Manen, "Compensating for source directivity in immersive wave experimentation," *The Journal of the Acoustical Society of America*, vol. 146, no. 5, pp. 3141–3158, 2019. [Online]. Available: https://doi.org/10.1121/1.5131029

[21] D. Blackstock, *Fundamentals of Physical Acoustics*, ser. A Wiley-Interscience publication. Wiley, 2000.

[22] F. Fahy, *Sound Intensity, Second Edition*. Taylor & Francis, 1995.

[23] H.-E. de Bree, P. Leussink, T. Korthorst, H. Jansen, T. S. Lammerink, and M. Elwenspoek, "The μ-flown: a novel device for measuring acoustic flows," *Sensors and Actuators A: Physical*, vol. 54, no. 1, pp. 552–557, 1996. [Online]. Available: https://www.sciencedirect.com/science/article/pii/S0924424797800131

[24] J. Thompson and D. Tree, "Finite difference approximation errors in acoustic intensity measurements," *Journal of Sound and Vibration*, vol. 75, no. 2, pp. 229–238, 1981. [Online]. Available: https://www.sciencedirect.com/science/article/pii/0022460X81903412

[25] J. Pascal and C. Carles, "Systematic measurement errors with two microphone sound intensity meters," *Journal of Sound and Vibration*, vol. 83, no. 1, pp. 53–65, 1982. [Online]. Available: https://www.sciencedirect.com/science/article/pii/S0022460X82800758

[26] S. Müller, *Measuring Transfer-Functions and Impulse Responses*. New York, NY: Springer New York, 2008, pp. 65–85. [Online]. Available: https://doi.org/10.1007/978-0-387-30441-0_5

[27] J. Fokkema and P. van den Berg, *Seismic Applications of Acoustic Reciprocity*. Elsevier Science, 2013. [Online]. Available: https://books.google.nl/books?id=uYxGBQAAQBAJ

[28] A. de Hoop, *Handbook of Radiation and Scattering of Waves: Acoustic Waves in Fluids, Elastic Waves in Solids, Electromagnetic Waves*. Academic Press, 1995.

[29] K. Watanabe, *Integral Transform Techniques for Green's Function*, ser. Lecture Notes in Applied and Computational Mechanics. Springer International Publishing, 2015. [Online]. Available: https://books.google.nl/books?id=fJ1wCAAAQBAJ

[30] D. Wilson and L. Liu, "Finite-difference, time-domain simulation of sound propagation in a dynamic atmosphere," p. 63, 05 2004.

[31] A. Taflove, *Computational Electrodynamics: The Finite-difference Time-domain Method*, ser. Antennas and Propagation Library. Artech House, 1995.

[32] K. Yee, "Numerical solution of initial boundary value problems involving maxwell's equations in isotropic media," *IEEE Transactions on Antennas and Propagation*, vol. 14, no. 3, pp. 302–307, 1966.

[33] Y. Wang, “The Ricker wavelet and the Lambert W function,” *Geophysical Journal International*, vol. 200, no. 1, pp. 111–115, 11 2014. [Online]. Available: https://doi.org/10.1093/gji/ggu384

[34] *SU-series W2-2040S*, TB-speaker. [Online]. Available: http://www.tb-speaker.com/products/w2-2040s

[35] E. Turkel and A. Yefet, “Absorbing pml boundary layers for wave-like equations,” *Applied Numerical Mathematics*, vol. 27, no. 4, pp. 533–557, 1998, special Issue on Absorbing Boundary Conditions. [Online]. Available: https://www.sciencedirect.com/science/article/pii/S0168927498000269

[36] M. Deserno, “How to generate equidistributed points on the surface of a sphere,” September 2004.

[37] A. Berkhoff, “Lecture notes in signal processing for acoustics and vibrations,” February 2013.

[38] B. M. Project, H. Bateman, A. Erdélyi, and U. S. O. of Naval Research, *Tables of Integral Transforms: Based, in Part, on Notes Left by Harry Bateman*, ser. Tables of Integral Transforms: Based, in Part, on Notes Left by Harry Bateman. McGraw-Hill, 1954, no. v. 1. [Online]. Available: https://books.google.nl/books?id=FzfvAAAAMAAJ

Appendix A

Derivation of analytical equations for outward propagating waves

In order to evaluate the estimated and extrapolated velocities obtained for the immersive boundary conditions, exact equations are derived for the one-dimensional plane, cylindrical and spherical wave for the pressure and velocity.

These equations can be derived from the velocity potential ϕ, which is related to acoustic particle velocity $\mathbf{v}$ and acoustic pressure p by

$$\mathbf{v} = \nabla\phi, \tag{A.1}$$

$$p = -\rho_0 \frac{\partial}{\partial t}\phi. \tag{A.2}$$

A.1 Plane wave

For one-dimensional plane waves propagating along the x axis of a coordinate system the second order linearized wave equation in velocity potential can be written as

$$\frac{\partial^2}{\partial x^2}\phi - \frac{1}{c_0^2}\frac{\partial^2}{\partial t^2}\phi = 0, \tag{A.3}$$

which has the following general solution:

$$\phi(x,t) = f\left(t - \frac{x}{c_0}\right) + g\left(t + \frac{x}{c_0}\right). \tag{A.4}$$

When the positive x direction is assumed to be the forward or outward direction and the backward or inward propagating wave is excluded, eq. (A.4) reduces to

$$\phi(x,t) = f\left(t - \frac{x}{c_0}\right). \tag{A.5}$$

Suppose there is a velocity potential described by $input_\phi(t)$ at x_0, i.e.

$$\phi(x_0,t) = input_\phi(t). \tag{A.6}$$

Then one can obtain an expression for function $f(t)$ by applying eq. (A.6) to eq. (A.5) as follows:

$$\begin{aligned} \phi(x_0,t) =& f\left(t-\frac{x_0}{c_0}\right), \\ input_\phi(t) =& f\left(t-\frac{x_0}{c_0}\right), \\ f\left(t\right) =& input_\phi\left(t+\frac{x_0}{c_0}\right). \end{aligned} \tag{A.7}$$

By substituting eq. (A.7) into eq. (A.5), where x is the location where one wants to know the pressure and velocity, one obtains

$$\phi(x,t) = input_\phi\left(t-\frac{x-x_0}{c_0}\right) \quad \forall\, x > x_0. \tag{A.8}$$

In case the input is a pressure $input_p(t)$ instead, one can rewrite eq. (A.2) as

$$\phi = \frac{1}{-\rho_0}\int_\infty p\, dt \tag{A.9}$$

and use it to replace the velocity potential $input_\phi(t)$ in eq. (A.8), yielding

$$\phi(x,t) = \frac{1}{-\rho_0}\int_\infty \left\{input_p\left(t-\frac{x-x_0}{c_0}\right)\right\} dt \quad \forall\, x > x_0. \tag{A.10}$$

Suppose $Input_p\left(t-\frac{x-x_0}{c_0}\right)$ is a differentiable function that is defined as $Input_p\left(t-\frac{x-x_0}{c_0}\right) = \int_\infty \left\{input_p\left(t-\frac{x-x_0}{c_0}\right)\right\} dt$. The following partial derivatives can be found for this function:

$$\frac{\partial}{\partial t} Input_p\left(t-\frac{x-x_0}{c_0}\right) = input_p\left(t-\frac{x-x_0}{c_0}\right), \tag{A.11}$$

$$\frac{\partial}{\partial x} Input_p\left(t-\frac{x-x_0}{c_0}\right) = \frac{-1}{c_0} input_p\left(t-\frac{x-x_0}{c_0}\right). \tag{A.12}$$

By applying eqs. (A.2) and (A.11) to eq. (A.10) one can obtain the pressure

$$\begin{aligned} p(x,t) =& -\rho_0 \frac{\partial}{\partial t}\phi(x,t) \\ =& -\rho_0 \frac{\partial}{\partial t}\frac{1}{-\rho_0}\int_\infty \left\{input_p\left(t-\frac{x-x_0}{c_0}\right)\right\} dt \\ =& \frac{-\rho_0}{-\rho_0}\frac{\partial}{\partial t}\int_\infty \left\{input_p\left(t-\frac{x-x_0}{c_0}\right)\right\} dt, \\ p(x,t) =& input_p\left(t-\frac{x-x_0}{c_0}\right). \end{aligned} \tag{A.13}$$

To obtain the velocity one would apply eq. (A.1) to eq. (A.10) but because this is 1 dimensional eq. (A.1) reduces to

$$v_x = \frac{\partial}{\partial x}\phi$$

which can then be applied to eq. (A.10) together with eq. (A.12) to obtain the velocity

$$\begin{aligned} v_x(x,t) =& \frac{\partial}{\partial x}\frac{1}{-\rho_0}\int_\infty \left\{ input_p\left(t-\frac{x-x_0}{c_0}\right)\right\} dt \\ =& \frac{1}{-\rho_0}\frac{\partial}{\partial x}\int_\infty \left\{ input_p\left(t-\frac{x-x_0}{c_0}\right)\right\} dt \\ =& \frac{1}{-\rho_0}\frac{\partial}{\partial x} Input_p\left(t-\frac{x-x_0}{c_0}\right) \\ =& \frac{1}{-\rho_0}\frac{-1}{c_0} input_p\left(t-\frac{x-x_0}{c_0}\right), \\ v_x(x,t) =& \frac{1}{\rho_0 c_0} input_p\left(t-\frac{x-x_0}{c_0}\right). \end{aligned} \tag{A.14}$$

Equations (A.13) and (A.14) show the standard relation between particle velocity and pressure for plane waves $p = Z_0 v$ where $Z_0 = \rho_0 c_0$ [21], as expected.

A.2 Cylindrical wave

For the one dimensional cylindrical waves the second order differential equation is

$$\frac{\partial^2}{\partial r^2}\phi + \frac{1}{r}\frac{\partial}{\partial r}\phi - \frac{1}{c_0^2}\frac{\partial^2}{\partial t^2}\phi = 0 \tag{A.15}$$

where r is the radial distance from the origin of the source [21]. This can be rewritten by grouping terms such that it resembles eq. (A.3), however doing so yields

$$\frac{\partial^2}{\partial r^2}(\sqrt{r}\phi) - \frac{1}{c_0^2}\frac{\partial^2}{\partial t^2}(\sqrt{r}\phi) + \frac{(\sqrt{r}\phi)}{4r^2} = 0, \tag{A.16}$$

which contains an additional term. If the radius r is sufficiently large, as is the case in the far field, this additional $\frac{(\sqrt{r}\phi)}{4r^2}$ can be omitted. Without this additional term the general solution becomes

$$\begin{aligned} \sqrt{r}\phi(r,t) &= f\left(t-\frac{r}{c_0}\right) + g\left(t+\frac{r}{c_0}\right), \\ \phi(r,t) &= \frac{f\left(t-\frac{r}{c_0}\right)}{\sqrt{r}} + \frac{g\left(t+\frac{r}{c_0}\right)}{\sqrt{r}}. \end{aligned} \tag{A.17}$$

By assuming the positive r direction as outward and omitting the inward travelling wave, eq. (A.17) becomes

$$\phi(r,t) = \frac{f\left(t-\frac{r}{c_0}\right)}{\sqrt{r}}. \tag{A.18}$$

Assuming that there is a velocity potential defined at r_0 described by

$$\phi(r_0,t) = input_\phi(t) \tag{A.19}$$

one can obtain an expression for $f(t)$ as follows:

$$\begin{aligned}
\phi(r_0,t) =& input_\phi\left(t\right),\\
\phi(r_0,t) =& \frac{f\left(t-\frac{r_0}{c_0}\right)}{\sqrt{r_0}},\\
input_\phi\left(t\right) =& \frac{f\left(t-\frac{r_0}{c_0}\right)}{\sqrt{r_0}},\\
\sqrt{r_0} input_\phi\left(t\right) =& f\left(t-\frac{r_0}{c_0}\right),\\
f\left(t\right) =& \sqrt{r_0}\, input_\phi\left(t+\frac{r_0}{c_0}\right).
\end{aligned} \tag{A.20}$$

Substituting eq. (A.20) into eq. (A.18) results in

$$\phi(r,t) = \frac{\sqrt{r_0}}{\sqrt{r}} input_\phi\left(t-\frac{r-r_0}{c_0}\right). \tag{A.21}$$

When the input is defined in pressure, i.e. $input_p(t)$, one can apply eq. (A.9) which combined with eq. (A.20) yields

$$\phi(r,t) = \frac{\sqrt{r_0}}{\sqrt{r}}\frac{-1}{\rho_0}\int_\infty input_p\left(t-\frac{r-r_0}{c_0}\right)dt. \tag{A.22}$$

Again one can introduce a function $Input_p$ which is defined as $Input_p\left(t-\frac{r-r_0}{c_0}\right) = \int_\infty \left\{input_p\left(t-\frac{r-r_0}{c_0}\right)\right\}dt$ which has the following partial derivatives:

$$\frac{\partial}{\partial t} Input_p\left(t-\frac{r-r_0}{c_0}\right) = input_p\left(t-\frac{r-r_0}{c_0}\right), \tag{A.23}$$

$$\frac{\partial}{\partial r} Input_p\left(t-\frac{r-r_0}{c_0}\right) = \frac{-1}{c_0} input_p\left(t-\frac{r-r_0}{c_0}\right). \tag{A.24}$$

Applying eqs. (A.2) and (A.23) to eq. (A.22) yields the pressure

$$\begin{aligned}
p(r,t) =& -\rho_0\frac{\partial}{\partial t}\phi(r,t)\\
=& -\rho_0\frac{\partial}{\partial t}\left[\frac{\sqrt{r_0}}{\sqrt{r}}\frac{-1}{\rho_0}\int_\infty input_p\left(t-\frac{r-r_0}{c_0}\right)dt\right]\\
=& \frac{-\rho_0}{-\rho_0}\frac{\sqrt{r_0}}{\sqrt{r}}\frac{\partial}{\partial t}\left[\int_\infty input_p\left(t-\frac{r-r_0}{c_0}\right)dt\right]\\
=& \frac{\sqrt{r_0}}{\sqrt{r}}\frac{\partial}{\partial t}\left[Input_p\left(t-\frac{r-r_0}{c_0}\right)\right],\\
p(r,t) =& \frac{\sqrt{r_0}}{\sqrt{r}} input_p\left(t-\frac{r-r_0}{c_0}\right).
\end{aligned} \tag{A.25}$$

To obtain the velocity one can simplify eq. (A.1) to its one dimensional version

$$v_r = \frac{\partial}{\partial r}\phi \tag{A.26}$$

and apply it to eq. (A.22) as follows:

$$
\begin{aligned}
v_r(r,t) =& \frac{\partial}{\partial r}\phi \\
=& \frac{\partial}{\partial r}\left[\frac{\sqrt{r_0}}{\sqrt{r}}\frac{-1}{\rho_0}\int_\infty input_p\left(t-\frac{r-r_0}{c_0}\right)dt\right] \\
=& \frac{-1}{\rho_0}\frac{\partial}{\partial r}\left[\frac{\sqrt{r_0}}{\sqrt{r}}\int_\infty input_p\left(t-\frac{r-r_0}{c_0}\right)dt\right] \\
=& \frac{-1}{\rho_0}\sqrt{r_0}\frac{\partial}{\partial r}\left[\frac{Input_p\left(t-\frac{r-r_0}{c_0}\right)}{\sqrt{r}}\right], \\
\frac{\partial}{\partial r}\left(\frac{N}{D}\right) =& \frac{\frac{\partial}{\partial r}N}{D}-\frac{N\frac{\partial}{\partial r}D}{D^2}, \\
N =& Input_p\left(t-\frac{r-r_0}{c_0}\right), \\
D =& \sqrt{r}, \\
v_r(r,t) =& \frac{-1}{\rho_0}\sqrt{r_0}\left[\frac{\frac{\partial}{\partial r}Input_p\left(t-\frac{r-r_0}{c_0}\right)}{\sqrt{r}}-\frac{Input_p\left(t-\frac{r-r_0}{c_0}\right)\frac{\partial}{\partial r}\sqrt{r}}{\sqrt{r}^2}\right].
\end{aligned}
$$

By applying eq. (A.24) and rearranging terms one obtains

$$
\begin{aligned}
v_r(r,t) =& \frac{-1}{\rho_0}\sqrt{r_0}\left[\frac{\frac{-1}{c_0}input_p\left(t-\frac{r-r_0}{c_0}\right)}{\sqrt{r}}-\frac{Input_p\left(t-\frac{r-r_0}{c_0}\right)\frac{1}{2\sqrt{r}}}{\sqrt{r}^2}\right] \\
=& \frac{-1}{\rho_0}\sqrt{r_0}\left[\frac{-1}{c_0}\frac{input_p\left(t-\frac{r-r_0}{c_0}\right)}{\sqrt{r}}-\frac{1}{2\sqrt{r}}\frac{Input_p\left(t-\frac{r-r_0}{c_0}\right)}{\sqrt{r}^2}\frac{-c_0}{-c_0}\right] \\
=& \frac{-1}{\rho_0}\sqrt{r_0}\left[\frac{-1}{c_0}\frac{1}{\sqrt{r}}input_p\left(t-\frac{r-r_0}{c_0}\right)-\frac{-1}{c_0}\frac{1}{\sqrt{r}}\frac{Input_p\left(t-\frac{r-r_0}{c_0}\right)}{2r}(-c_0)\right] \\
=& \frac{-1}{\rho_0}\frac{-1}{c_0}\frac{1}{\sqrt{r}}\sqrt{r_0}\left[input_p\left(t-\frac{r-r_0}{c_0}\right)-\frac{Input_p\left(t-\frac{r-r_0}{c_0}\right)}{2r}(-c_0)\right], \\
v_r(r,t) =& \frac{1}{\rho_0 c_0}\frac{\sqrt{r_0}}{\sqrt{r}}\left[input_p\left(t-\frac{r-r_0}{c_0}\right)+\frac{c_0}{2r}Input_p\left(t-\frac{r-r_0}{c_0}\right)\right]. \qquad \text{(A.27)}
\end{aligned}
$$

By comparing eqs. (A.25) and (A.27) one may note that the impedance is no longer a constant. This impedance is frequency dependent and can most easily be evaluated by converting eqs. (A.25) and (A.27) to the frequency domain using the Laplace transform and

calculating $Z = \frac{p}{v}$. Doing so yields:

$$
\begin{aligned}
p(r,s) =& \frac{\sqrt{r_0}}{\sqrt{r}} e^{-s\frac{r-r_0}{c_0}} input_p(s), \\
v_r(r,s) =& \frac{1}{\rho_0 c_0} \frac{\sqrt{r_0}}{\sqrt{r}} \left[e^{-s\frac{r-r_0}{c_0}} input_p(s) + \frac{c_0}{2r} e^{-s\frac{r-r_0}{c_0}} \frac{1}{s} input_p(s) \right] \\
=& \frac{1}{\rho_0 c_0} \frac{\sqrt{r_0}}{\sqrt{r}} e^{-s\frac{r-r_0}{c_0}} input_p(s) \left[1 + \frac{c_0}{2r} \frac{1}{s} \right] \\
=& \frac{1}{\rho_0 c_0} \left[1 + \frac{c_0}{2r} \frac{1}{s} \right] \frac{\sqrt{r_0}}{\sqrt{r}} e^{-s\frac{r-r_0}{c_0}} input_p(s) \\
=& \frac{1}{\rho_0 c_0} \left[\frac{2rs + c_0}{2rs} \right] \frac{\sqrt{r_0}}{\sqrt{r}} e^{-s\frac{r-r_0}{c_0}} input_p(s), \\
\frac{p(r,s)}{v_r(r,s)} =& \frac{\frac{\sqrt{r_0}}{\sqrt{r}} e^{-s\frac{r-r_0}{c_0}} input_p(s)}{\frac{1}{\rho_0 c_0} \left[\frac{2rs+c_0}{2rs} \right] \frac{\sqrt{r_0}}{\sqrt{r}} e^{-s\frac{r-r_0}{c_0}} input_p(s)} \\
=& \frac{1}{\frac{1}{\rho_0 c_0} \left[\frac{2rs+c_0}{2rs} \right]}, \\
Z =& \rho_0 c_0 \left[\frac{2rs}{2rs + c_0} \right] \\
Z =& Z_0 \left[\frac{2rs}{2rs + c_0} \right]
\end{aligned}
\tag{A.28}
$$

A description for periodic signals in the near field can be obtained using Bessel functions [21], which results in the following expressions for the velocity potential, acoustic pressure, acoustic particle velocity and impedance:

$$
\begin{aligned}
\phi =& \frac{H_0^{(2)}(kr)}{kH_1^{(2)}(kr_0)} e^{j\omega t}, \\
p =& -j\omega\rho_0\phi = -j\omega\rho_0 \frac{H_0^{(2)}(kr)}{kH_1^{(2)}(kr_0)} e^{j\omega t}, \\
v_r =& \frac{\partial}{\partial r}\phi = \frac{H_1^{(2)}(kr)}{H_1^{(2)}(kr_0)} e^{j\omega t}, \\
Z =& \frac{p}{v_r} = j\rho_0 c_0 \frac{H_0^{(2)}(kr)}{kH_1^{(2)}(kr)},
\end{aligned}
$$

where k is the wavenumber, j is the imaginary unit and $H_1^{(2)}$ and $H_0^{(2)}$ are Hankel functions of the second kind of orders one and zero respectively. In the far field formulation of equation eq. (A.28) one can clearly see that if r is assumed to be very large, the relation between acoustic pressure and acoustic particle velocity approaches that of the one-dimensional plane wave. This is also true for the near field formulation [21].

A.3 Spherical wave

Finally for the 1 dimensional spherical wave the second order differential equation is [21]

$$\frac{\partial^2}{\partial r^2}\phi + \frac{2}{r}\frac{\partial}{\partial r}\phi - \frac{1}{c_0^2}\frac{\partial^2}{\partial t^2}\phi = 0, \tag{A.29}$$

which can conveniently be rewritten to

$$\frac{\partial^2}{\partial r^2}(r\phi) - \frac{1}{c_0^2}\frac{\partial^2}{\partial t^2}(r\phi) = 0. \tag{A.30}$$

This has the general solution

$$\begin{aligned}\sqrt{r}\phi(r,t) &= f\left(t - \frac{r}{c_0}\right) + g\left(t + \frac{r}{c_0}\right),\\ \phi(r,t) &= \frac{f\left(t - \frac{r}{c_0}\right)}{r} + \frac{g\left(t + \frac{r}{c_0}\right)}{r}.\end{aligned} \tag{A.31}$$

Again the positive r direction is assumed to be the outward direction and the inward travelling wave is omitted yielding:

$$\phi(r,t) = \frac{f\left(t - \frac{r}{c_0}\right)}{r}. \tag{A.32}$$

One can obtain an expression for using the same method as was used for the plane and cylindrical waves, i.e.:

$$\begin{aligned}\phi(r_0,t) =& input_\phi(t),\\ \phi(r_0,t) =& \frac{f\left(t - \frac{r_0}{c_0}\right)}{r_0},\\ input_\phi(t) =& \frac{f\left(t - \frac{r_0}{c_0}\right)}{r_0},\\ r_0 input_\phi(t) =& f\left(t - \frac{r_0}{c_0}\right),\\ f(t) =& r_0\, input_\phi\left(t + \frac{r_0}{c_0}\right).\end{aligned} \tag{A.33}$$

Substituting eq. (A.33) into eq. (A.32) yields

$$\begin{aligned}\phi(r,t) =& \frac{r_0 input_\phi\left(t - \frac{r}{c_0} + \frac{r_0}{c_0}\right)}{r},\\ \phi(r,t) =& \frac{r_0}{r} input_\phi\left(t - \frac{r - r_0}{c_0}\right).\end{aligned} \tag{A.34}$$

Assuming the provided signal is $input_p(t)$ and applying eq. (A.2) yields

$$\phi(r,t) = \frac{r_0}{r}\frac{-1}{\rho_0}\int_\infty input_p\left(t - \frac{r - r_0}{c_0}\right)dt. \tag{A.35}$$

By defining a function $Input_p$ in the same manner as for the cylindrical wave one obtains the same partial derivatives as those found in eqs. (A.23) and (A.24). The pressure can be obtained by applying eqs. (A.23) and (A.26) to eq. (A.34) as follows:

$$\begin{aligned}
p(r,t) =& -\rho_0 \frac{\partial}{\partial t}\phi(r,t) \\
=& -\rho_0 \frac{\partial}{\partial t}\left[\frac{r_0}{r}\frac{-1}{\rho_0}\int_\infty input_p\left(t-\frac{r-r_0}{c_0}\right)dt\right] \\
=& \frac{-\rho_0}{-\rho_0}\frac{r_0}{r}\frac{\partial}{\partial t}\left[\int_\infty input_p\left(t-\frac{r-r_0}{c_0}\right)dt\right] \\
=& \frac{r_0}{r}\frac{\partial}{\partial t}\left[Input_p\left(t-\frac{r-r_0}{c_0}\right)\right], \\
p(r,t) =& \frac{r_0}{r} input_p\left(t-\frac{r-r_0}{c_0}\right). \qquad \text{(A.36)}
\end{aligned}$$

The velocity can be obtained by applying eqs. (A.24) and (A.26) to eq. (A.34) as follows:

$$
\begin{aligned}
v_r(r,t) =& \frac{\partial}{\partial r}\phi \\
=& \frac{\partial}{\partial r}\left[\frac{r_0}{r}\frac{-1}{\rho_0}\int_\infty input_p\left(t-\frac{r-r_0}{c_0}\right)dt\right] \\
=& \frac{-1}{\rho_0}\frac{\partial}{\partial r}\left[\frac{r_0}{r}\int_\infty input_p\left(t-\frac{r-r_0}{c_0}\right)dt\right] \\
=& \frac{-1}{\rho_0}r_0\frac{\partial}{\partial r}\left[\frac{Input_p\left(t-\frac{r-r_0}{c_0}\right)}{r}\right], \\
\frac{\partial}{\partial r}\left(\frac{N}{D}\right) =& \frac{\frac{\partial}{\partial r}N}{D}-\frac{N\frac{\partial}{\partial r}D}{D^2}, \\
N =& Input_p\left(t-\frac{r-r_0}{c_0}\right), \\
D =& r, \\
v_r(r,t) =& \frac{-1}{\rho_0}r_0\left[\frac{\frac{\partial}{\partial r}Input_p\left(t-\frac{r-r_0}{c_0}\right)}{r}-\frac{Input_p\left(t-\frac{r-r_0}{c_0}\right)\frac{\partial}{\partial r}r}{r^2}\right], \\
v_r(r,t) =& \frac{-1}{\rho_0}r_0\left[\frac{\frac{-1}{c_0}input_p\left(t-\frac{r-r_0}{c_0}\right)}{r}-\frac{Input_p\left(t-\frac{r-r_0}{c_0}\right)}{r^2}\right] \\
=& \frac{-1}{\rho_0}r_0\left[\frac{-1}{c_0}\frac{input_p\left(t-\frac{r-r_0}{c_0}\right)}{r}-\frac{Input_p\left(t-\frac{r-r_0}{c_0}\right)}{r^2}\frac{-c_0}{-c_0}\right] \\
=& \frac{-1}{\rho_0}r_0\left[\frac{-1}{c_0}\frac{1}{r}input_p\left(t-\frac{r-r_0}{c_0}\right)-\frac{1}{r}\frac{-1}{c_0}\frac{Input_p\left(t-\frac{r-r_0}{c_0}\right)}{r}(-c_0)\right] \\
=& \frac{-1}{\rho_0}r_0\frac{-1}{c_0}\frac{1}{r}\left[input_p\left(t-\frac{r-r_0}{c_0}\right)-\frac{Input_p\left(t-\frac{r-r_0}{c_0}\right)}{r}(-c_0)\right], \\
v_r(r,t) =& \frac{1}{\rho_0 c_0}\frac{r_0}{r}\left[input_p\left(t-\frac{r-r_0}{c_0}\right)+\frac{c_0}{r}Input_p\left(t-\frac{r-r_0}{c_0}\right)\right].
\end{aligned}
\tag{A.37}
$$

One may observe similar behavior for the spherical wave as was observed for the cylindrical wave. A frequency description of the impedance for spherical waves can be obtained in the

same manner as was done for the two dimensional case, i.e.:

$$
\begin{aligned}
p(r,s) =& \frac{r_0}{r} e^{-s\frac{r-r_0}{c_0}} input_p(s), \\
v_r(r,s) =& \frac{1}{\rho_0 c_0} \frac{r_0}{r} \left[e^{-s\frac{r-r_0}{c_0}} input_p(s) + \frac{c_0}{r} e^{-s\frac{r-r_0}{c_0}} \frac{1}{s} input_p(s) \right] \\
=& \frac{1}{\rho_0 c_0} \frac{r_0}{r} e^{-s\frac{r-r_0}{c_0}} input_p(s) \left[1 + \frac{c_0}{r}\frac{1}{s} \right] \\
=& \frac{1}{\rho_0 c_0} \left[1 + \frac{c_0}{r}\frac{1}{s} \right] \frac{r_0}{r} e^{-s\frac{r-r_0}{c_0}} input_p(s) \\
=& \frac{1}{\rho_0 c_0} \left[\frac{rs + c_0}{rs} \right] \frac{r_0}{r} e^{-s\frac{r-r_0}{c_0}} input_p(s), \\
\frac{p(r,s)}{v_r(r,s)} =& \frac{\frac{r_0}{r} e^{-s\frac{r-r_0}{c_0}} input_p(s)}{\frac{1}{\rho_0 c_0}\left[\frac{rs+c_0}{rs}\right] \frac{r_0}{r} e^{-s\frac{r-r_0}{c_0}} input_p(s)} \\
=& \frac{1}{\frac{1}{\rho_0 c_0}\left[\frac{rs+c_0}{rs}\right]}, \\
Z_0 =& \rho_0 c_0 \left[\frac{rs}{rs + c_0} \right]
\end{aligned}
$$

Appendix B

Green's state time domain representation derivations

In order to implement the IBCs one must extrapolate the velocity at the boundary on S^{emt} from a recording surface at S^{rec}. This can be done using equation eq. (3.24), although it can also be written in its time convolution form as

$$v_{full\_i}(\mathbf{x}^{emt},t) = \oint_{S^{rec}} [G_i^{v,q}(\mathbf{x}^R,\mathbf{x},t)] * v_{full,m}(\mathbf{x},t) + G_{i,m}^{v,f}(\mathbf{x}^R,\mathbf{x},t)] * p_{full}(\mathbf{x},t)]n_m dS. \quad \text{(B.1)}$$

In order to implement eq. (3.24) or eq. (B.1) one requires the time domain representations of the Green's states, where the frequency domain Green's states in an unbounded homogeneous medium are, according to Fokkema and van den Berg [27],

$$\hat{G}^{p,q}(\mathbf{x}^R,\mathbf{x},s) = s\rho\hat{G}(\mathbf{x}^R-\mathbf{x},s), \quad \text{(B.2)}$$

$$\hat{G}_k^{v,q}(\mathbf{x}^R,\mathbf{x},s) = -\partial_k^R\hat{G}(\mathbf{x}^R-\mathbf{x},s), \quad \text{(B.3)}$$

$$\hat{G}_l^{p,f}(\mathbf{x}^R,\mathbf{x},s) = -\partial_l^R\hat{G}(\mathbf{x}^R-\mathbf{x},s), \quad \text{(B.4)}$$

$$\hat{G}_{l,k}^{v,f}(\mathbf{x}^R,\mathbf{x},s) = \frac{1}{s\rho}\left[\partial_l^R\partial_k^R\hat{G}(\mathbf{x}^R-\mathbf{x},s) + \delta(\mathbf{x}^R-\mathbf{x})\delta_{l,k}\right]. \quad \text{(B.5)}$$

Here ∂_l^R is the spatial partial derivative with respect to position $\mathbf{x}^R$ in the l direction, $\delta_{l,k}$ is the Kronecker delta, $\delta(\mathbf{x}^R-\mathbf{x})$ is the dirac delta function and $\hat{G}(\mathbf{x},s)$ is the frequency domain Green's function corresponding to the specific domain, ie. one dimensional space, two dimensional space or three dimesnional space. Do note that for consistency the notation of de Hoop [28] is used for the Green's states.

The full derivation of the time domain representation of eqs. (B.2), (B.3) and (B.5) will be presented here. Time domain representation of eq. (B.4) is not presented here as it is not used in any of the calculations and can be obtained from the time domain representation of eq. (B.3).

Before the specific derivations are treated it is useful to first treat the spatial derivative $\partial_k^R|\mathbf{x}^R - \mathbf{x}|$, as this term will feature prominently. First one may note that $|\mathbf{x}^R - \mathbf{x}|$ can be written as

$$|\mathbf{x}^R - \mathbf{x}| = \sqrt{(x_i^R - x_i)(x_i^R - x_i)}.$$

Following the work of Berkhoff [37], one can write its spatial derivative in the k direction w.r.t. $\mathbf{x}^R$ as

$$\begin{aligned}
\partial_k^R|\mathbf{x}^R - \mathbf{x}| =& \partial_k^R\sqrt{(x_i^R - x_i)(x_i^R - x_i)} \\
=& \partial_k^R \left(x_i^R x_i^R - 2x_i^R x_i + x_i x_i\right)^{\frac{1}{2}} \\
=& \frac{1}{2}\left(x_i^R x_i^R - 2x_i^R x_i + x_i x_i\right)^{-\frac{1}{2}} \\
&+ \partial_k^R \left(x_i^R x_i^R - 2x_i^R x_i + x_i x_i\right) \\
=& \frac{1}{2}\left(x_i^R x_i^R - 2x_i^R x_i + x_i x_i\right)^{-\frac{1}{2}} \\
&+ \left(2x_k^R - 2x_k\right) \\
=& \frac{2x_k^R - 2x_k}{2\left(x_i^R x_i^R - 2x_i^R x_i + x_i x_i\right)^{\frac{1}{2}}} \\
=& \frac{x_k^R - x_k}{\sqrt{(x_i^R - x_i)(x_i^R - x_i)}}, \\
\partial_k^R|\mathbf{x}^R - \mathbf{x}| =& \frac{x_k^R - x_k}{|\mathbf{x}^R - \mathbf{x}|}.
\end{aligned} \tag{B.6}$$

B.1 One-dimensional Green's states

For the one dimensional derivations the frequency domain Green's function for one dimensional waves from an impulsive source [29] is the starting point:

$$\hat{G}(x, s) = \frac{c}{2}\frac{1}{s} exp(-s\frac{|x|}{c}). \tag{B.7}$$

Here it is assumed that wave propagates along the x or x_1 direction, i.e. $\mathbf{x}/|\mathbf{x}| = [1\ 0\ 0]^T$. Starting with $\hat{G}^{p,q}(\mathbf{x}^R, \mathbf{x}, s)$:

$$\begin{aligned}
\hat{G}^{p,q}(\mathbf{x}^R, \mathbf{x}, s) =& s\rho\hat{G}(\mathbf{x}^R - \mathbf{x}, s) \\
=& s\rho\frac{c}{2s} exp(-s\frac{|x^R - x|}{c}) \\
=& \frac{1}{2}\rho c\frac{s}{s} exp(-s\frac{|x^R - x|}{c}), \\
\hat{G}^{p,q}(\mathbf{x}^R, \mathbf{x}, s) =& \frac{1}{2}\rho c\, exp(-s\frac{|x^R - x|}{c}).
\end{aligned} \tag{B.8}$$

The time domain equation can be obtained by applying the inverse Laplace transform

$$G^{p,q}(\mathbf{x}^R, \mathbf{x}, t) = \mathcal{L}^{-1}\left\{\frac{1}{2}\rho c\, exp(-s\frac{|x^R - x|}{c}) * 1\right\} \tag{B.9}$$

Although this equation can be converted to the time domain by taking the inverse Laplace transform directly, one can also obtain the inverse by means of inspection. The relevant terms that need to be converted are:

- The exponential term that corresponds to a time shift of a function according to $\mathcal{L}\{f(t-\tau)\} = exp(-\tau s)f(s)$, i.e. $f(t-\tau) = \mathcal{L}^{-1}\{exp(-\tau s)f(s)\}$.
- The constant that takes the place of $f(s)$ corresponds to $\mathcal{L}\{\delta(t)\} = 1$ where $\delta(t)$ is the Dirac delta, i.e. $\delta(t) = \mathcal{L}^{-1}\{1\}$.

Combining these two observations and applying them results in the time domain Green's state

$$G^{p,q}(\mathbf{x}^R, \mathbf{x}, t) = \frac{1}{2}\rho c\, \delta\left(t - \frac{|x^R - x|}{c}\right). \tag{B.10}$$

Moving on to $\hat{G}_k^{v,q}(\mathbf{x}^R, \mathbf{x}, s)$:

$$\begin{aligned}
\hat{G}_k^{v,q}(\mathbf{x}^R, \mathbf{x}, s) =& -\partial_k^R \hat{G}(\mathbf{x}^R - \mathbf{x}, s) \\
=& -\partial_k^R \frac{c}{2s} exp(-s\frac{|x^R - x|}{c}) \\
=& -\frac{c}{2s}\partial_k^R exp(-s\frac{|x^R - x|}{c}) \\
=& -\frac{c}{2s} exp(-s\frac{|x^R - x|}{c})\partial_k^R \frac{-s}{c}|x^R - x| \\
=& -\frac{c}{2s} exp(-s\frac{|x^R - x|}{c})\frac{-s}{c}\partial_k^R |x^R - x|, \\
\hat{G}_k^{v,q}(\mathbf{x}^R, \mathbf{x}, s) =& \frac{1}{2} exp(-s\frac{|x^R - x|}{c})\partial_k^R |x^R - x|.
\end{aligned} \tag{B.11}$$

The remaining partial derivative has been derived earlier, however a further simplification can be made for the entire equation. As the wave only propagates in the x_1 direction, one can either set $k = 1$ or omit it altogether. Doing the latter results in the following equation:

$$\begin{aligned}
\hat{G}^{v,q}(\mathbf{x}^R, \mathbf{x}, s) =& \frac{1}{2} exp\left(-s\frac{|x^R - x|}{c}\right)\frac{x^R - x}{|x^R - x|}, \\
\hat{G}^{v,q}(\mathbf{x}^R, \mathbf{x}, s) =& \frac{1}{2}\frac{x^R - x}{|x^R - x|} exp\left(-s\frac{|x^R - x|}{c}\right).
\end{aligned} \tag{B.12}$$

The time domain can again be converted either by directly applying the inverse Laplace transform or by means of inspection. In either case the Laplace transform only affects the temporal parameters so all the other terms can be moved:

$$\begin{aligned}
\mathcal{L}^{-1}\left\{\hat{G}^{v,q}(\mathbf{x}^R, \mathbf{x}, s)\right\} =& \mathcal{L}^{-1}\left\{\frac{1}{2}\frac{x^R - x}{|x^R - x|} exp\left(-s\frac{|x^R - x|}{c}\right)\right\} \\
=& \frac{1}{2}\mathcal{L}^{-1}\left\{\frac{x^R - x}{|x^R - x|} exp\left(-s\frac{|x^R - x|}{c}\right)\right\}, \\
\mathcal{L}^{-1}\left\{\hat{G}^{v,q}(\mathbf{x}^R, \mathbf{x}, s)\right\} =& \frac{1}{2}\frac{x^R - x}{|x^R - x|}\mathcal{L}^{-1}\left\{exp\left(-s\frac{|x^R - x|}{c}\right) * 1\right\}
\end{aligned}$$

The remaining term that needs to be converted is the same as the one of previous Green's state and applying the results obtained for the previous Green's state here yields

$$\hat{G}^{v,q}(\mathbf{x}^R, \mathbf{x}, t) = \frac{1}{2}\frac{x^R - x}{|x^R - x|}\delta\left(t - \frac{|x^R - x|}{c}\right). \tag{B.13}$$

Finishing with the remaining Green's state required for extrapolation, $G^{v,f}_{l,k}(\mathbf{x}^R, \mathbf{x}, t)$, substituting eq. (4.2) into eq. (4.4) yields:

$$\hat{G}^{v,f}_{l,k}(\mathbf{x}^R, \mathbf{x}, s) = \frac{1}{s\rho}\left[\partial^R_l \partial^R_k \hat{G}(\mathbf{x}^R - \mathbf{x}, s) + \delta(\mathbf{x}^R - \mathbf{x})\delta_{l,k}\right]$$

This time it is more convenient to immediately simplify the equation by omitting k and l as both will be 1. Additionally one can also omit the $\delta(\mathbf{x}^R - \mathbf{x})\delta_{l,k}$ term as it will be zero when $x^R \neq x$, which is the case here. Doing so yields the much simpler equation

$$\hat{G}^{v,f}(\mathbf{x}^R, \mathbf{x}, s) = \frac{1}{s\rho}\partial^R \partial^R \hat{G}(\mathbf{x}^R - \mathbf{x}, s).$$

The first partial derivative has been calculated for the previous Green's state and can be substituted into the previous equation, i.e.

$$\begin{aligned}\hat{G}^{v,f}(\mathbf{x}^R, \mathbf{x}, s) =& \frac{1}{s\rho}\partial^R\left[-\frac{1}{2}\frac{x^R - x}{|x^R - x|}exp\left(-s\frac{|x^R - x|}{c}\right)\right] \\ =& \frac{-1}{2\rho s}\partial^R\left[\frac{x^R - x}{|x^R - x|}exp\left(-s\frac{|x^R - x|}{c}\right)\right].\end{aligned}$$

The remaining partial derivative can be derived as follows:

$$\begin{aligned}\partial^R(F\ S) =& S\partial^R F + F\partial^R S, \\ S =& exp\left(-s\frac{|x^R - x|}{c}\right), \\ F =& \frac{N}{D}, \\ N =& x^R - x, \\ D =& |x^R - x| = \sqrt{(x^R - x)^2},\end{aligned}$$

$$
\begin{aligned}
\partial^R F =& \partial^R \frac{N}{D} = \frac{D\partial^R N - N\partial^R D}{D^2} = \frac{\partial^R N}{D} - \frac{N\partial^R D}{D^2}, \\
\partial^R F =& \frac{1}{|x^R - x|} - \frac{(x^R - x)}{1}\frac{(x^R - x)}{|x^R - x|}\frac{1}{|x^R - x|^2} \\
=& \frac{1}{|x^R - x|} - \frac{(x^R - x)^2}{|x^R - x|^3}, \\
(x^R - x)^2 =& |x^R - x|^2, \\
\partial^R F =& \frac{1}{|x^R - x|} - \frac{|x^R - x|^2}{|x^R - x|^3} \\
=& \frac{1}{|x^R - x|} - \frac{1}{|x^R - x|} = 0,
\end{aligned}
$$

$$
\begin{aligned}
\partial^R (F\ S) =& 0 + F\partial^R S \\
=& \frac{x^R - x}{|x^R - x|} exp\left(-s\frac{|x^R - x|}{c}\right)\frac{-s}{c}\frac{x^R - x}{|x^R - x|} \\
=& \frac{(x^R - x)^2}{|x^R - x|^2}\frac{-s}{c} exp\left(-s\frac{|x^R - x|}{c}\right) \\
=& \frac{|x^R - x|^2}{|x^R - x|^2}\frac{-s}{c} exp\left(-s\frac{|x^R - x|}{c}\right), \\
\partial^R (F\ S) =& \frac{-s}{c} exp\left(-s\frac{|x^R - x|}{c}\right).
\end{aligned}
$$

Substituting into the remaining equation yields:

$$
\begin{aligned}
\hat{G}^{v,f}(\mathbf{x}^R, \mathbf{x}, t) =& \frac{-1}{2\rho s}\left[\frac{-s}{c} exp\left(-s\frac{|x^R - x|}{c}\right)\right] \\
=& \frac{1}{2\rho c} exp\left(-s\frac{|x^R - x|}{c}\right).
\end{aligned}
$$

This can be converted to the time domain by using the same steps as before due to the linearity of the Laplace transform (and its inverse). Doing so yields:

$$
G^{v,f}(\mathbf{x}^R, \mathbf{x}, t) = \frac{1}{2}\frac{1}{\rho c}\delta\left(t - \frac{|x^R - x|}{c}\right). \tag{B.14}
$$

One may note that the derived Green's states can also be derived by first applying the inverse Laplace transform to eq. (B.7) to obtain

$$
G(x,t) = \mathcal{L}^{-1}\left\{\hat{G}(x,s)\right\} = \frac{c}{2}H(t - \frac{|x|}{c}), \tag{B.15}
$$

where $H(t)$ is the Heaviside step function defined as $H(t) = \{0, 1\}$ for $\{t < 0, t > 0\}$. Applying the time domain equivalent operations of eqs. (B.2), (B.3) and (B.5) to eq. (B.15) yields eqs. (B.10), (B.13) and (B.14) respectively.

B.2 Two-dimensional Green's states

Following the same procedure used for the one dimensional Green's states, the starting point for the two dimensional case is the Green's function for cylindrical waves from an impulsive source [29]:

$$\hat{G}(\mathbf{x}, s) = -\frac{1}{2\pi} K_0(s\frac{|\mathbf{x}|}{c}), \tag{B.16}$$

where $K_0(s)$ is the zeroth order modified Bessel function of the second kind.

Starting with the derivation of $G^{p,q}$, filling in eq. (B.16) into eq. (B.2) results in:

$$\hat{G}^{p,q}(\mathbf{x}^R, \mathbf{x}, s) = -\rho s K_0\left(s\frac{|\mathbf{x}^R - \mathbf{x}|}{c}\right). \tag{B.17}$$

The inverse Laplace transform would then be obtained from

$$\begin{aligned}\mathcal{L}^{-1}\left\{\hat{G}^{p,q}(\mathbf{x}^R, \mathbf{x}, s)\right\} =& -\rho\mathcal{L}^{-1}\left\{sK_0\left(s\frac{|\mathbf{x}^R - \mathbf{x}|}{c}\right)\right\} \\ =& -\rho\frac{\partial}{\partial t}\mathcal{L}^{-1}\left\{K_0\left(s\frac{|\mathbf{x}^R - \mathbf{x}|}{c}\right)\right\}.\end{aligned}$$

The inverse Laplace transform of $K_0\left(s\frac{|\mathbf{x}^R-\mathbf{x}|}{c}\right)$ can be found in Bateman's Tables of Integral Transforms [38] and is found to be

$$\mathcal{L}^{-1}\left\{K_0\left(s\frac{|\mathbf{x}^R - \mathbf{x}|}{c}\right)\right\} = \frac{H\left(t - \frac{|\mathbf{x}^R-\mathbf{x}|}{c}\right)}{\sqrt{t^2 - \left(\frac{|\mathbf{x}^R-\mathbf{x}|}{c}\right)^2}},$$

where $H(t)$ is the Heaviside step function. The partial derivative with respect to time can be calculated as follows:

$$\begin{aligned}\frac{\partial}{\partial t}\frac{H\left(t - \frac{|\mathbf{x}^R-\mathbf{x}|}{c}\right)}{\sqrt{t^2 - \left(\frac{|\mathbf{x}^R-\mathbf{x}|}{c}\right)^2}} =& \frac{\partial}{\partial t}\frac{N}{D} \\ =& \frac{\frac{\partial}{\partial t}N}{D} - \frac{N\frac{\partial}{\partial t}D}{D^2}, \\ \frac{\partial}{\partial t}N =& \delta\left(t - \frac{|\mathbf{x}^R - \mathbf{x}|}{c}\right), \\ \frac{\partial}{\partial t}D =& \frac{t}{\sqrt{t^2 - \left(\frac{|\mathbf{x}^R-\mathbf{x}|}{c}\right)^2}}, \\ \frac{\partial}{\partial t}\frac{H\left(t - \frac{|\mathbf{x}^R-\mathbf{x}|}{c}\right)}{\sqrt{t^2 - \left(\frac{|\mathbf{x}^R-\mathbf{x}|}{c}\right)^2}} =& \frac{\delta\left(t - \frac{|\mathbf{x}^R-\mathbf{x}|}{c}\right)}{\sqrt{t^2 - \left(\frac{|\mathbf{x}^R-\mathbf{x}|}{c}\right)^2}} - \frac{H\left(t - \frac{|\mathbf{x}^R-\mathbf{x}|}{c}\right)t}{\sqrt{t^2 - \left(\frac{|\mathbf{x}^R-\mathbf{x}|}{c}\right)^2}^3}.\end{aligned}$$

Combining these results yields the time domain Green's state

$$G^{p,q}(\mathbf{x}^R, \mathbf{x}, t) = -\rho\frac{\delta\left(t - \frac{|\mathbf{x}^R-\mathbf{x}|}{c}\right)}{\sqrt{t^2 - \left(\frac{|\mathbf{x}^R-\mathbf{x}|}{c}\right)^2}} + \rho\frac{H\left(t - \frac{|\mathbf{x}^R-\mathbf{x}|}{c}\right)t}{\sqrt{t^2 - \left(\frac{|\mathbf{x}^R-\mathbf{x}|}{c}\right)^2}^3} \tag{B.18}$$

Moving on to $G_k^{v,q}$, substitution of eq. (B.16) into eq. (B.3) yields

$$\begin{aligned}\hat{G}_k^{v,q}(\mathbf{x}^R,\mathbf{x},s) =& -\partial_k^R\left(-\frac{1}{2\pi}K_0(s\frac{|\mathbf{x}^R-\mathbf{x}|}{c})\right),\\ \hat{G}_k^{v,q}(\mathbf{x}^R,\mathbf{x},s) =& \frac{1}{2\pi}\partial_k^R\left(K_0(s\frac{|\mathbf{x}^R-\mathbf{x}|}{c})\right).\end{aligned} \tag{B.19}$$

Regarding the derivatives of Bessel functions are obtained using the following equations:

$$\begin{aligned}\tfrac{d}{dx}J_0(x) &= -J_1(x), & \tfrac{d}{dx}J_n(x) &= +\tfrac{1}{2}\left(J_{n-1}(x)-J_{n+1}(x)\right),\\ \tfrac{d}{dx}Y_0(x) &= -Y_1(x), & \tfrac{d}{dx}Y_n(x) &= +\tfrac{1}{2}\left(Y_{n-1}(x)-Y_{n+1}(x)\right),\\ \tfrac{d}{dx}I_0(x) &= +I_1(x), & \tfrac{d}{dx}I_n(x) &= +\tfrac{1}{2}\left(I_{n-1}(x)+I_{n+1}(x)\right),\\ \tfrac{d}{dx}K_0(x) &= -K_1(x), & \tfrac{d}{dx}K_n(x) &= -\tfrac{1}{2}\left(K_{n-1}(x)+K_{n+1}(x)\right),\end{aligned}$$

where J_n is the Bessel function of the first kind of order n, Y_n is the Bessel function of the second kind of order n and I_n is the modified Bessel function of the first kind of order n.

Applying the relevant differential equation and the chain rule to eq. (B.19) yields

$$\begin{aligned}\hat{G}_k^{v,q}(\mathbf{x}^R,\mathbf{x},s) =& \frac{1}{2\pi}\left(-K_1\left(s\frac{|\mathbf{x}^R-\mathbf{x}|}{c}\right)\frac{s}{c}\frac{x_k^R-x_k}{|\mathbf{x}^R-\mathbf{x}|}\right)\\ =& -\frac{1}{2\pi c}\frac{x_k^R-x_k}{|\mathbf{x}^R-\mathbf{x}|}sK_1\left(s\frac{|\mathbf{x}^R-\mathbf{x}|}{c}\right)\end{aligned}$$

The inverse Laplace transform of $K_1\left(s\frac{|\mathbf{x}^R-\mathbf{x}|}{c}\right)$ is also found in Bateman's Tables of Integral Transforms [38] and is found to be

$$\mathcal{L}^{-1}\left\{K_1\left(s\frac{|\mathbf{x}^R-\mathbf{x}|}{c}\right)\right\} = \frac{H\left(t-\frac{|\mathbf{x}^R-\mathbf{x}|}{c}\right)}{\sqrt{t^2-\left(\frac{|\mathbf{x}^R-\mathbf{x}|}{c}\right)^2}}\frac{t}{\frac{|\mathbf{x}^R-\mathbf{x}|}{c}}.$$

The time domain representation of $\hat{G}_k^{v,q}(\mathbf{x}^R,\mathbf{x},s)$ will then become

$$\begin{aligned}G_k^{v,q}(\mathbf{x}^R,\mathbf{x},t) =& -\frac{1}{2\pi c}\frac{x_k^R-x_k}{|\mathbf{x}^R-\mathbf{x}|}\frac{\partial}{\partial t}\left(\frac{H\left(t-\frac{|\mathbf{x}^R-\mathbf{x}|}{c}\right)}{\sqrt{t^2-\left(\frac{|\mathbf{x}^R-\mathbf{x}|}{c}\right)^2}}\frac{t}{\frac{|\mathbf{x}^R-\mathbf{x}|}{c}}\right)\\ =& -\frac{1}{2\pi}\frac{x_k^R-x_k}{|\mathbf{x}^R-\mathbf{x}|^2}\frac{\partial}{\partial t}\left(\frac{H\left(t-\frac{|\mathbf{x}^R-\mathbf{x}|}{c}\right)}{\sqrt{t^2-\left(\frac{|\mathbf{x}^R-\mathbf{x}|}{c}\right)^2}}t\right).\end{aligned}$$

Resolving the partial derivative with respect to time in the same manner as before yields

$$G_k^{v,q}(\mathbf{x}^R,\mathbf{x},t) = -\frac{1}{2\pi}\frac{x_k^R-x_k}{|\mathbf{x}^R-\mathbf{x}|^2}\left(\frac{\delta\left(t-\frac{|\mathbf{x}^R-\mathbf{x}|}{c}\right)t}{\sqrt{t^2-\left(\frac{|\mathbf{x}^R-\mathbf{x}|}{c}\right)^2}}+\frac{H\left(t-\frac{|\mathbf{x}^R-\mathbf{x}|}{c}\right)}{\sqrt{t^2-\left(\frac{|\mathbf{x}^R-\mathbf{x}|}{c}\right)^2}}-\frac{H\left(t-\frac{|\mathbf{x}^R-\mathbf{x}|}{c}\right)t^2}{\sqrt{t^2-\left(\frac{|\mathbf{x}^R-\mathbf{x}|}{c}\right)^2}^3}\right) \tag{B.20}$$

Moving on to the last remaining Green's state, the previously obtained frequency domain Green's state is used as a starting point, similar to the one dimensional derivation. Doing so gives the following starting point

$$\begin{aligned}\hat{G}^{v,f}_{l,k}(\mathbf{x}^R,\mathbf{x},s) =&\frac{1}{s\rho}\partial^R_l\left[\frac{1}{2\pi c}\frac{x^R_k-x_k}{|\mathbf{x}^R-\mathbf{x}|}sK_1\left(s\frac{|\mathbf{x}^R-\mathbf{x}|}{c}\right)\right]\\ =&\frac{1}{s\rho}\frac{1}{2\pi c}s\partial^R_l\left[\frac{x^R_k-x_k}{|\mathbf{x}^R-\mathbf{x}|}K_1\left(s\frac{|\mathbf{x}^R-\mathbf{x}|}{c}\right)\right]\\ =&\frac{1}{2\pi\rho c}\partial^R_l\left[\frac{x^R_k-x_k}{|\mathbf{x}^R-\mathbf{x}|}K_1\left(s\frac{|\mathbf{x}^R-\mathbf{x}|}{c}\right)\right].\end{aligned}$$

Using the relations for the derivatives of the modified Bessel functions combined with the chain rule, quotient rule and product rule results in the frequency domain greens state

$$\begin{aligned}\hat{G}^{v,f}_{l,k}(\mathbf{x}^R,\mathbf{x},s) =&\frac{1}{2\pi\rho c}\left[\frac{K_1(sT_0)}{|\mathbf{x}^R-\mathbf{x}|}-\frac{(x^R_k-x_k)(x^R_l-x_l)}{|\mathbf{x}^R-\mathbf{x}|^3}K_1(sT_0)\right.\\ &\left.+\frac{(x^R_k-x_k)(x^R_l-x_l)}{|\mathbf{x}^R-\mathbf{x}|^2}\frac{s}{c}\left(-\frac{1}{2}K_0(sT_0)-\frac{1}{2}K_2(sT_0)\right)\right]\\ =&\frac{1}{2\pi\rho c}\frac{K_1(sT_0)}{|\mathbf{x}^R-\mathbf{x}|}\\ &-\frac{1}{2\pi\rho c}\frac{(x^R_k-x_k)(x^R_l-x_l)}{|\mathbf{x}^R-\mathbf{x}|^3}K_1(sT_0)\\ &-\frac{1}{4\pi\rho c^2}\frac{(x^R_k-x_k)(x^R_l-x_l)}{|\mathbf{x}^R-\mathbf{x}|^2}sK_0(sT_0)\\ &-\frac{1}{4\pi\rho c^2}\frac{(x^R_k-x_k)(x^R_l-x_l)}{|\mathbf{x}^R-\mathbf{x}|^2}sK_2(sT_0),\end{aligned}$$

where $T_0=\frac{|\mathbf{x}^R-\mathbf{x}|}{c}$. The time domain representation can then be obtained by resolving

$$\begin{aligned}\mathcal{L}^{-1}\left\{\hat{G}^{v,f}_{l,k}(\mathbf{x}^R,\mathbf{x},s)\right\} =&\frac{1}{2\pi\rho c}\frac{1}{|\mathbf{x}^R-\mathbf{x}|}\mathcal{L}^{-1}\{K_1(sT_0)\}\\ &-\frac{1}{2\pi\rho c}\frac{(x^R_k-x_k)(x^R_l-x_l)}{|\mathbf{x}^R-\mathbf{x}|^3}\mathcal{L}^{-1}\{K_1(sT_0)\}\\ &-\frac{1}{4\pi\rho c^2}\frac{(x^R_k-x_k)(x^R_l-x_l)}{|\mathbf{x}^R-\mathbf{x}|^2}\mathcal{L}^{-1}\{sK_0(sT_0)\}\\ &-\frac{1}{4\pi\rho c^2}\frac{(x^R_k-x_k)(x^R_l-x_l)}{|\mathbf{x}^R-\mathbf{x}|^2}\mathcal{L}^{-1}\{sK_2(sT_0)\}\end{aligned}$$

The inverse Laplace transform of $K_1(sT_0)$ and $K_0(sT_0)$ have already been presented earlier and the inverse Laplace transform of $K_2(sT_0)$ can be obtained from Bateman's Tables of Integral Transforms [38]:

$$\mathcal{L}^{-1}\left\{K_n\left(s\frac{|\mathbf{x}^R-\mathbf{x}|}{c}\right)\right\}=\frac{H\left(t-\frac{|\mathbf{x}^R-\mathbf{x}|}{c}\right)}{\sqrt{t^2-\left(\frac{|\mathbf{x}^R-\mathbf{x}|}{c}\right)^2}}\mathsf{cosh}\left(n\,\mathsf{cosh}^{-1}\left(\frac{t}{\frac{|\mathbf{x}^R-\mathbf{x}|}{c}}\right)\right).$$

Applying these inverse Laplace transforms yields:

$$
\begin{aligned}
G_{l,k}^{v,f} =& \frac{1}{2\pi\rho c}\frac{1}{|\mathbf{x}^R-\mathbf{x}|}\left\{\frac{H\left(t-\frac{|\mathbf{x}^R-\mathbf{x}|}{c}\right)}{\sqrt{t^2-\left(\frac{|\mathbf{x}^R-\mathbf{x}|}{c}\right)^2}}\frac{t}{\frac{|\mathbf{x}^R-\mathbf{x}|}{c}}\right\} \\
&- \frac{1}{2\pi\rho c}\frac{(x_k^R-x_k)(x_l^R-x_l)}{|\mathbf{x}^R-\mathbf{x}|^3}\left\{\frac{H\left(t-\frac{|\mathbf{x}^R-\mathbf{x}|}{c}\right)}{\sqrt{t^2-\left(\frac{|\mathbf{x}^R-\mathbf{x}|}{c}\right)^2}}\frac{t}{\frac{|\mathbf{x}^R-\mathbf{x}|}{c}}\right\} \\
&- \frac{1}{4\pi\rho c^2}\frac{(x_k^R-x_k)(x_l^R-x_l)}{|\mathbf{x}^R-\mathbf{x}|^2}\frac{\partial}{\partial t}\left\{\frac{H\left(t-\frac{|\mathbf{x}^R-\mathbf{x}|}{c}\right)}{\sqrt{t^2-\left(\frac{|\mathbf{x}^R-\mathbf{x}|}{c}\right)^2}}\right\} \\
&- \frac{1}{4\pi\rho c^2}\frac{(x_k^R-x_k)(x_l^R-x_l)}{|\mathbf{x}^R-\mathbf{x}|^2}\frac{\partial}{\partial t}\left\{\frac{H\left(t-\frac{|\mathbf{x}^R-\mathbf{x}|}{c}\right)}{\sqrt{t^2-\left(\frac{|\mathbf{x}^R-\mathbf{x}|}{c}\right)^2}}\cosh\left(2\cosh^{-1}\left(\frac{t}{\frac{|\mathbf{x}^R-\mathbf{x}|}{c}}\right)\right)\right\}
\end{aligned}
$$

Resolving the partial derivatives with respect to time yields:

$$
\begin{aligned}
G_{l,k}^{v,f} =& \frac{1}{2\pi\rho c}\frac{1}{|\mathbf{x}^R-\mathbf{x}|}\left\{\frac{H\left(t-\frac{|\mathbf{x}^R-\mathbf{x}|}{c}\right)}{\sqrt{t^2-\left(\frac{|\mathbf{x}^R-\mathbf{x}|}{c}\right)^2}}\frac{t}{\frac{|\mathbf{x}^R-\mathbf{x}|}{c}}\right\} \\
&- \frac{1}{2\pi\rho c}\frac{(x_k^R-x_k)(x_l^R-x_l)}{|\mathbf{x}^R-\mathbf{x}|^3}\left\{\frac{H\left(t-\frac{|\mathbf{x}^R-\mathbf{x}|}{c}\right)}{\sqrt{t^2-\left(\frac{|\mathbf{x}^R-\mathbf{x}|}{c}\right)^2}}\frac{t}{\frac{|\mathbf{x}^R-\mathbf{x}|}{c}}\right\} \\
&- \frac{1}{4\pi\rho c^2}\frac{(x_k^R-x_k)(x_l^R-x_l)}{|\mathbf{x}^R-\mathbf{x}|^2}\left\{\frac{\delta\left(t-\frac{|\mathbf{x}^R-\mathbf{x}|}{c}\right)}{\sqrt{t^2-\left(\frac{|\mathbf{x}^R-\mathbf{x}|}{c}\right)^2}}-\frac{H\left(t-\frac{|\mathbf{x}^R-\mathbf{x}|}{c}\right)t}{\sqrt{t^2-\left(\frac{|\mathbf{x}^R-\mathbf{x}|}{c}\right)^2}^3}\right\} \\
&- \frac{1}{4\pi\rho c^2}\frac{(x_k^R-x_k)(x_l^R-x_l)}{|\mathbf{x}^R-\mathbf{x}|^2}\left\{\right. \\
&\left.\frac{\sigma_1}{\sigma_2}\delta\left(t-T_0\right)-\frac{\sigma_1 t}{\sigma_2^3}H\left(t-T_0\right)+\frac{2\sinh\left(2\cosh^{-1}\left(\frac{t}{T_0}\right)\right)H\left(t-T_0\right)}{T_0\sigma_2\sqrt{\frac{t}{T_0}-1}\sqrt{\frac{t}{T_0}+1}}\right\}, \qquad \text{(B.21)} \\
\sigma_1 =& \cosh\left(2\cosh^{-1}\left(\frac{t}{T_0}\right)\right), \qquad \sigma_2=\sqrt{t^2-T_0^2} \qquad ,T_0=\frac{|\mathbf{x}^R-\mathbf{x}|}{c}.
\end{aligned}
$$

B.3 Three-dimensional Green's states

For the 3D case the Green's function is the following well known equation:

$$\hat{G}(\mathbf{x}, s) = \frac{exp(-s\frac{|\mathbf{x}|}{c})}{4\pi|\mathbf{x}|}. \tag{B.22}$$

Starting with eq. (B.2), filling in eq. (B.22) yields:

$$\hat{G}^{p,q}(\mathbf{x}^R, \mathbf{x}, s) = \rho s \left(\frac{exp(-s\frac{|\mathbf{x}^R-\mathbf{x}|}{c})}{4\pi|\mathbf{x}^R-\mathbf{x}|} \right). \tag{B.23}$$

The time domain version of this equation obtained by means of inspection similar, which yields

$$G^{p,q}(\mathbf{x}^R, \mathbf{x}, t) = \rho \frac{\frac{\partial}{\partial t}\left[\delta\left(t - \frac{|\mathbf{x}^R-\mathbf{x}|}{c}\right)\right]}{4\pi|\mathbf{x}^R-\mathbf{x}|}. \tag{B.24}$$

Moving on to derive $G_k^{v,q}$, substitution of eq. (B.22) into eq. (B.3) yields

$$\hat{G}_k^{v,q}(\mathbf{x}^R, \mathbf{x}, s) = -\partial_k^R \left(\frac{exp(-s\frac{|\mathbf{x}^R-\mathbf{x}|}{c})}{4\pi|\mathbf{x}^R-\mathbf{x}|} \right). \tag{B.25}$$

The spatial derivatives of the numerator and denominator are respectively

$$\begin{aligned}
\partial_k^R \left(exp(-s\frac{|\mathbf{x}^R-\mathbf{x}|}{c}) \right) &= \frac{-s}{c}\frac{x_k^R - x_k}{|\mathbf{x}^R-\mathbf{x}|} exp(-s\frac{|\mathbf{x}^R-\mathbf{x}|}{c}), \\
\partial_k^R \left(4\pi|\mathbf{x}^R-\mathbf{x}| \right) &= 4\pi\frac{x_k^R - x_k}{|\mathbf{x}^R-\mathbf{x}|}.
\end{aligned}$$

Using the quotient rule with these derivatives in eq. (B.25) yields the frequency domain result:

$$\begin{aligned}
\hat{G}_k^{v,q}(\mathbf{x}^R, \mathbf{x}, s) &= -\left(\frac{\frac{-s}{c}\frac{x_k^R-x_k}{|\mathbf{x}^R-\mathbf{x}|} exp(-s\frac{|\mathbf{x}^R-\mathbf{x}|}{c})}{4\pi|\mathbf{x}^R-\mathbf{x}|} - exp(-s\frac{|\mathbf{x}^R-\mathbf{x}|}{c})\frac{4\pi(x_k^R-x_k)}{|\mathbf{x}^R-\mathbf{x}|}\frac{1}{4^2\pi^2|\mathbf{x}^R-\mathbf{x}|^2} \right) \\
&= -\left(\frac{-s}{4\pi c}\frac{x_k^R-x_k}{|\mathbf{x}^R-\mathbf{x}|^2} exp(-s\frac{|\mathbf{x}^R-\mathbf{x}|}{c}) - \frac{1}{4\pi}\frac{x_k^R-x_k}{|\mathbf{x}^R-\mathbf{x}|^3} exp(-s\frac{|\mathbf{x}^R-\mathbf{x}|}{c}) \right), \\
\hat{G}_k^{v,q}(\mathbf{x}^R, \mathbf{x}, s) &= \frac{s}{4\pi c}\frac{x_k^R-x_k}{|\mathbf{x}^R-\mathbf{x}|^2} exp(-s\frac{|\mathbf{x}^R-\mathbf{x}|}{c}) + \frac{1}{4\pi}\frac{x_k^R-x_k}{|\mathbf{x}^R-\mathbf{x}|^3} exp(-s\frac{|\mathbf{x}^R-\mathbf{x}|}{c}).
\end{aligned} \tag{B.26}$$

Converting to the time domain by means of inspection yields the following equation:

$$G_k^{v,q}(\mathbf{x}^R, \mathbf{x}, t) = \frac{1}{4\pi c}\frac{x_k^R-x_k}{|\mathbf{x}^R-\mathbf{x}|^2}\frac{\partial}{\partial t}\delta(t - \frac{|\mathbf{x}^R-\mathbf{x}|}{c}) + \frac{1}{4\pi}\frac{x_k^R-x_k}{|\mathbf{x}^R-\mathbf{x}|^3}\delta(t - \frac{|\mathbf{x}^R-\mathbf{x}|}{c}). \tag{B.27}$$

The remaining Green's state can also be derived using the same method, starting with

$$\hat{G}_{l,k}^{v,f}(\mathbf{x}^R, \mathbf{x}, s) = \frac{1}{s\rho}\left[\partial_l^R \partial_k^R \left(\frac{exp(-s\frac{|\mathbf{x}^R-\mathbf{x}|}{c})}{4\pi|\mathbf{x}^R-\mathbf{x}|} \right) \right].$$

Filling in the partial spatial derivative ∂_k^R calculated for eq. (B.27) yields

$$\hat{G}_{l,k}^{v,f}(\mathbf{x}^R,\mathbf{x},s) = \frac{1}{s\rho}\partial_l^R\left[\frac{-s}{4\pi c}\frac{x_k^R-x_k}{|\mathbf{x}^R-\mathbf{x}|^2}exp(-s\frac{|\mathbf{x}^R-\mathbf{x}|}{c}) - \frac{1}{4\pi}\frac{x_k^R-x_k}{|\mathbf{x}^R-\mathbf{x}|^3}exp(-s\frac{|\mathbf{x}^R-\mathbf{x}|}{c})\right].$$

Using the same approach that was used to obtain eq. (B.27) will result in the following derivation:

$$\begin{aligned}\hat{G}_{l,k}^{v,f}(\mathbf{x}^R,\mathbf{x},s) =& \frac{1}{s\rho}\left[\frac{-s}{4\pi c}\partial_l^R\left(\frac{x_k^R-x_k}{|\mathbf{x}^R-\mathbf{x}|^2}exp(-s\frac{|\mathbf{x}^R-\mathbf{x}|}{c})\right)\right.\\ &\left. - \frac{1}{4\pi}\partial_l^R\left(\frac{x_k^R-x_k}{|\mathbf{x}^R-\mathbf{x}|^3}exp(-s\frac{|\mathbf{x}^R-\mathbf{x}|}{c})\right)\right]\\ =& \frac{-1}{4\pi\rho c}\partial_l^R\left(\frac{x_k^R-x_k}{|\mathbf{x}^R-\mathbf{x}|^2}exp(-s\frac{|\mathbf{x}^R-\mathbf{x}|}{c})\right)\\ &- \frac{1}{4\pi\rho s}\partial_l^R\left(\frac{x_k^R-x_k}{|\mathbf{x}^R-\mathbf{x}|^3}exp(-s\frac{|\mathbf{x}^R-\mathbf{x}|}{c})\right).\end{aligned}$$

The following spatial partial derivatives assist in writing out the required spatial partial derivatives.

$$\begin{aligned}\partial_l^R\left(x_k^R-x_k\right) =& 1,\\ \partial_l^R|\mathbf{x}^R-\mathbf{x}|^2 =& 2|\mathbf{x}^R-\mathbf{x}|\frac{x_l^R-x_l}{|\mathbf{x}^R-\mathbf{x}|} = 2(x_l^R-x_l),\\ \partial_l^R|\mathbf{x}^R-\mathbf{x}|^3 =& 3|\mathbf{x}^R-\mathbf{x}|^2\frac{x_l^R-x_l}{|\mathbf{x}^R-\mathbf{x}|} = 3(x_l^R-x_l)|\mathbf{x}^R-\mathbf{x}|.\end{aligned}$$

Applying the product and quotient rules yields the following:

$$\begin{aligned}\partial_l^R\left(\frac{x_k^R-x_k}{|\mathbf{x}^R-\mathbf{x}|^2}exp(-s\frac{|\mathbf{x}^R-\mathbf{x}|}{c})\right) =& \frac{exp(-s\frac{|\mathbf{x}^R-\mathbf{x}|}{c})}{|\mathbf{x}^R-\mathbf{x}|^2} - 2\frac{(x_k^R-x_k)(x_l^R-x_l)}{|\mathbf{x}^R-\mathbf{x}|^4}exp(-s\frac{|\mathbf{x}^R-\mathbf{x}|}{c})\\ &- \frac{s}{c}\frac{(x_k^R-x_k)(x_l^R-x_l)}{|\mathbf{x}^R-\mathbf{x}|^3}exp(-s\frac{|\mathbf{x}^R-\mathbf{x}|}{c})\\ \partial_l^R\left(\frac{x_k^R-x_k}{|\mathbf{x}^R-\mathbf{x}|^3}exp(-s\frac{|\mathbf{x}^R-\mathbf{x}|}{c})\right) =& \frac{exp(-s\frac{|\mathbf{x}^R-\mathbf{x}|}{c})}{|\mathbf{x}^R-\mathbf{x}|^3} - 3\frac{(x_k^R-x_k)(x_l^R-x_l)}{|\mathbf{x}^R-\mathbf{x}|^5}exp(-s\frac{|\mathbf{x}^R-\mathbf{x}|}{c})\\ &- \frac{s}{c}\frac{(x_k^R-x_k)(x_l^R-x_l)}{|\mathbf{x}^R-\mathbf{x}|^4}exp(-s\frac{|\mathbf{x}^R-\mathbf{x}|}{c})\end{aligned}$$

Substitution of these partial derivatives into $\hat{G}^{v,f}_{l,k}$ yields:

$$\begin{aligned}
\hat{G}^{v,f}_{l,k}(\mathbf{x}^R,\mathbf{x},s) = &-\frac{1}{4\pi\rho c}\left(\frac{exp(-s\frac{|\mathbf{x}^R-\mathbf{x}|}{c})}{|\mathbf{x}^R-\mathbf{x}|^2} - 2\frac{(x^R_k-x_k)(x^R_l-x_l)}{|\mathbf{x}^R-\mathbf{x}|^4}exp(-s\frac{|\mathbf{x}^R-\mathbf{x}|}{c})\right.\\
&\left.\qquad - \frac{s}{c}\frac{(x^R_k-x_k)(x^R_l-x_l)}{|\mathbf{x}^R-\mathbf{x}|^3}exp(-s\frac{|\mathbf{x}^R-\mathbf{x}|}{c})\right)\\
&-\frac{1}{4\pi\rho s}\left(\frac{exp(-s\frac{|\mathbf{x}^R-\mathbf{x}|}{c})}{|\mathbf{x}^R-\mathbf{x}|^3} - 3\frac{(x^R_k-x_k)(x^R_l-x_l)}{|\mathbf{x}^R-\mathbf{x}|^5}exp(-s\frac{|\mathbf{x}^R-\mathbf{x}|}{c})\right.\\
&\left.\qquad - \frac{s}{c}\frac{(x^R_k-x_k)(x^R_l-x_l)}{|\mathbf{x}^R-\mathbf{x}|^4}exp(-s\frac{|\mathbf{x}^R-\mathbf{x}|}{c})\right)\\
= &-\frac{exp(-s\frac{|\mathbf{x}^R-\mathbf{x}|}{c})}{4\pi\rho c|\mathbf{x}^R-\mathbf{x}|^2} + 2\frac{(x^R_k-x_k)(x^R_l-x_l)}{4\pi\rho c|\mathbf{x}^R-\mathbf{x}|^4}exp(-s\frac{|\mathbf{x}^R-\mathbf{x}|}{c})\\
&+\frac{s}{c}\frac{(x^R_k-x_k)(x^R_l-x_l)}{4\pi\rho c|\mathbf{x}^R-\mathbf{x}|^3}exp(-s\frac{|\mathbf{x}^R-\mathbf{x}|}{c})\\
&-\frac{1}{s}\frac{exp(-s\frac{|\mathbf{x}^R-\mathbf{x}|}{c})}{4\pi\rho|\mathbf{x}^R-\mathbf{x}|^3} + 3\frac{1}{s}\frac{(x^R_k-x_k)(x^R_l-x_l)}{4\pi\rho|\mathbf{x}^R-\mathbf{x}|^5}exp(-s\frac{|\mathbf{x}^R-\mathbf{x}|}{c})\\
&+\frac{s}{c}\frac{1}{s}\frac{(x^R_k-x_k)(x^R_l-x_l)}{4\pi\rho|\mathbf{x}^R-\mathbf{x}|^4}exp(-s\frac{|\mathbf{x}^R-\mathbf{x}|}{c}).
\end{aligned}$$

Rearranging terms yields the following expression for the frequency domain Green's state:

$$\begin{aligned}
\hat{G}^{v,f}_{l,k}(\mathbf{x}^R,\mathbf{x},s) = &\left(\frac{1}{4\pi\rho c^2}\frac{(x^R_k-x_k)(x^R_l-x_l)}{|\mathbf{x}^R-\mathbf{x}|^3}\right)s\ exp(-s\frac{|\mathbf{x}^R-\mathbf{x}|}{c})\\
&+\left(-\frac{1}{4\pi\rho c|\mathbf{x}^R-\mathbf{x}|^2} + 3\frac{(x^R_k-x_k)(x^R_l-x_l)}{4\pi\rho c|\mathbf{x}^R-\mathbf{x}|^4}\right)exp(-s\frac{|\mathbf{x}^R-\mathbf{x}|}{c})\\
&+\left(-\frac{1}{4\pi\rho|\mathbf{x}^R-\mathbf{x}|^3} + 3\frac{(x^R_k-x_k)(x^R_l-x_l)}{4\pi\rho|\mathbf{x}^R-\mathbf{x}|^5}\right)\frac{1}{s}exp(-s\frac{|\mathbf{x}^R-\mathbf{x}|}{c})
\end{aligned}$$

Conversion to the time domain is done by means of inspection and yields

$$\begin{aligned}
G^{v,f}_{l,k}(\mathbf{x}^R,\mathbf{x},t) = &\left(\frac{1}{4\pi\rho c^2}\frac{(x^R_k-x_k)(x^R_l-x_l)}{|\mathbf{x}^R-\mathbf{x}|^3}\right)\frac{\partial}{\partial t}\delta(t-\frac{|\mathbf{x}^R-\mathbf{x}|}{c})\\
&+\left(-\frac{1}{4\pi\rho c|\mathbf{x}^R-\mathbf{x}|^2} + 3\frac{(x^R_k-x_k)(x^R_l-x_l)}{4\pi\rho c|\mathbf{x}^R-\mathbf{x}|^4}\right)\delta(t-\frac{|\mathbf{x}^R-\mathbf{x}|}{c})\\
&+\left(-\frac{1}{4\pi\rho|\mathbf{x}^R-\mathbf{x}|^3} + 3\frac{(x^R_k-x_k)(x^R_l-x_l)}{4\pi\rho|\mathbf{x}^R-\mathbf{x}|^5}\right)\int\delta(t-\frac{|\mathbf{x}^R-\mathbf{x}|}{c})dt, \qquad \text{(B.28)}
\end{aligned}$$

where $\int\delta(t-\frac{|\mathbf{x}^R-\mathbf{x}|}{c})dt$ can be replaced by the Heaviside step function.